USES OF CHANNELING TECHNIQUE FOR DETERMINATION OF DEFECT CONCENTRATION AND STRUCTURES IN CRYSTALS

NORIAKI MATSUNAMI

PREFACE

This monograph is written on the basis of the results of the experimental and theoretical works made by the author under the auspices of Professor Noriaki Itoh. The present work was done at Prof. Itoh's Laboratory of Department of Nuclear Engineering, Nagoya University, from April 1970 to the present time.

Some of the contents have already been published in J. Phys. Soc. Japan, Radiation Effects and Phys. Letters. Others will be published soon.

March, 1976

Noriaki Matsunami

TABLE OF CONTENTS

Abbreviations

Symbol	Meaning
a	Thomas-Fermi screening radius
a_o	Bohr radius (0.529 A)
c	Fractional Concentration of defects
d	Distance between atoms in a string
e	Electronic charge; $e^2 = 14.39$ ev-A
$g(E_\perp, z)$	Distribution of particles in transverse energy $E_\perp$ at depth z
q	Defects concentration per cm^2
$\vec{r}$	Position in a channel
$\vec{r}_{in}$	Position of incidence in a channel
$\vec{s}$	Equilibrium position of displaced atoms in a channel
z	Depth from crystal surface
$A(E_\perp)$	Area accessible to particle with transverse energy $E_\perp$ (accessible area)
$D(E_\perp)$	Diffusion coefficient
E	Energy of incident particle
E_1	Characteristic energy for axial channeling
$E_\perp$	Transverse energy
$F(\vec{r}, z, \psi_{in})$	Flux distribution of particles at $\vec{r}$ in a channel
N	Number of host atoms per cm^3
Z_1, Z_2	Atomic numbers of incident ion and target atom, respectively
$P(\vec{r})$	Gaussian distribution of thermal displacements
$U(\vec{r})$	Transverse potential

$U_{row}(\rho)$	Continuum potential belonging to an atomic row (string potential)
$U_{row,T}(\rho)$	Thermally modified row potential
ε	Reduced energy of particle; $\varepsilon = E/(E_1/2)$
$\varepsilon_\perp$	Reduced transverse energy; $\varepsilon_\perp = E_\perp/(E_1/2)$
$\varepsilon_\perp^B$	Boundary transverse energy
$\varepsilon_\perp^c$	Critical transverse energy
$\pi(\varepsilon_\perp)$	Effectiveness factor
ρ	Distance from an atomic row
$\rho_\perp$	Thermal vibration amplitude normal to an atomic row
$\chi(z)$	Normalized yield of close encounter processes
$\chi_R(z)$	Normalized yield of close encounter processes with lattice atoms
$\chi_p(z)$	Random fraction for pure crystal
χ_d	Additive term of random fraction due to defects
χ_{min}	Minimum value of $\chi(z)$
ψ	Angle between particle velocity and an atomic row (crossing angle)
ψ_1	Characteristic angle for axial channeling
$\psi_{1/2}$	Half-angular width of channeling dip (half-angle)
ψ_{in}	Angle between incident beam and a major crystal axis

CHAPTER I

INTRODUCTION

When a well-collimated beam of the energetic charged particles is incident around a major axis (or plane) of crystals, the yields of the close encounter processes, e.g., Rutherford scattering, nuclear reaction, inner shell ionization are found to be strongly dependent on the relative orientations of the beam direction and crystal axes. These phenomena are called the channeling effect.[1 - 3] In view of the classical mechanics, this effect is qualitatively understood as follows: if the direction of the energetic charged particles is close to the direction of a major axis (or plane) of crystals, the particles will undergo correlated small-angle collisions because of the regular structure of the crystals. For positively charged particles, this results in a steering effect which causes the trajectories of such particles (i.e., channeled particles) to oscillate in the open channels between adjacent close-packed atomic rows (or planes). In other words, such particles with positive charge cannot come close to lattice atoms. Thus the yield of the close encounter processes of lattice atoms with the beam incident along a major crystal axis or plane, which is called the aligned yield, is reduced substantially as compared with the random yield, i.e., the close encounter

yield of lattice atoms with the beam incident along none of major axes nor planes. Furthermore, a somewhat reduced energy loss and a large penetration of ions are expected due to the channeling effect.

The concept of channeling for the energetic charged particles was originally envisaged by Stark[4] in 1912, when the existence of crystal lattices was conclusively demonstrated by the X-ray diffraction. In any event, fifty years passed before channeling was actually discovered. In 1963, Robinson and Oen[5] performed computer calculations on the penetration of ions in various crystals and they found abnormal large penetrations for those ions with initial velocities lying close to a major axis of crystals. They first observed that such particles are steered by a succession of the glancing collisions with atomic rows and their trajectories are constrained to within the open channels surrounded by the adjacent atomic rows. The word "channeling" originated from their observation. In the same year, Davies and collaborators,[6] Nelson and Thompson,[7] Lutz and Sizmann[8] provided independently the direct experimental evidence of the channeling effect.

To describe the channeling effect, a simple theory based on the continuum approximation has been developed by Lindhard[9] and Erginsoy.[10] In the continuum approximation it is assumed that the motion of the channeled ions is characterized by the transverse

motion, i.e., the motion on the plane normal to the atomic row (transverse plane) and that channeled ions feel an average continuum potential from a row (or plane), in which the atoms are regarded as a uniform line (or sheet) of charge. Lindhard has suggested that the energetic ions can keep the correlated glancing-collisions with a row, if the transverse energy, i.e., the energy associated with the transverse motion is less than the characteristic energy E_1, or if the crossing angle ψ between the ion velocity and the row (measured at the center of the channel) is less than the characteristic angle ψ_1. Here E_1 and ψ_1, for not too low energy E of the ions,[9] are given by

$$E_1 = \frac{2Z_1Z_2e^2}{d} \tag{1.1}$$

and

$$\psi_1 = \sqrt{E_1/E}\ , \tag{1.2}$$

where Z_1 and Z_2 are the atomic number of the incident ion and target atoms, respectively, e is the charge of an electron and d is the interatomic spacing along the row. The ions with the transverse energy larger than $E_1 = E\,\psi_1^2$ cannot continue the glancing collisions with a row. Such ions suffer a violent collision with lattice atoms, which are called non-channeled ions. For protons

or heliums with a few MeV, E_1 is usually several hundred eV and ψ_1 is typically of the order of 1°.

With the continuum approximation, Andersen[11] has calculated the normalized yield of particles emitted from thermally vibrating lattice atoms as a function of the emerging angle or the tilt angle from a major crystal axis or plane, which is called blocking dip: the blocking effect being the reverse process to the channeling effect. The half-angle, i.e., the half-width of the blocking dip, which agrees with that of the channeling dip because of the reversibility law, and the minimum yield, i.e., the lowest value of the aligned yield normalized by the random yield obtained by Andersen were in good agreement with the experimental results obtained by Picraux et al..[12] The minimum yield and the half-angle have been also calculated by Barrett[13] using a Monte Carlo method, in which the trajectory of each ion is traced and the close encounter yield is obtained directly, and better agreement with the experimental results has been obtained.

Lindhard[9] has also suggested that as the ions penetrate into the crystal, the scattering of the ions with electrons, thermally vibrating lattice atoms and lattice defects may increase the transverse energy or the crossing angle of the ions and cause the channeled ions to leave the channel or to be non-channeled ions. This effect, which is called dechanneling, has been ob-

served as the increase of the normalized aligned yield. A diffusion model, in which the transverse energy or the crossing angle of the channeled ions is assumed to be changed gradually, has been developed by several authors[14 - 17] and good agreement between the theoretical and experimental results has been obtained for pure crystals.

In addition to the study of understanding the channeling process itself, several important applications have been developed. One of them is an application for the investigation of lattice defects. The effects of lattice defects on the properties of crystals are important for the usage of the nuclear reactor materials under high energetic radiation. Furthermore, ion implantation technique,[18] which has been recently developed, is widely used for the modification of the properties of materials. In this technique, the knowledge of the defect structures and its distribution, and the location of the implanted ions in the lattice and its distribution are of particular interest.

As stated above, the close encounter processes are prohibited substantially between the channeled ions and lattice atoms but not prohibited between the channeled ions and the atoms displaced from an atomic row or plane. The displaced atoms are found to cause the dechanneling.[19, 20] The dechanneling phenomena are measured most conveniently by means of the backscatter-

ing technique, where the energy of the backscattered ions is analyzed. Since the difference between the energies of the incident and emerging ions depends on the distance by which the ions travel in solids, the energy of the emerging ions is indicative of the depth at which the backscattering takes place. Bøgh[20] has considered that the single scattering or multiple scattering with the displaced atoms (defects) brings the channeled ions to non-channeled ions and increases the backscattering yield. From the increment of the backscattering yield caused by defects in ion-implanted semi-conductors, the defect concentration has been derived as a function of the depth from the crystal surface.[21 - 27] The single or multiple scattering model has been often employed, resulting in the unexplainable problems; the defect concentration is larger than that theoretically predicted[28, 29] by a factor of 4 ~ 5 and increases super-linearly with the implantation dose and the half-width of the depth dependence of the defect concentration increases by a factor of 2 as the implantation dose increases. Although these facts have been ascribed to the characteristics of the ion-beam induced radiation damage, they may be ascribed alternatively to the underestimation of the random fraction (i.e., the close encounter yield with the lattice atoms) in channels containing lattice defects. To obtain the defect concentration correctly, it is necessary to know the de-

channeling caused by defects accurately.

Moreover, recent experimental works[30 - 32] have shown that the angular dependence of the close encounter yield with the impurity located near the center of the channel has a peak; this effect being called the flux-peaking. Soon, the theoretical works[33 - 35] have been made on the flux distribution of the channeled ions and the flux-peaking is understood as follows; the flux distribution of the channeled ions is dependent on the position in the channel and the incident angle. These results may indicate that the comparison between the theoretical and experimental angular dependence of the close encounter yield with an impurity would determine the location of the impurity.

In order to obtain the flux distribution of the channeled particles, either a Monte Carlo calculation or an analytical calculation has been used. The analytical calculation is more convenient than the Monte Carlo calculation and it may give a better understanding of channeling processes (from its simplicity). However, the validity of the continuum approximation employed in the analytical calculation is not well examined. Furthermore, the effects of lattice defects on the depth dependence of the flux distribution and on the dechanneling are of great importance for determining the defect concentration. Nevertheless, the effects of the lattice defects on the flux distribution of the channeled par-

ticles are almost unknown.

The present thesis intends to examine the validity of the continuum approximation in obtaining the flux distribution and the yield of close encounters as the function of the incident angle and the depth. This thesis also purposes to provide a quantitative knowledge of the effects of the lattice defects on the flux distribution of the channeled particles and on the random fraction, (especially depth dependence of the flux distribution of the channeled particles) and to establish the channeling technique for the defect study. The obtained results have been applied to the determination of an impurity location and the defect concentration in ion-implanted layers. In this thesis, the theoretical and experimental results are arranged in the following way.

Chapter II deals with the calculation of the flux distribution of the channeled ions as a function of the incident angle. The calculation is based on the continuum approximation. The results obtained with the present method are compared with those of the Monte Carlo calculations. The effectiveness factor or the reaction function, defined as the probability that the close encounter processes occur between the channeled ions with a given transverse energy and the atoms, is introduced on the basis of the continuum approximation. The validity of the continuum approximation is discussed.

Chapter III treats the calculation of the depth

dependence of the flux distribution or the distribution in the transverse energy. A diffusion model is used for the calculation of the particle distribution in the transverse energy. The effects of the lattice defects (displaced atoms) on the depth dependence of the particle distribution and the dechanneling are particularly investigated. The obtained results are compared with the results of the single scattering calculation, in which the modification of the particle distribution is not taken into account. The present results are also compared with the results of the multiple scattering calculation, in which the particle distribution is assumed to be a gaussian form. The modification of the particle distribution caused by defects is discussed in terms of the interference effect between the scattering with defects and the scattering with electrons and thermally vibrating lattice atoms.

In Chapter IV, channeling technique has been applied for determining the location of Pb impurities in irradiated KCl crystals. The angular dependence of the backscattering yield from the impurities is compared with that obtained in Chapter II. Optical absorption studies have been also made for Pb^{++}-doped KCl crystals. The location of diffusion-doped Au impurities in Si crystals is also determined by means of channeling technique.

Chapter V deals with the determination of the depth dependence of the defect concentration in ion-

implanted layers. In the previous method the equation derived by Bøgh,[20] combined with the single scattering model have been used. Since the previous treatments lead to unexplainable problems as stated above, a new method of determination of the random fraction and of the defect concentration is developed from another standpoint. The obtained random fraction is compared with that of theoretical calculation described in Chapter III. The depth dependence of the defect concentration obtained above is also compared with that of the elastic energy deposition calculated by Brice.[28]

Finally the conclusions of this thesis are given in Chapter VI and some problems to be solved in future are suggested.

References

1. R. S. Nelson,
   "The Observation of Atomic Collisions in Crystalline Solids," (North-Holland, Amsterdam, 1968).
2. "Chenneling," ed. by D. V. Morgan (John Wiley & Sons, 1973).
3. D. S. Gemmell, Rev. Mod. Phys. 46, 129 (1974).
4. J. Stark, Z. Phys. 13, 973 (1912).
5. M. T. Robinson and O. S. Oen,
   Appl. Phys. Letters 2, 30 (1963),
   Phys. Rev. 132, 2385 (1963).
6. G. R. Piercy, F. Brown, J. A. Davies and M. McCargo,
   Phys. Rev. Letters 10, 399 (1963).
7. R. S. Nelson and M. W. Thompson, Phil. Mag. 8, 1677 (1963).
8. H. O. Lutz and R. Sizmann, Phys. Letters 5, 113 (1963).
9. J. Lindhard,
   Mat. Fys. Medd. Dan. Vid. Selsk. 34, No. 14 (1965).
10. C. Erginsoy, Phys. Rev. Letters 15, 360 (1965).
11. J. U. Andersen,
    Mat. Fys. Medd. Dan. Vid. Selsk. 36, No. 7 (1967).
12. S. T. Picraux, J. A. Davies, L. Eriksson,
    N. G. E. Johansson and J. W. Mayer,
    Phys. Rev. 180, 873 (1969).
13. J. H. Barrett, Phys. Rev. B3, 1527 (1971).
14. L. C. Feldman, B. R. Appleton and W. L. Brown,
    BNL-50083, p. 58 (1968).
15. K. Morita and N. Itoh, J. Phys. Soc. Japan 30, 1430 (1971).
16. E. Bonderup, H. Esbensen, J. U. Andersen and H. E. Schiøtt,
    Rad. Effects 12, 261 (1972).

17. V. V. Beloshitsky, M. A. Kumakhov and V. A. Muralev, Rad. Effects 13, 9 (1972).

18. J. W. Mayer, L. Eriksson and J. A. Davies, "Ion Implantation in Semiconductors," (Academic Press, New York, 1970).

19. J. A. Davies, J. Denhartog, L. Eriksson and J. W. Mayer, Can. J. Phys. 45, 4053 (1967).

20. E. Bøgh, Can. J. Phys. 46, 653 (1968).

21. J. W. Mayer, L. Eriksson, S. T. Picraux and J. A. Davies, Can. J. Phys. 46, 663 (1968).

22. L. C. Feldman and J. W. Rodgers, J. Appl. Phys. 41, 3776 (1970).

23. F. H. Eisen, B. Welch, J. E. Westmoreland and J. W. Mayer, "Atomic Collision Phenomena in Solids," ed. by D. W. Palmer, M. T. Thompson and P. D. Townsend (North-Holland, Amsterdam, 1970) p. 111.

24. J. E. Westmoreland, J. W. Mayer, F. H. Eisen and B. Welch, Rad. Effects 6, 161 (1970).

25. J. F. Ziegler, J. Appl. Phys. 43, 2973 (1972).

26. K. Schmid, Rad. Effects 17, 201 (1973).

27. P. P. Promko, J. B. Mitchell, J. Shewchun and J. A. Davies, Rad. Effects 20, 257 (1973).

28. D. K. Brice, Rad. Effects 6, 77 (1970).

29. T. Tsuruchima and H. Tanoue, "Ion Impantation in Semiconductors," ed. by S. Namba (Plenum Press, New York, 1975) p. 429.

30. B. Domeij, G. Fladda and N. G. E. Johansson, Rad. Effects 6, 155 (1970).

31. J. U. Andersen, O. Andreasen, J. A. Davies and E. Uggerhøj Rad. Effects 7, 25 (1971).

32. J. U. Andersen, E. Laegsgaard and L. C. Feldman, Rad. Effects 12, 219 (1972).

33. R. B. Alexander, G. Dearnaley, D. V. Morgan and J. M. Poate, Phys. Letters A32, 365 (1970).

34. D. Van Vliet, Rad. Effects 10, 137 (1971).

35. D. V. Morgan and D. Van Vliet, Rad. Effects 12, 203 (1972).

CHAPTER II

CONTINUUM CALCULATION OF THE SCATTERING YIELDS OF CHANNELED PARTICLES FOR ATOM LOCATION

2.1 Introduction

Ion channeling has been used for the determination of the location of an impurity in the lattice.[1] In this technique, the yields of the close encounter, e.g., Rutherford scattering, nuclear reaction, both between the incident ions and the impurities, and between incident ions and the host atoms are measured as a function of the angle between a well-collimated beam of the energetic ions and a major crystal axis. The angular dependence of the yield scattered by the substitutional impurity around a high symmetry axis has the same dip as that scattered by the host atoms.[2,3] For the impurity located close to the center of the channel, a central peak appears in the angular variation curve of the impurity yields, which is called flux-peaking.[4-6] For the impurity situated at neither substitutional sites nor the center of the channel, it has been established[7-9] that the comparison between the theoretical and experimental scattering yields from the impurity may give an approximate position in the lattice.

In order to obtain the theoretical angular dependence of the scattering yield from the impurity,

either a Monte Carlo calculation or an analytical calculation has been employed. In a Monte Carlo calculation,[8-15] the trajectory of each particle is traced and the close encounter probability with displaced atoms is calculated directly. It can include various effects such as the angular spread of the incident beam, the multiple scattering with electrons and thermally vibrating atoms and the depth effects. However, the computation time is long. In the increasing utility of the channeling for the determination of the impurity location, more convenient method or an analytical calculation, in which the computation time is short, is necessary. The analytical calculation based on the continuum approximation[16] has been made by several authors.[7, 8, 11, 17, 18] Although it has been concluded by Alexander et al.[8] that the analytical calculation and the Monte Carlo calculation give essentially the same results in certain cases, it has been pointed out by Barrett[12, 19] that the analytical calculation underestimates the minimum yield by a factor of three and that the statistical hypothesis, which is essential in the analytical calculation, is not a sound approximation. The validity of the continuum approximation is not well examined.

In this chapter, the flux distribution of the channeled particles, the close encounter yields, such as Rutherford backscattering yield, the minimum yield

and the half-angle have been calculated with the analytical method on the basis of the continuum approximation. Furthermore, the effectiveness factor[12] or the reaction function[20] defined as the probability that the close encounter occurs between the incident ions with a given transverse energy and target atoms is introduced based on the continuum approximation. The obtained results are compared with those of the Monte Carlo calculations. The validity of the continuum approximation and its applicability to the description of the channeled ions are discussed.

2.2 Method of Calculation

In the continuum approximation, the motion of the energetic particles is assumed to be well described by its transverse energy. For the particles with the crossing angle ψ between the particle velocity and the axis at $\vec{r}$ in the channel (see Fig. 2.1), the transverse enegy $E_\perp$ is given by

$$E_\perp = U(\vec{r}) + E\psi^2 , \qquad (2.1)$$

where E is the incident energy of the particles and $U(\vec{r})$ is the transverse potential. The transverse potential is calculated by

$$U(\vec{r}) = \sum_n U_{row}(|\vec{r}-\vec{r}_n|) - U_{min}. \qquad (2.2)$$

Here $U_{row}(\rho)$ is a row (or string) potential and U_{min}

is a constant such that $U(\vec{r})$ goes to zero at its minimum. The summation is taken over the atomic rows surrounding the channel.

In the present calculation, the Molière approximation[21] to the Thomas-Fermi potential is used for the ion-atom interaction potential. Then the static row potential or the string potential $U_{row}(\rho)$ at a distance ρ from the string is given by

$$U_{row}(\rho) = \frac{Z_1 Z_2 e^2}{d}\{0.2K_o(6\rho/a) + 1.1K_o(1.2\rho/a) + 0.7K_o(0.3\rho/a)\}. \tag{2.3}$$

Here Z_1 and Z_2 are the atomic numbers of the incident ions and target atoms, respectively, d is the interatomic spacing in the string, e is the electronic charge, K_o is the zeroth-order modified Bessel function of the second kind, and a is the Thomas-Fermi radius. The Thomas-Fermi radius a is given by

$$a = \frac{0.8853a_o}{(Z_1^{2/3} + Z_2^{2/3})^{1/2}}, \tag{2.4}$$

where a_o is the Bohr radius (0.529 A).

As the distance ρ from the string goes to zero, $U_{row}(\rho)$ goes to infinite. The thermal vibration of the atoms was taken into consideration as suggested by Erginsoy.[22] Assuming a gaussian distribution of the thermal displacements of the atoms, the thermally modified row potential is calculated by

$$U_{row,T}(\rho) = \int_0^\infty \frac{dr^2}{\rho_\perp^2} \exp(-r^2/\rho_\perp^2) \int_0^\pi \frac{d\theta}{\pi} U_{row}\left\{(\rho^2 + r^2 - 2r\rho\cos\theta)^{1/2}\right\} . \tag{2.5}$$

Here $\rho_\perp$ is the thermal vibration amplitude in the plane normal to the string at a temperature T, and given by

$$\rho_\perp = \sqrt{2/3}\ \bar{u} ,$$

where $\bar{u}$ is the usual root mean square of the thermal vibration amplitude in three dimensions.

From the classical standpoint, the motion of the particles with $E_\perp$ is found to be constrained within the accessible area $A(E_\perp)$, in which $U(\vec{r}) \leqq E_\perp$. It is assumed in the continuum approximation that the statistical equilibrium is attained. Then the particles with a given transverse energy $E_\perp$ are distributed uniformly in the accessible area $A(E_\perp)$.

Now the flux distribution $F(\vec{r}, z, \psi_{in})$ of the particles at $\vec{r}$ is the channel for an incident angle ψ_{in} at a depth z is obtained by

$$F(\vec{r}, z, \psi_{in}) = \int_{U(\vec{r}) \leqq E_\perp} \frac{g(E_\perp, z, \psi_{in})}{A(E_\perp)} dE_\perp , \tag{2.6}$$

where $g(E_\perp, z, \psi_{in})$ is the distribution of the particles in the transverse energy $E_\perp$ at a depth z, for an incident

angle ψ_{in}. Since the depth necessary for the measurements of the impurity location is rather shallow, the transverse energy at the crystal surface is assumed to be conserved and given by

$$E_{\perp} = U(\vec{r}_{in}) + E\psi_{in}^{2}. \qquad (2.7)$$

Here $\vec{r}_{in}$ is the position of incidence. Then $g(E_{\perp},z,\psi_{in})$ is replaced by $g_o(E_{\perp}, \psi_{in}) \equiv g(E_{\perp},0,\psi_{in})$ and the flux distribution becomes independent of the depth z. It is clear from Eq.(2.6) that the flux distribution at $\vec{r}$ is determined by the transverse potential $U(\vec{r})$. The ions are assumed to be random or distributed uniformly, when the transverse energy $E_{\perp}$ exceeds a transverse energy $E_{\perp}^{B}$ (boundary transverse energy). Moreover, in order to avoid the divergence of the flux due to the fact that $A(0) = 0, \delta E_{\perp}$ corresponding to the scattering with electrons in the depth for the mesurements is added to Eq.(2.7) in the calculation of the $A(E_{\perp})$, as suggested by Van Vliet.[11]

The close encounter yield $\chi(\vec{s},\psi_{in})$ between the ions and the atoms, whose equilibrium position is, $\vec{s}$ in the channel is calculated by

$$\chi(\vec{s}, \psi_{in}) = \int F(\vec{r},\psi_{in}) P_s(\vec{r}) d\vec{r}. \qquad (2.8)$$

Here $P_s(\vec{r})$ is the probability for the atoms being $\vec{r}$ in the channel:

$$P_s(\vec{r})d\vec{r} = \frac{d\vec{r}}{\pi\rho_{\perp}^{2}} \exp(-|\vec{r}-\vec{s}|^{2}/\rho_{\perp}^{2}). \qquad (2.9)$$

The yield $\chi(\vec{s},\psi_{in})$ is also given as a form:

$$\chi(\vec{s},\psi_{in}) = \int g(E_\perp,\ 0,\psi_{in})\Pi(E_\perp)dE_\perp, \qquad (2.10)$$

where $\Pi(E_\perp)$ is the effectiveness factor[12] or the reaction function.[20] From Eqs.(2.8), (2.9) and (2.10), the effectiveness factor $\Pi(E_\perp)$ is shown to be given by

$$\Pi(E_\perp) = \frac{1}{A(E_\perp)} \int_{U(\vec{r})\leq E_\perp} P_s(\vec{r})d\vec{r} \quad . \qquad (2.11)$$

This is the similar expression as $\Pi_{out}(E_\perp)$ derived by Lindhard.[16] It should be noted that $\Pi(E_\perp)$ is independent of the flux, and $\Pi(E_\perp)$ is a function of $\rho_\perp$ and $\vec{s}$.

The calculation has been made for the case that the helium ions of MeV are incident along the <100> direction of Cu. The geometry of the <100> channel of Cu is shown in Fig. 2.1.

2.3 Results and Discussion

2.3.1 Transverse Potential

The thermally modified row potential $U_{row,T}(\rho)$ calculated with Eq.(2.5) for He^+ in the <100> string of Cu at room temperature ($\rho_\perp$ = 0.12 Å) is shown by the solid line in Fig. 2.2. The static row potential $U_{row}(\rho)$ is also shown in the figure (broken line). The potential is expressed in the reduced unit ($Z_1Z_2e^2/d$ = 231 eV). It is seen that $U_{row,T}(\rho)$ is almost the same as $U_{row}(\rho)$ for $\rho > \rho_\perp$ and $U_{row,T}(\rho)$ is nearly flat for $\rho < \rho_\perp$. Then

$U_{row,T}(\rho)$ is well approximated by

$$U_{row,T}(\rho) = \begin{cases} U_{row,T}(0) & \rho \leqq \rho_o \\ U_{row}(\rho) & \rho > \rho_o \end{cases} , \qquad (2.12)$$

where ρ_o is given by

$$U_{row}(\rho_o) = U_{row,T}(0) \quad . \qquad (2.13)$$

Clearly, ρ_o is close to $\rho_\perp$. It is emphasized that the thermally modified row potential does not affect the particles away from $\rho_o \simeq \rho_\perp$, but the flux for $\rho < \rho_o$ and the minimum yield.

The transverse potential $U(\vec{r})$ was obtained by summing four string potentials (Eq.(2.2)) and the equi-potential contours are shown in Fig. 2.3. The difference between the transverse potential obtained with four string calculation and with sixteen string calculation was less than ~15 %. It is to be noted that the equi-potential contour is closed for $U(\vec{r}) \leqq 0.05$(~10 eV).

Moreover, $U_{row,T}(0)$ is found to be only a function of $\rho_\perp/a$, if $U_{row,T}(0)$ is expressed in the reduced unit $(Z_1 Z_2 e^2/d)$. Figure 2.4 shows the $U_{row,T}(0)$ as a function of $\rho_\perp/a$. The value of $U_{row,T}(0)$ gives the maximum transverse energy of the particles for $\psi_{in} = 0$.

2.3.2 Accessible Area

The accessible area $A(\mathcal{E}_\perp)$ as a function of the reduced transverse energy $(\mathcal{E}_\perp = E_\perp/(Z_1 Z_2 e^2/d))$ was cal-

culated as follows. From the symmetry of the <100> channel of Cu, the one-fourth of the channel is divided into a small sections $\Delta A_i = (A_o/4)/(5 \times 10^4)$, where A_o is the area of the channel. $U(\vec{r}_i)$ at the center of each sections were calculated. Then the accessible area $A(\varepsilon_\perp)$ is given by the four times of the summation of the area ΔA_i over the sections in which the relation: $\varepsilon_\perp \geqq U(\vec{r}_i)$ is satisfied. Figure 2.5 shows the accessible area $A(\varepsilon_\perp)$, which is normalized by the area of the channel A_o (solid line). In the figure, the results obtained with the one string approximation, which has been used frequently (see Sec. 3.2.3 in Chapter III), are also shown (broken line). For low $\varepsilon_\perp$, the one string approximation overestimates the accessible area by a factor of two. For large $\varepsilon_\perp$, both results are in good agreement. It is to be noted that $A(\varepsilon_\perp)$ increases suddenly at $\varepsilon_\perp \sim 0.05$. This is due to the facts that the equi-potential contour is closed for $\varepsilon_\perp < 0.05$ and open for $\varepsilon_\perp > 0.05$ as shown in Fig. 2.3.

2.3.3 Initial Distribution

Assuming that the particles are incident uniformly on the crystal surface, the initial distribution $g_o(\varepsilon_\perp, \psi_{in})$ for $\psi_{in} = 0$ is obtained by

$$g_o(\varepsilon_\perp, 0) = \frac{dA(\varepsilon_\perp)}{d\varepsilon_\perp} \quad . \qquad (2.14)$$

Figure 2.6 shows the initial distribution $g_o(\varepsilon_\perp, 0)$ (solid line). The initial distribution $g_o(\varepsilon_\perp, 0)$ obtained with

the one string approximation is also shown in the figure (broken line). The difference between the four string calculation and the one string calculation is less than 15 % for not too low $\mathcal{E}_\perp$. In the above equation, the angular spread of the incident beam is neglected. Thus $g_o(\mathcal{E}_\perp, 0)$ is substantially zero for $\mathcal{E}_\perp \geqq U_{row,T}(0)$. The peak around $\mathcal{E}_\perp \sim 0.05$ is also due to the facts that the equi-potential contour is closed for $\mathcal{E}_\perp < 0.05$ and opened for $\mathcal{E}_\perp > 0.05$. $g_o(\mathcal{E}_\perp)$ for $\mathcal{E}_\perp \leqq 0.05$ may correspond to the hyper-channeled particles,[23] which are constrained within one channel. The initial distribution obtained with the static-row potential is also shown in the figure. The dot-dash and the dotted lines were obtained with four string calculation and one string calculation, respectively.

For $\psi_{in} \neq 0$, the initial distribution $g_o(\mathcal{E}_\perp, \psi_{in})$ is given by

$$g_o(\mathcal{E}_\perp, \psi_{in}) = \begin{cases} 0 & \mathcal{E}_\perp < \mathcal{E}\psi_{in}^2 \\ g_o(\mathcal{E}_\perp - \mathcal{E}\psi_{in}^2, 0) & \mathcal{E}_\perp \geqq \mathcal{E}\psi_{in}^2 \end{cases}, \tag{2.15}$$

where $\mathcal{E}$ is the energy of the incident particle in the reduced unit ($\mathcal{E} = E/(Z_1 Z_2 e^2/d)$).

It should be noticed that $A(\mathcal{E}_\perp)$ and $g_o(\mathcal{E}_\perp, 0)$ do not depend on the energy E of the incident particle. Thus the flux distribution is independent of E.

2.3.4 Flux Distribution

The flux distribution was calculated from the distribution in the $\mathcal{E}_\perp$ - space by means of Eq.(2.6). As stated in Sec. 2.2, in order to avoid the divergence of the flux, the value of the accessible area at $\mathcal{E}_\perp$ is replaced by $\mathcal{E}_\perp + \delta\mathcal{E}_\perp$, where $\delta\mathcal{E}_\perp = \mathcal{E}(\Delta\psi)^2$ is taken as 0.0043(1eV) corresponding to the angular spread $\Delta\psi$ due to multiple scattering with electrons, as suggested by Van Vliet. Furthermore, the boundary transverse energy $\mathcal{E}_\perp^B$ in the reduced unit is taken as the maximum value of the thermally modified row potential $U_{row,T}(0)$ ($U_{row,T}(0) = 2.0$ at room temperature).

In Fig. 2.7, the equi-flux contours of channeled ions calculated with the present analytical method (solid line) for 1 MeV He^+ in the <100> channel of Cu at $\psi_{in} = 0$ are compared with the results of the Monte Carlo calculation or the simulation calculation obtained by Van Vliet[11] (broken line). Only one quarter of the channel is shown but the rest of the profile is symmetric. The Cu atom is indicated by an open circle. In the present analytical calculation, the fraction of the particles with $\mathcal{E}_\perp$ larger than $\mathcal{E}_\perp^B = 2.0$, which is called the random component, was obtained as $\pi N d \rho_o^2 = 0.7$ % for $\psi_{in} = 0$. Thus the random component does not affect the flux distribution nor the close encounter yields with displaced atoms, and the results are almost independent of temperature.

From Fig. 2.7, it is seen that the results of the

analytical calculation agree well with those of the simulation calculation near the string. On the other hand, disagreement in the analytical and simulation calculations is remarkable near the center and the side of the channel. The discrepancies between the analytical and simulation calculations may be ascribed to the following facts. In the analytical calculation, the effects of the angular spread of the incident beam and the multiple scattering with electrons and thermally vibrating strings are not taken into account. However, the simulation calculation shows that these effects influence appreciably the flux near the center and the side of the channel. Moreover the simulation calculations include the depth effect on the flux, which is not included in the statistical-hypothesis.

Figure 2.8 shows the angular dependence of the flux at various positions in the channel, which are indicated in the figure. The angle of incidence ψ_{in} is normalized by the Lindhard's characteristic angle ψ_1 = 1.0° for E = 1.5 MeV. The right-hand side is the results of the present analytical calculation and the left-hand side is those of the simulation calculation obtained by Morgan et al.[13] Since the random component for $\psi_{in} < \psi_1$ is very small, the random component has little effects for the flux. At the center of the channel (a), the profiles and the half-widths of the peak are in good agreement for both calculations. At the position of (b) and (c), the angle of the maximum yield

and the half-width of the dip are also in good agreement, respectively, for both calculations, but the peak at position (b) is more pronounced for the simulation calculation. On the other hand, at the position (d), the analytical calculation shows a double-peak while the simulation calculation shows a dip. As already described, the discrepancy may be due to the facts that the effects of the lattice vibrations, the multiple scattering with electrons and the initial beam divergence are not taken into account in the analytical calculation. Although both calculations disagree near the side of the channel as represented by the position (d), the good agreements of the profiles are obtained at the position (a), (b) and (c).

The effects of the angular spread of the incident beam may be incorporated by integrating the flux distribution (shown in Fig. 2.8) multiplied by a gaussian form ($\frac{1}{\sqrt{\pi}\Delta\psi}\mathrm{Exp}(-(\psi/\Delta\psi)^2)$). Figure 2.9 shows the angular dependence of the flux, in which the angular spread of the incident beam was taken into account, at various positions in the channel (see Fig. 2.8). The solid line and the broken line are the results for the angular spread of the incident beam $\Delta\psi = 0$ and for $\Delta\psi = 0.1\psi_1$, respectively. At the positions (a) and (c), the better agreements of the analytical and simulation calculations are obtained. However, at the position (b), the double-peak disappears and only a broad peak is seen. This result is quite different from the simulation calcula-

tion, and indicates that the assumption of the uniform distribution leads to the absence of double-peak at the position (b). The experimental studies on this point may, in turn, give a measure whether the uniform distribution is valid or not.

2.3.5 Close Encounter Yield

The yields of the close encounter between the energetic ions and atoms located at various positions were obtained by Eqs.(2.8) and (2.9) at room temperature. Figure 2.10 shows the angular dependence of the close encounter yield, e. g., scattering yield. The incident angle ψ_{in} is also normalized by $\psi_1 = 1.0^{\circ}$ for E = 1.5 MeV. The angular spread of the incident beam was not taken into account. The yields were averaged by the thermal displacements of atoms. Here, the yield at the lattice position (e), i.e., channeling dip is compared with the experimental and theoretical results as follows. Figure 2.11 shows the angular dependence of the channeling dip at various temperatures. These temperature dependence of the channeling dip appears to be similar as the experimental results for H^+ in the <110> channel of Au obtained by Howe and Schmid[24].

From Fig. 2.11, the minimum yield χ_{min} and the half angle $\psi_{1/2}$ were calculated. The results are shown in Figs. 2.12 and 2.13, where they are compared with the results obtained by Barrett[12]. The half-angle $\psi_{1/2}$ obtained with the present calculation shows the similar

temperature dependence as that by Barrett, but the value is large by 10 %. The minimum yield $\chi_{min} \simeq \pi N d \rho_\perp^2$ was obtained for the present calculation, which is smaller by a factor of three than the results obtained by Barrett. The discrepancy is discussed in terms of the effectiveness factor $\Pi(\varepsilon_\perp)$.

Figure 2.14 shows $\Pi(\varepsilon_\perp)$ at room temperature (solid line). Clearly, $\Pi(\varepsilon_\perp)$ is less than unity for $\varepsilon_\perp < \varepsilon_\perp^B$ and $\Pi(\varepsilon_\perp)$ is unity for $\varepsilon_\perp \geqq \varepsilon_\perp^B$ in the continuum approximation. The gap at $\varepsilon_\perp^B$ is originated from the approximation of Eq.(2.12). On the other hand, it has been pointed out by Barrett[12, 19] that $\Pi(\varepsilon_\perp)$ is larger than unity for $\varepsilon_\perp \sim \varepsilon_\perp^B$ due to the focusing effects. In addition, the distribution at the depth, where the close encounter yield is measured, should have a tail in $g_0(\varepsilon_\perp, 0)$ for $\varepsilon_\perp \geqq \varepsilon_\perp^B$ due to the scattering with electrons and thermally vibrating lattice atoms. These facts lead to that $\chi_{min} = 3\pi N d \rho_\perp^2$. In Fig. 2.14, $\Pi(\varepsilon_\perp)$ obtained with the thermally modified row potential (Eq.(2.5)) is also shown (dotted line). This corrected $\Pi(\varepsilon_\perp)$ is smoothly changed around $\varepsilon_\perp \sim \varepsilon_\perp^B$, but does not affect the results appreciably.

At the other position $\vec{s}$ in the channel, $\Pi(\varepsilon_\perp)$ was also calculated and shown in Fig. 2.14 (broken line) for the position $\vec{s}$=(0.4 A,0.4 A). It is seen that $\Pi(\varepsilon_\perp)$ varies as a step function. In this case, $\Pi(\varepsilon_\perp)$ exceeds unity. Since the yield is given by integrating $g(\varepsilon_\perp, 0)\Pi(\varepsilon_\perp)$

and $g(\varepsilon_\perp, 0)$ is peaked at $\varepsilon_\perp \sim 0$, the focussing effect ($\varepsilon_\perp \sim \varepsilon_\perp^B$) may make little contribution to the scattering yield.

2.4 Conclusion

The flux distribution has been calculated with the analytical method based on the continuum approximation for MeV He^+ incident on the <100> channel of Cu. For the incident angle $\psi_{in} = 0$, the comparison of the present results with those of the Monte Carlo calculation shows that not very close to the center, atmic row nor side of the channel, the flux distribution for both calculations are in good agreement. The discrepancy for the vicinity of the center is shown to be improved by taking the angular spread into consideration. The angular dependence of the flux has been also calculated at various positions in the channel and the results are found to agree with the Monte Carlo calculation at the center of the channel. The double-peak obtained with the present calculation at the position apart from the center is not so pronounced, as compared with the results of the Monte Carlo calculations. The situation is not altered by taking the angular spread of the incident beam into consideration in the analytical calculation. These discrepancies may be ascribed to the fact that the steering effect in the transient refion or the oscillation of the flux distribution is more emphasized

in the Monte Carlo calculation.

The angular dependence of the close encounter yields has been also calculated at the various positions in the channel. From the channeling dip, i.e., the close encounter yield for the lattice atoms, the minimum yield χ_{min} and the half-angle $\psi_{1/2}$ are obtained. The half-angle $\psi_{1/2}$ obtained with the present calculation is in good agreement with the value obtained by Barrett, but χ_{min} is smaller by a factor of 3 than that by Barrett. This discrepancy is discussed in terms of the effectiveness factor $\Pi(\varepsilon_\perp)$. In the continuum approximation $\Pi(\varepsilon_\perp)$ is less than unity for the transverse energy $\varepsilon_\perp$ is less than the boundary transverse energy $\varepsilon_\perp^B$ and $\Pi(\varepsilon_\perp)$ approaches to unity for $\varepsilon_\perp \geqq \varepsilon_\perp^B$, and the distribution $g(\varepsilon_\perp, 0)$, which should be multiplied in obtaining χ_{min}, is substantially zero for $\varepsilon_\perp \geqq \varepsilon_\perp^B$. On the other hand, the Monte Carlo calculations show that $\Pi(\varepsilon_\perp)$ is larger than unity for $\varepsilon_\perp \sim \varepsilon_\perp^B$ due to the focusing effects and $g(\varepsilon_\perp, 0)$ has an appreciable value, due to the scattering with electrons and thermally vibrating lattice atoms. This results in a larger χ_{min}.

However, at the position inside the channel, the term added to $\Pi(\varepsilon_\perp)$ due to the focusing effect does not contribute the close encounter yield, since the main contribution to the yield at the position interested now originates from the particles with much lower transverse energy $\varepsilon_\perp$ than the boundary transverse energy $\varepsilon_\perp^B$.

Thus it is concluded that the continuum approximation may give good results for location of atoms inside the channel.

References

1. S. T. Picraux, "New Uses of Ion Accelerators," ed. by J. F. Ziegler (Plenum Press, New York, 1975) p. 229.
2. K. Tachibana, K. Morita and N. Itoh, Solid State Commu. 9, 1425 (1971).
3. R. B. Alexander and J. M. Poate, Rad. Effects 12, 211 (1972).
4. B. Domeij, G. Fladda and N. G. E. Johansson, Rad. Effects 6, 155 (1970).
5. J. U. Andersen, O. Andreasen, J. A. Davies and E. Uggerhøj, Rad. Effects 7, 25 (1971).
6. J. U. Andersen, E. Laegsgaard and L. C. Feldman, Rad. Effects 12 , 219 (1972).
7. S. T. Picraux, W. L. Brown and W. M. Gibson, Phys. Rev. B6, 1382 (1972).
8. R. B. Alexander, P. T. Callaghan and J. M. Poate, Phys. Rev. B9, 3022 (1974).
9. K. Morita and H. D. Carstanjen, Rad. Effects (in print).
10. M. T. Robinson and O. S. Oen, Phys. Rev. 132, 2385 (1963).
11. D. Van Vliet, Rad. Effects 10, 137 (1971).
12. J. H. Barrett, Phys. Rev. B3, 1527 (1971).
13. D. V. Morgan and D. Van Vliet, Rad. Effects 12, 203 (1972).
14. H. D. Carstanjen and R. Sizmann, Rad. Effects 12 , 225 (1972).

15. K. Morita, Rad. Effects (in print)

16. J. Lindhard,
Mat. Fys. Medd. Dan. Vid. Selsk. 34, No. 14 (1965).

17. J. U. Andersen,
Mat. Fys. Medd. Dan. Vid. Selsk. 36, No. 7 (1967).

18. K. Tachibana, Rad. Effects 19, 135 (1973).

19. J. H. Barrett, Phys. Rev. Letters 31, 1542 (1973).

20. H. E. Schiøtt, E. Bonderup, J. U. Andersen and H. Esbensen, "Atomic Collisions in Solids V," ed. by S. Datz, B. R. Appleton and C. D. Moak (Plenum Press, New York, 1975) p. 843.

21. G. Molière, Z. Naturforsch. A2, 133 (1947).

22. C. Erginsoy, Phys. Rev. Letters 15, 360 (1965).

23. B. R. Appleton, J. H. Barrett, T. S. Noggle and C. D. Moak, Rad. Effects 13, 171 (1971).

24. L. M. Howe and S. Schmid, Can. J. Phys. 49, 2321 (1971).

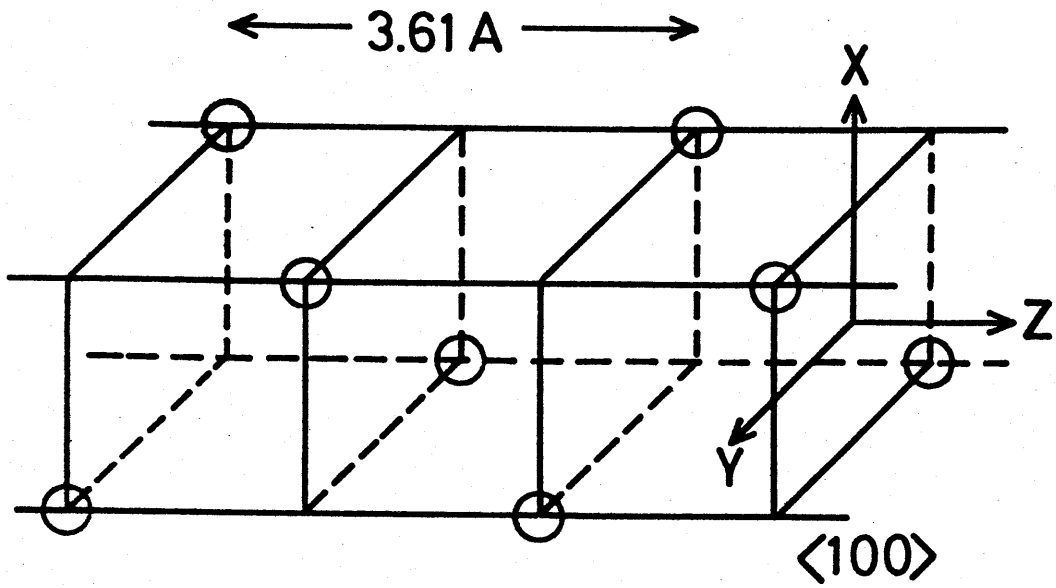

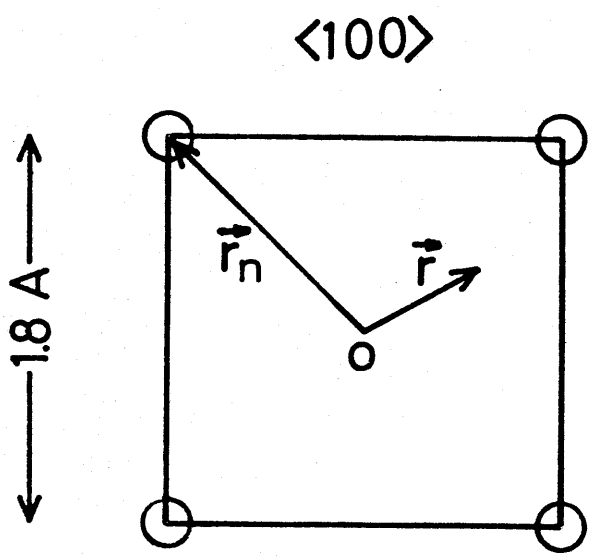

Fig. 2.1 Geometry of the <100> channel of Cu.

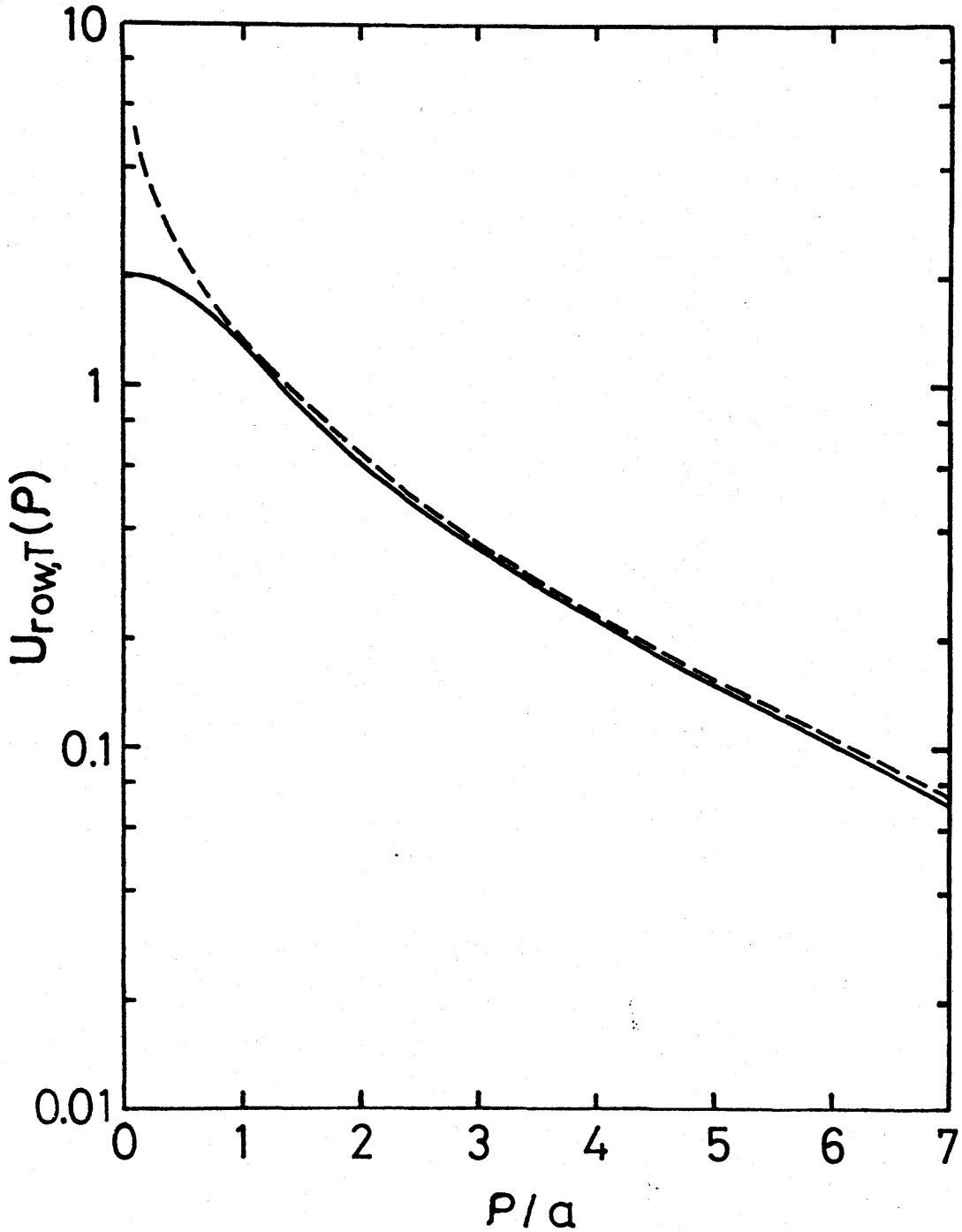

Fig. 2.2 Thermally modified row potential $U_{row,T}(\rho)$ as a function of the distance ρ from the string for He^+ in the <100> string of Cu at room temperature ($\rho_\perp$=0.12 A) (solid line). $U_{row,T}(\rho)$ is expressed in the reduced unit. The static row potential $U_{row}(\rho)$ in the reduced unit is also shown (broken line).

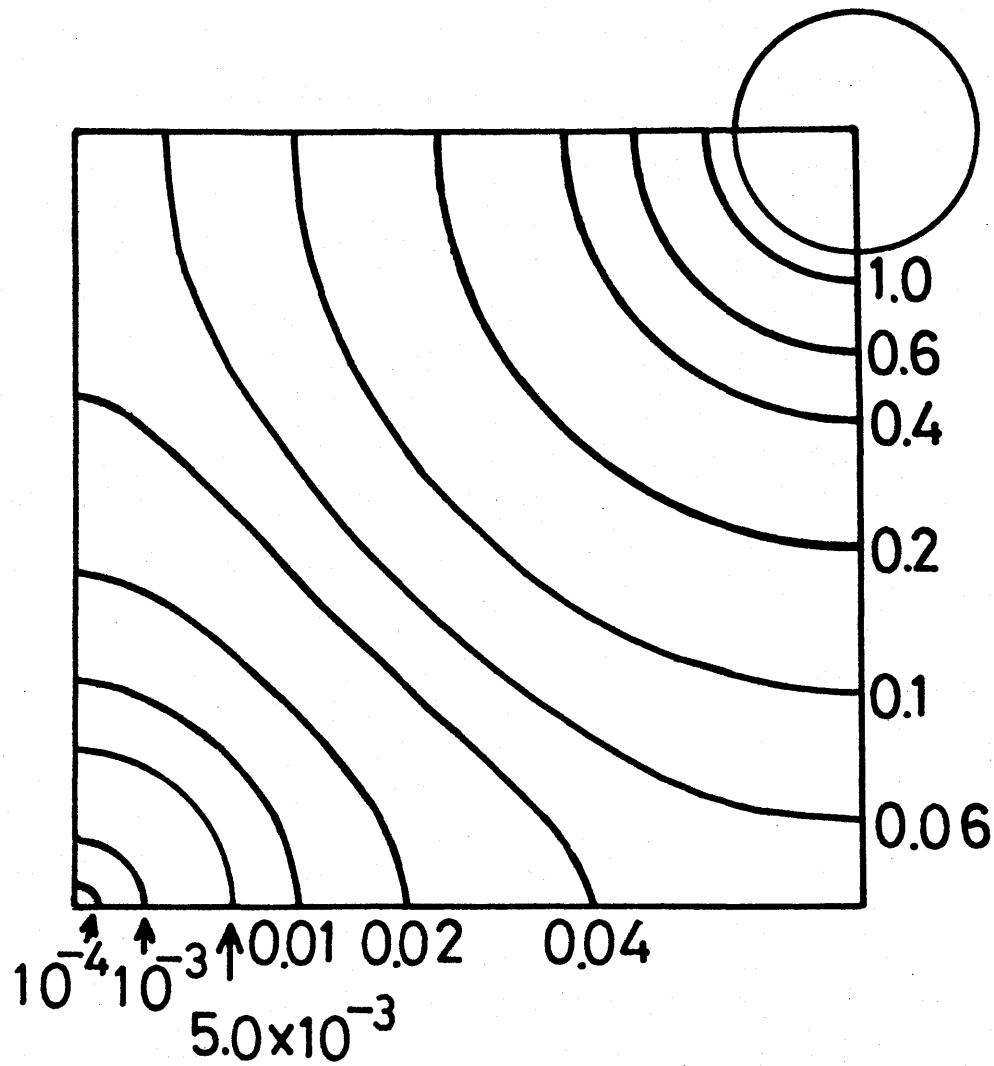

Fig. 2.3 Equi-potential contours for He^+ in the <100> channel of Cu. The transverse potential is expressed in the reduced unit (231 eV). Only one quarter of the channel is shown. The Cu atom is indicated by an open circle.

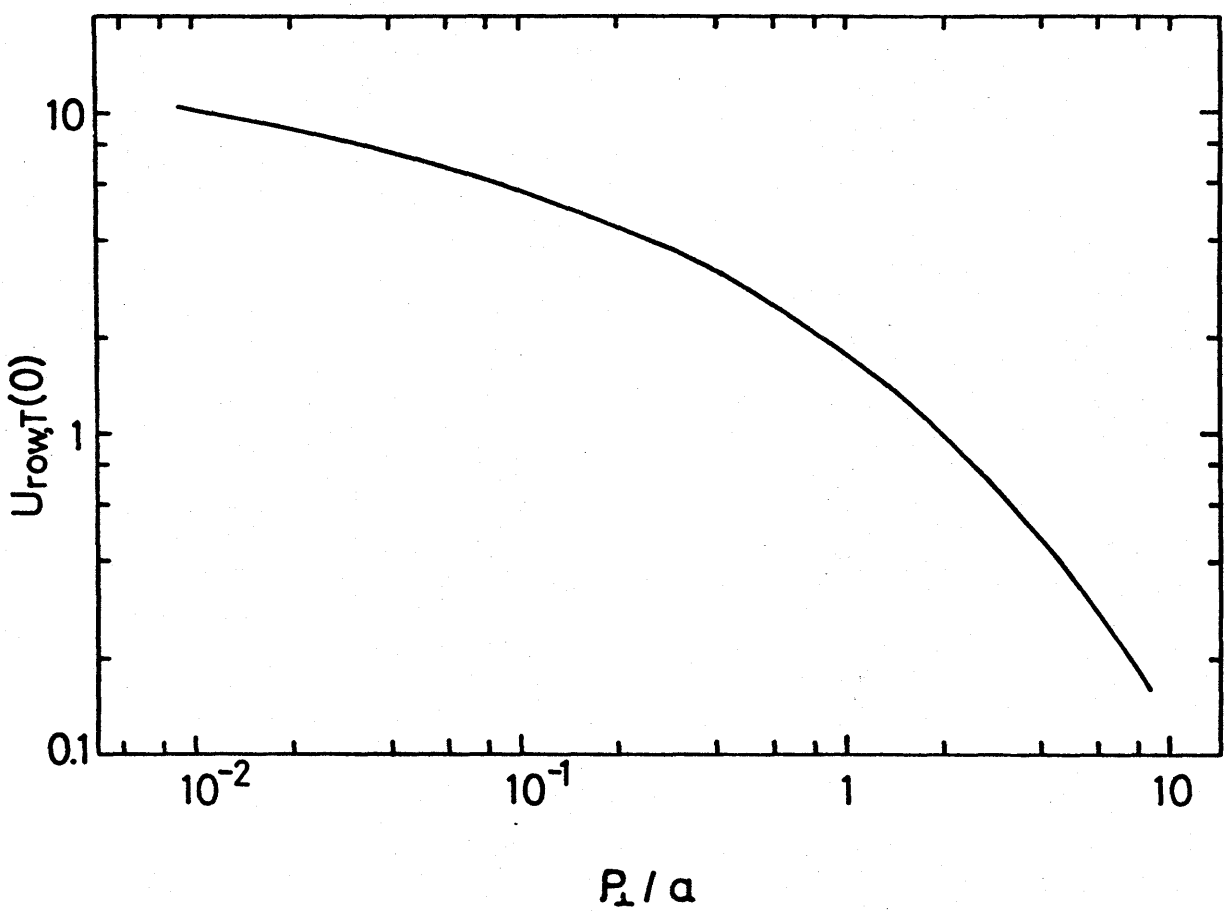

Fig. 2.4 Value of $U_{row,T}(0)$ as a function of the thermal vibration amplitude $\rho_\perp$ normal to the string divided by the Thomas-Fermi radius a.

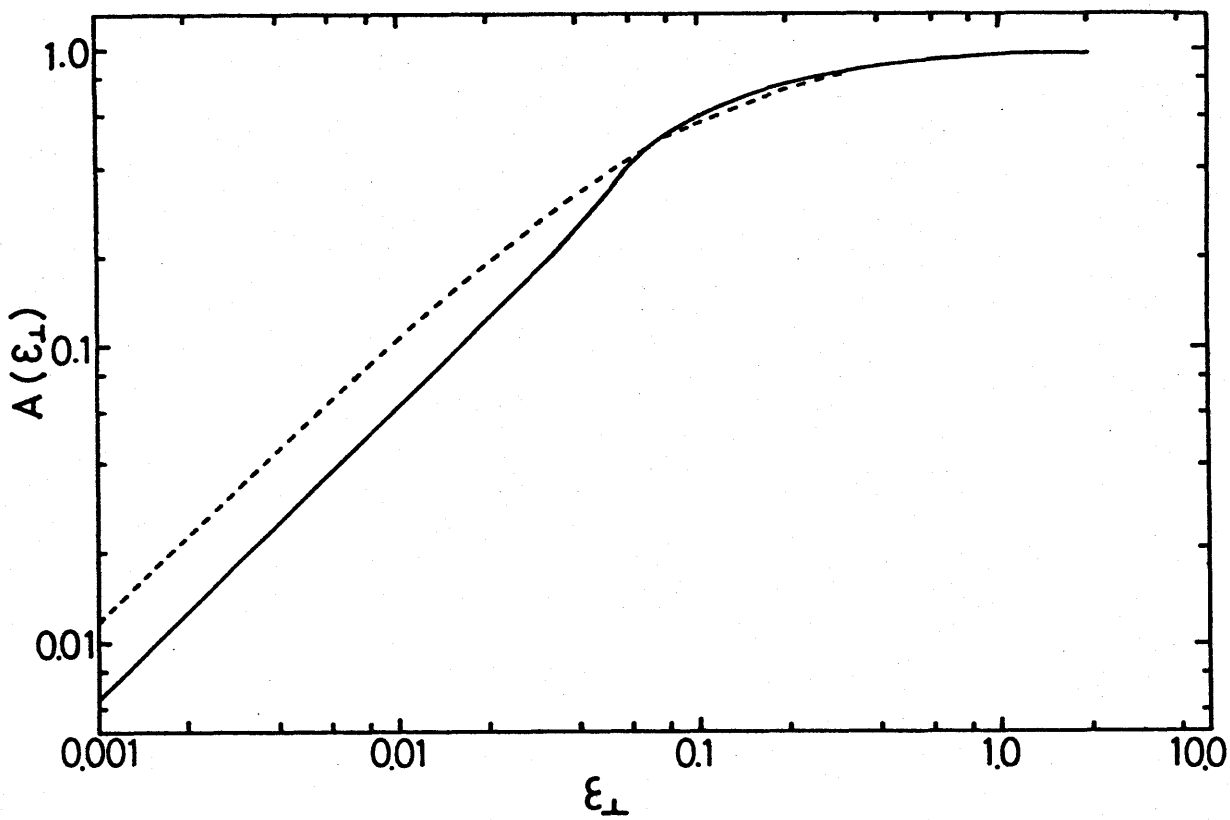

Fig. 2.5 Accessible area $A(\varepsilon_\perp)$ as a function of the reduced transverse energy $\varepsilon_\perp$ for He^+ in the <100> channel of Cu. The accessible area is normalized by the area of the channel. The solid line and the broken line are the results of the four string calculation and one string calculation, respectively.

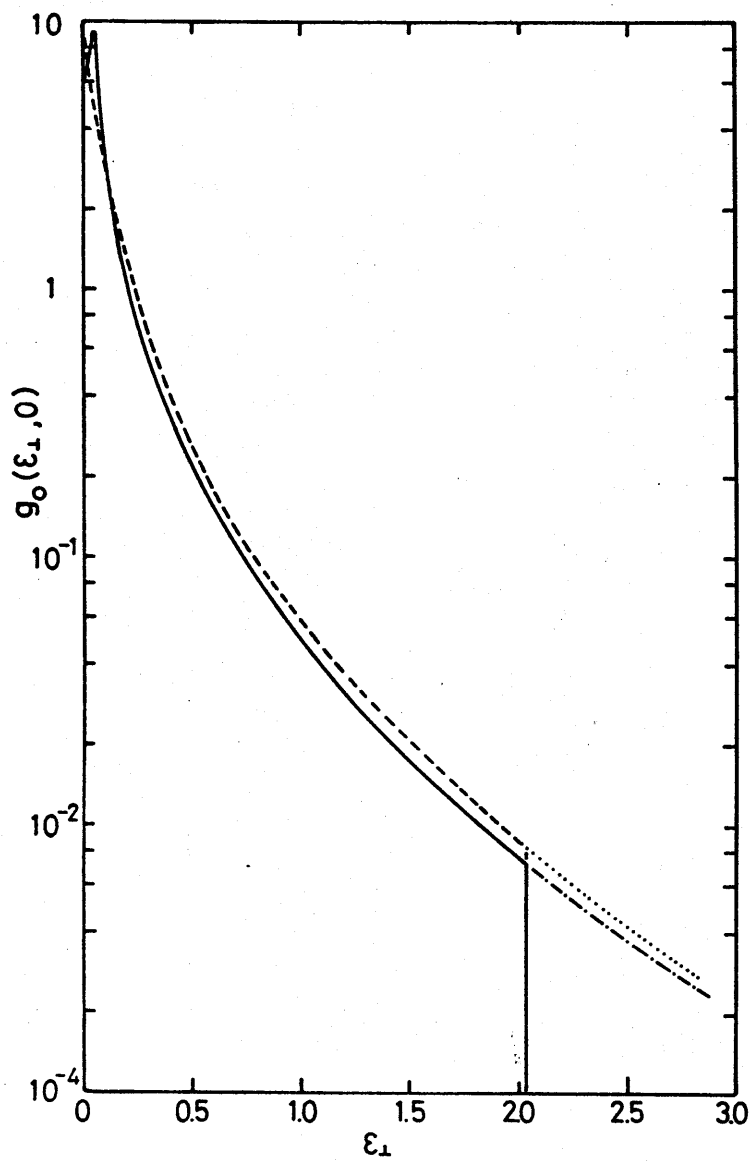

Fig. 2.6 Initial distribution $g_o(\varepsilon_\perp, 0)$ for He^+ in the <100> channel of Cu as a function of the reduced transverse energy $\varepsilon_\perp$. The solid and broken lines are the results of the four string calculation and the one string calculation, respectively. The dot-dash and dotted lines are the results obtained with the four static row potential and the one static row potential, respectively.

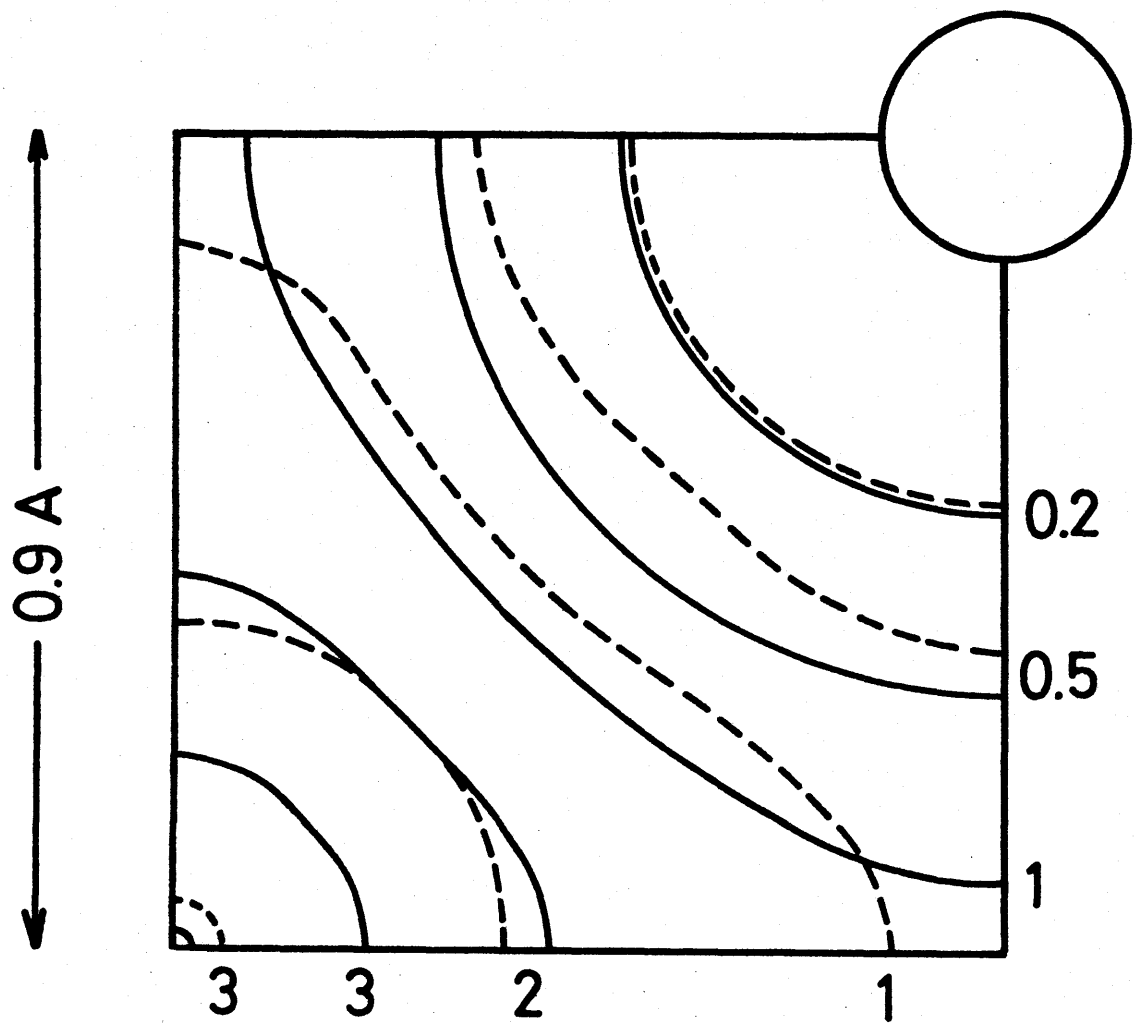

Fig. 2.7 Equi-flux contours for 1 MeV He^+ in the <100> channel of Cu at the incident angle $\Psi_{in}=0°$. The solid lines are the results obtained with the present analytical calculation. The broken lines are the results of the simulation calcuation obtained by Van Vliet. Only one quarter of the channel is shown but the rest of the profile is symmetric. The Cu atom is indicated by an open circle.

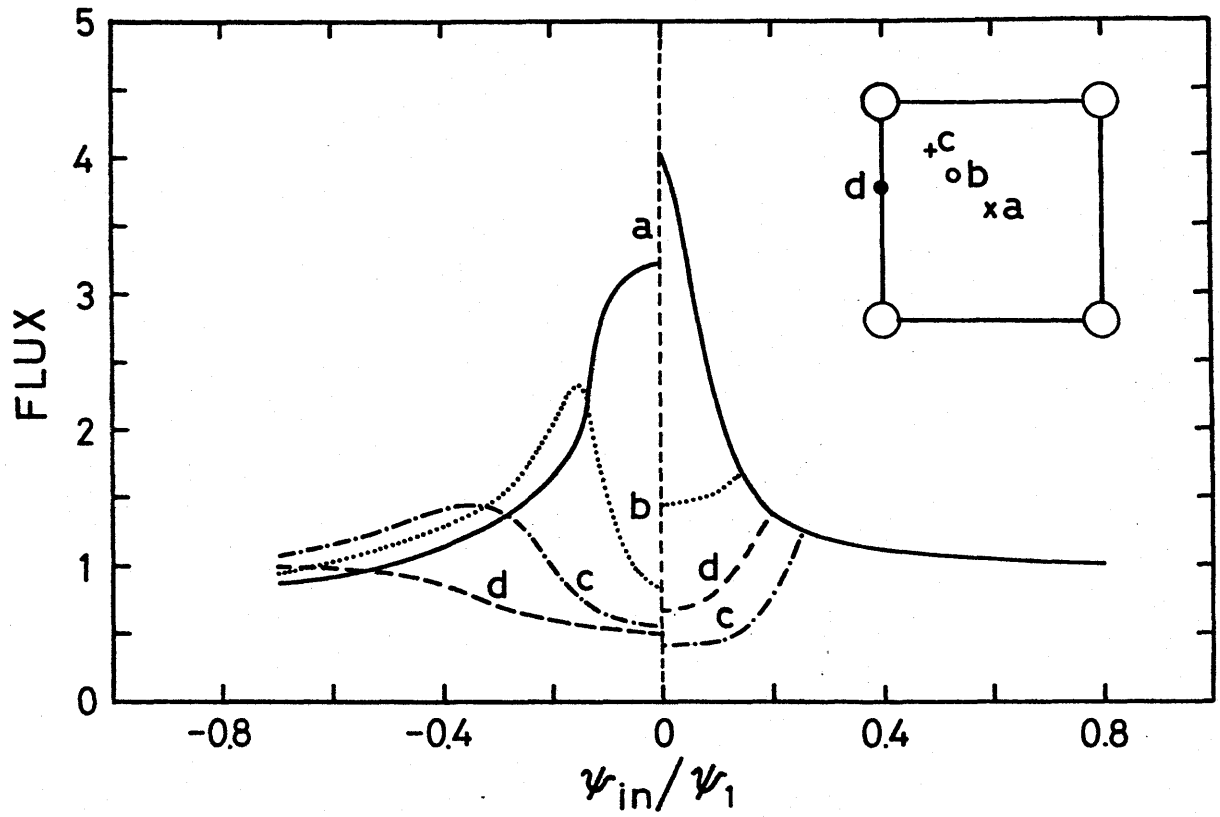

Fig. 2.8 Flux for 1.5 MeV He^+ in the <100> channel of Cu, as a function of the incident angle ψ_{in} normalized by Lindhard's characteristic angle ψ_1, at various positions in the channel, which are indicated in the figure. The position (a) is the center of the channel. The distance from the center of the channel to the positions (b) and (c) are 0.45 A and 0.7 A, along the diagonal, respectively. The distance from the string to the position (d) is 0.7 A. The right-hand side is the results of the present analytical calculation and the left-hand side is those of the simulation calculation by Morgan et al..

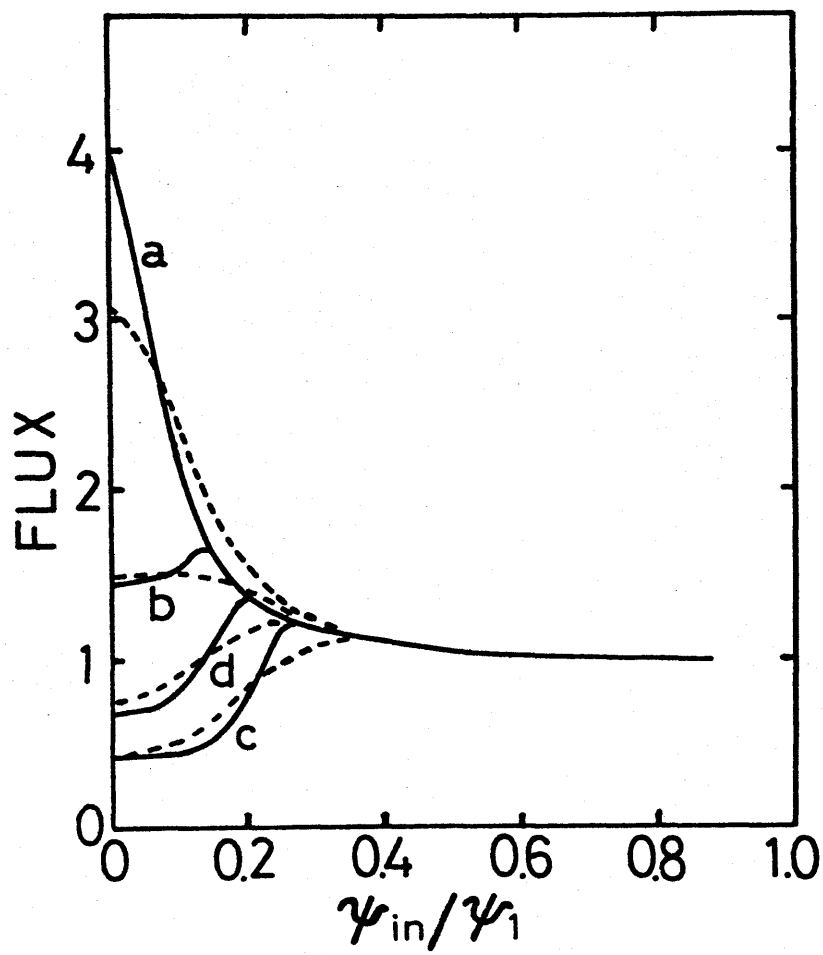

Fig. 2.9 Angular dependence of the flux, in which the angular spread $\Delta\psi$ of the incident beam was taken into account, for 1.5 MeV He^+ in the <100> channel of Cu at the same positions as indicated in Fig. 2.7. The solid line and broken line are the results for $\Delta\psi=0$ and $\Delta\psi=0.1\,\psi_1$, respectively. Here ψ_1 is Lindhard's characteristic angle.

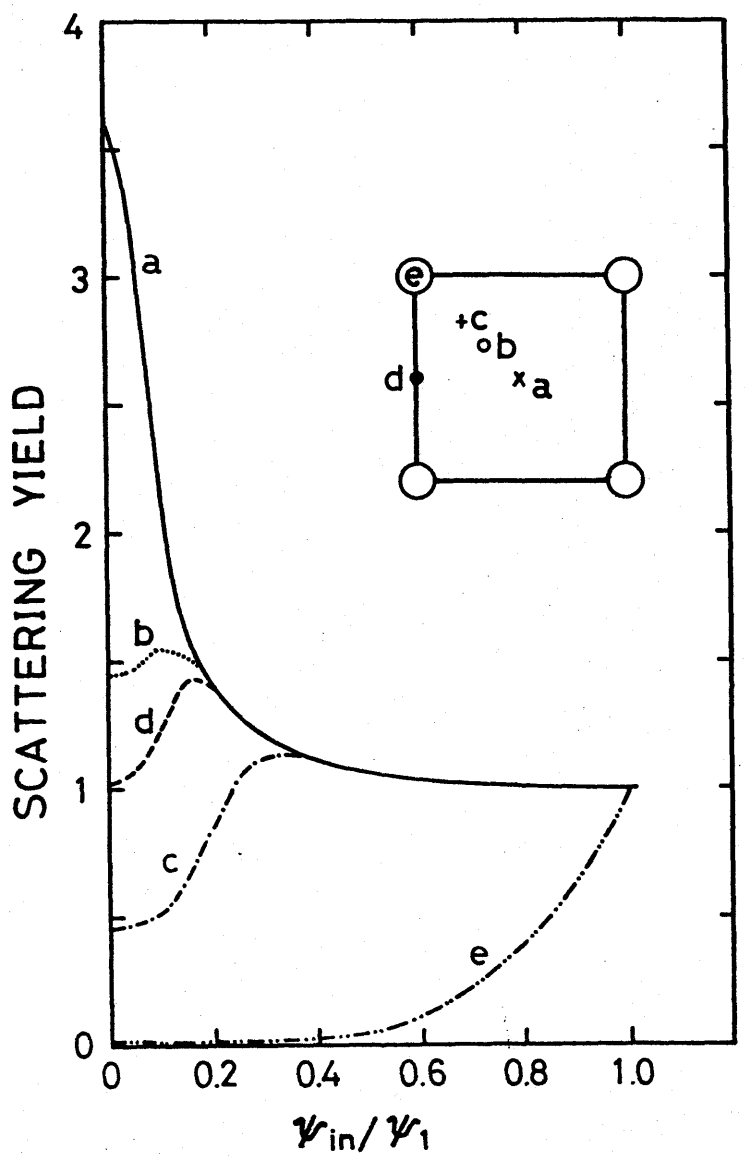

Fig. 2.10 Angular dependence of the scattering yield from the atoms located at various positions indicated in the figure, for He^+ in the <100> channel of Cu at room temperature. The positions (a), (b), (c) and (d) are the same as those in Fig. 2.7. The incident angle ψ_{in} is normalized by Lindhard's characteristic angle ψ_1.

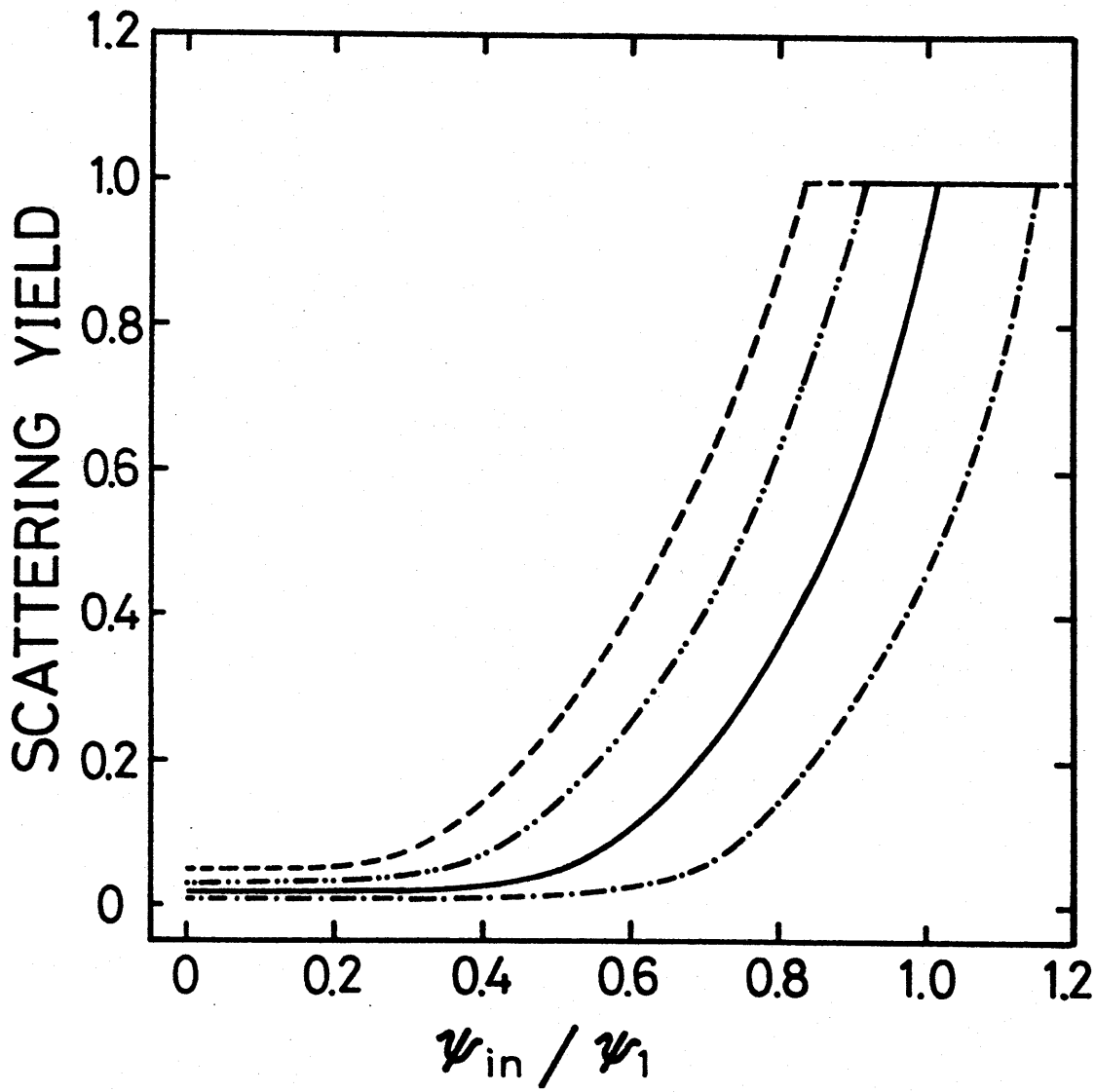

Fig. 2.11 Angular dependence of the scattering yield from the lattice atoms for 1.5 MeV He^+ in the <100> channel of Cu, at various temperature. The incident angle ψ_{in} is normalized by Lindhard's characteristic angle ψ_1. The broken, double dot-dash, solid and dot-dash lines are the results for the temperature T=865 K($\rho_\perp$=0.2 A), 550 K ($\rho_\perp$=0.16A), 300 K($\rho_\perp$=0.12 A) and 100 K ($\rho_\perp$=0.08 A), respectively.

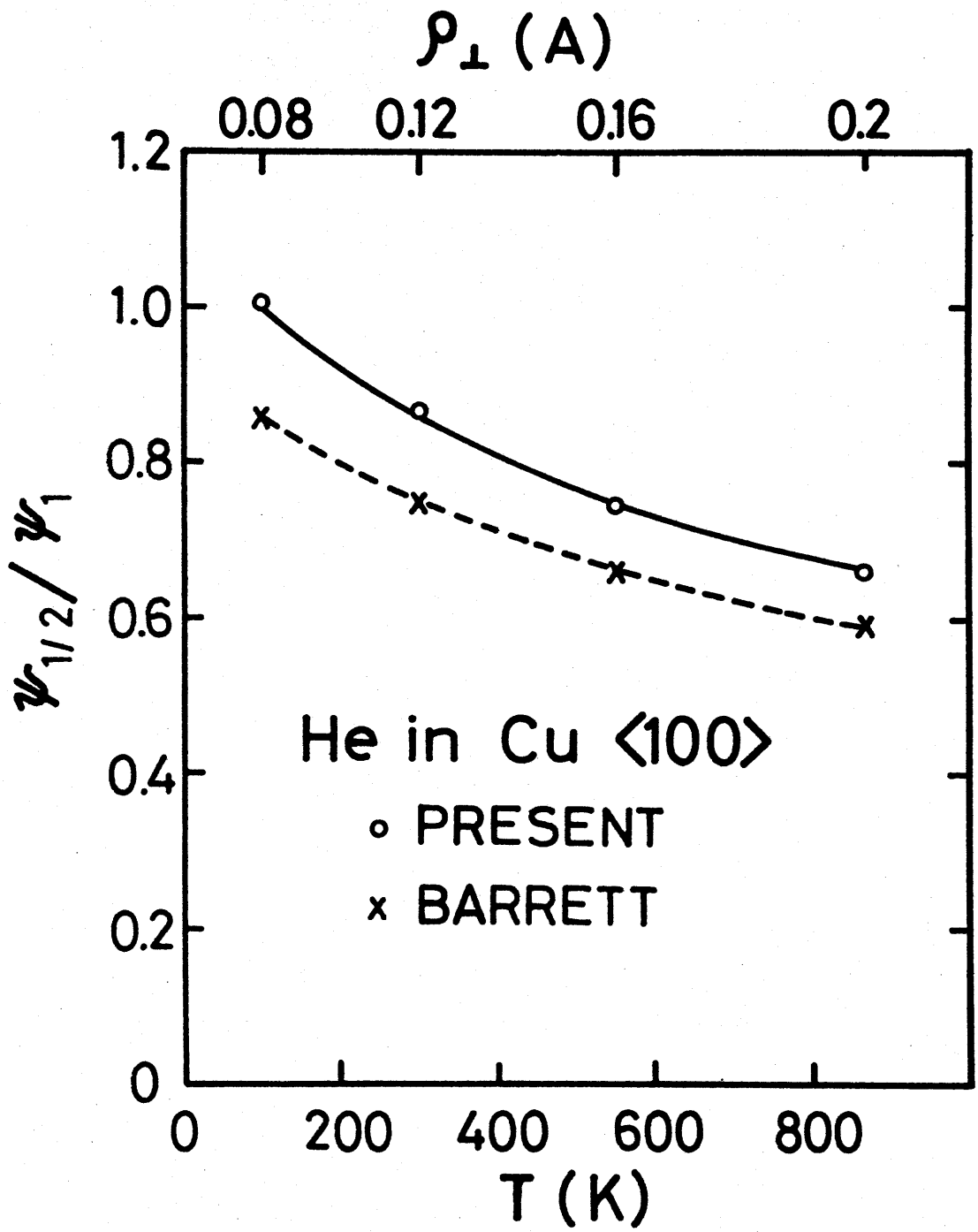

Fig. 2.12 Temperature dependence of the half-angle $\psi_{1/2}$ normalized by Lindhard's characteristic angle ψ_1, for He^+ in the <100> channel of Cu. The open circles and crosses are the results obtained with the present analytical calculation and the simulation calculation by Barrett, respectively.

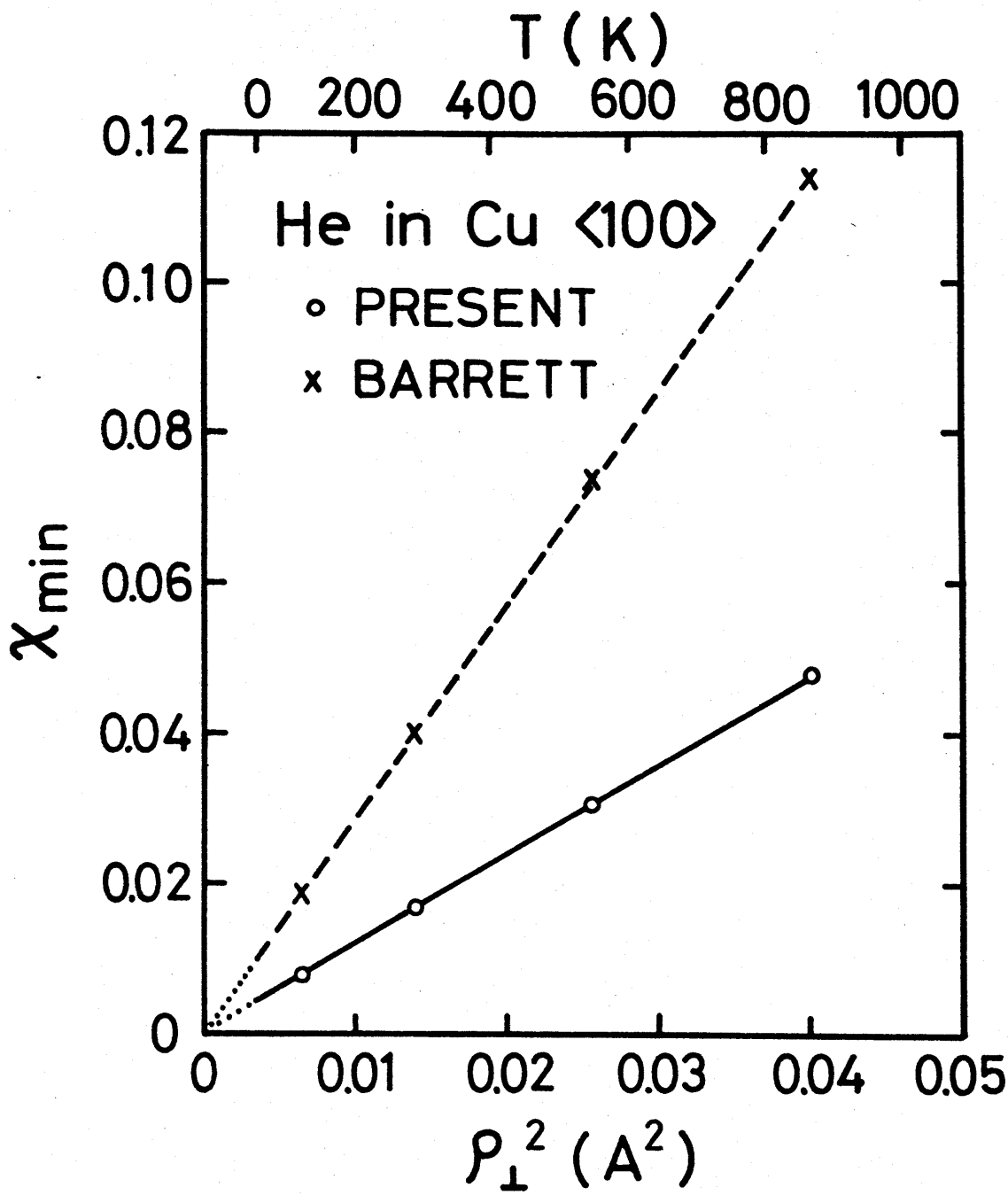

Fig. 2.13 Minimum yield χ_{min} as a function of the square of the thermal vibration amplitude $\rho_\perp$ normal to the string for He^+ in the <100> channel of Cu. The open circles and crosses are the results of the present analytical calculation and the simulation calculation by Barrett, respectively.

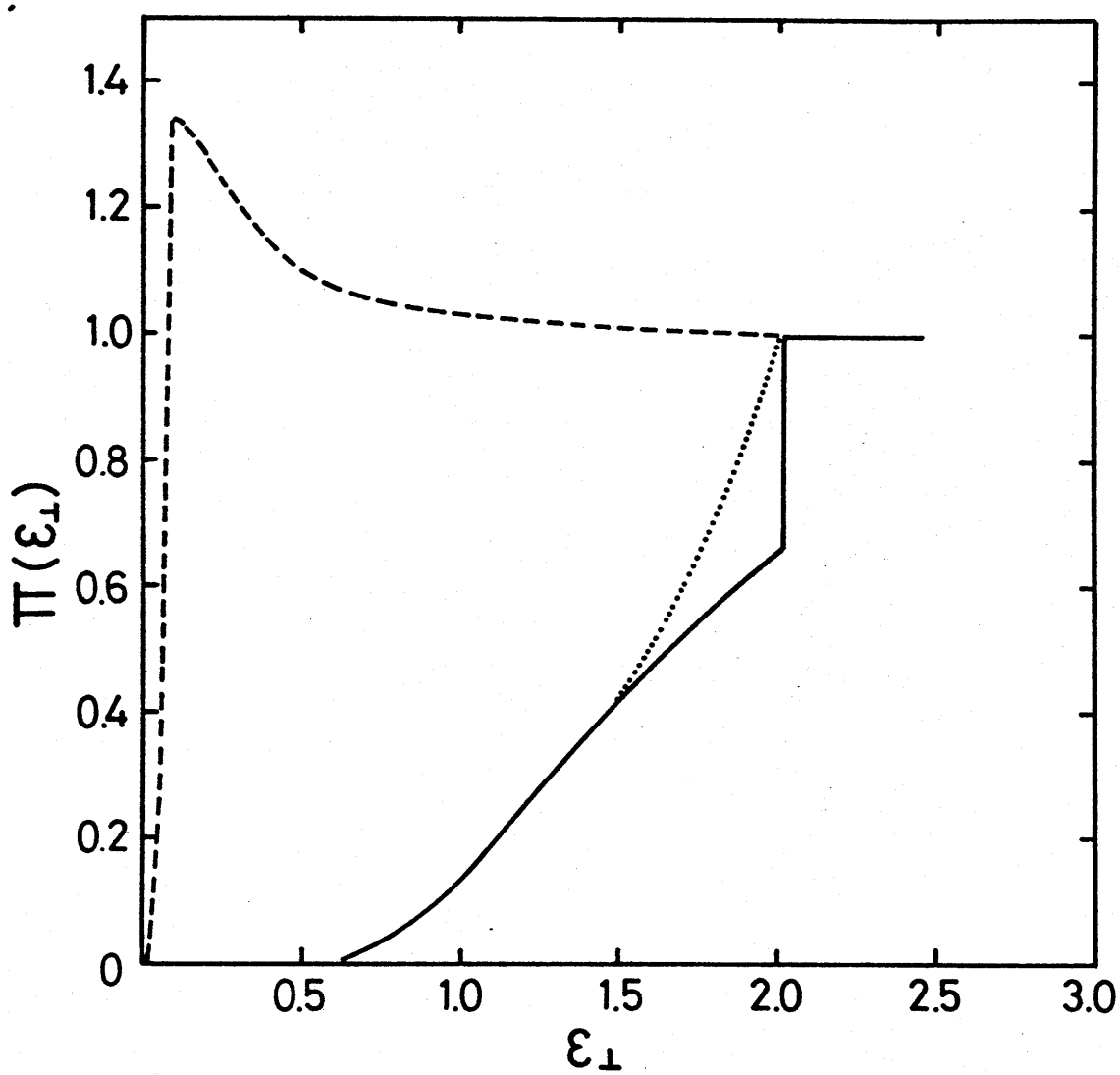

Fig. 2.14 Effectiveness factor $\Pi(\varepsilon_\perp)$ as a function of the reduced transverse energy $\varepsilon_\perp$ for He^+ in the <100> channel of Cu at room temperature. The solid line and the dotted line are obtained with the approximate and the correct thermally modified row potential, respectively, for lattice atoms. The broken line is the effectiveness factor for the atoms located at the position $\vec{s}$=(0.4 A, 0.4 A).

CHAPTER III

EFFECTS OF LATTICE DEFECTS ON THE CHANNELED PARTICLE DISTRIBUTION AND ON THE DECHANNELING

3.1 Introduction

In additon to the determination of the impurity location[1] as described in the previous chapter, measurements of dechanneling (the depth dependence of the close encounter yield) have been employed for the investigation of the defect distribution in ion-implanted layers[2 - 11] and defect structures induced by irradiation.[12, 13] In those studies, it is necessary to know how the defects influence the flux distribution of the channeled particles or the particle distribution in the transverse energy and the close encounter yield, such as Rutherford scattering yield, both from the lattice atoms and from the defects.

The effects of lattice defects (displaced atoms) on the channeled particles have been first treated by Bøgh.[3] He has considered that either single scattering or multiple scattering with displaced atoms brings the channeled particles into random particles (dechanneling) and increases the random fraction, i. e., the close encounter yield from the lattice atoms. In the single scattering model, the particle distribution is assumed to be not modified by the presence of defects. In the multiple scattering model, the particle distribution is

assumed to be a gaussian form with respect to the crossing angle between the particle velocity and a major crystal axis. Later, plural scattering model has been also used for the dechanneling by defects.[7] In neither of these models, the interference effect between the scattering with defects and the scattering with electrons and thermally vibrating lattice atoms or the modification of the particle distribution by defects has been disregarded. The interference effect combined with the modification of the particle distribution should increase the random fraction considerably. Moreover the angular dependence of the flux distribution may be affected by the presence of defects.

In this chapter, the modification of the particle distribution in the transverse energy has been calculated for KCl using a diffusion equation, in which the diffusion coefficients caused by elastic collisions with defects as well as collisions with electrons and the thermally vibrating lattice atoms are included. The modification of the particle distribution caused by defects and the interference effect are discussed. The dechanneling caused by defects is also obtained and compared with the results obtained with the single, multiple and plural scattering models. The change in the flux distribution caused by defects was briefly described. Since the present model treats the dechanneling by defects using a diffusion equation, it is refer-

ed as diffusion model.

3.2 Method of Calculation

3.2.1 Distribution Function and Random Fraction

As stated in Chapter II, the channeled particles are well described by their transverse energies. The effects of displaced atoms on the particle distribution are treated in the transverse energy space. The assumptions of the statistical equilibrium[14] and of the gradual change of the transverse energy lead to the following diffusion equation[15, 16]:

$$\frac{\partial g(\varepsilon_\perp, z)}{\partial z} = \frac{\partial}{\partial \varepsilon_\perp}\left[A(\varepsilon_\perp)D(\varepsilon_\perp)\frac{\partial}{\partial \varepsilon_\perp}\left\{\frac{g(\varepsilon_\perp, z)}{A(\varepsilon_\perp)}\right\}\right] . \quad (3.1)$$

Here $A(\varepsilon_\perp)$ is the accessible area defined in Sec. 2.3.2 and $D(\varepsilon_\perp)$ is the total diffusion coefficient. The energy is again expressed in the unit of the characteristic transverse energy. Then the distribution function $g(\varepsilon_\perp, z)$ of the particles in the transverse energy $\varepsilon_\perp$ at a depth z from the crystal surface is obtained by solving the above diffusion equation. In this equation, the energy loss of the particles is neglected. Since the dechanneling experiments are usually made for $\psi_{in} = 0$, only the case for $\psi_{in} = 0$ is treated here. Thus the term of ψ_{in} is omitted in the distribution function.

The transverse potential $U(\vec{r})$ was approximated by the one string potential obtained with the Molière

approximation[17] to the Thomas-Fermi potential (Eq.(2.3)). In the one string approximation, the area A_o per channel or string (i.e., the unit cell) is equal to $(Nd)^{-1}$, where N is the host atom density and d is interatomic distance in the string. Conventionally, the assumption that $U(r_o) = 0$ was used. Here $r_o = (A_o/\pi)^{1/2}$ is the radius of the unit cell (see Fig. 3.1). The transverse potential $U(\rho)$ at a distance ρ from the string becomes

$$U(\rho) = U_{row}(\rho) - U_{row}(r_o). \qquad (3.2)$$

After solving the diffusion equation, the random fraction χ_R may be obtained by Eq.(2.10). Since the purpose of this chapter is to obtain the depth dependence of χ_R, the effectiveness factor[18] $\pi(\varepsilon_\perp)$ is approximated by

$$\pi(\varepsilon_\perp) = \begin{cases} 0 & \varepsilon_\perp < \varepsilon_\perp^c \\ 1 & \varepsilon_\perp \geqq \varepsilon_\perp^c \end{cases} , \qquad (3.3)$$

where $\varepsilon_\perp^c$ is the critical transverse energy. $\varepsilon_\perp^c$ is given by

$$\varepsilon_\perp^c \simeq \varepsilon \psi_{1/2}^2 , \qquad (3.4)$$

with the experimental or the theoretical[18] half-angle $\psi_{1/2}$ of the channeling dip. Here ε is the energy of the incident particle expressed in the reduced unit.

Then χ_R is calculated by

$$\chi_R(z) = \int_{\varepsilon_\perp^c}^{\infty} g(\varepsilon_\perp, z)d\varepsilon_\perp \quad . \qquad (3.5)$$

3.2.2 Diffusion Coefficient

The diffusion coefficient $D_d(\varepsilon_\perp)$ caused by scattering with lattice defects or the displaced atoms was calculated by the integral:

$$D_d(\varepsilon_\perp) = \frac{1}{2} \int_0^{\varepsilon_\perp^U} (\varepsilon_\perp - \varepsilon_\perp')^2 P_r(\varepsilon_\perp \rightarrow \varepsilon_\perp')d\varepsilon_\perp' \quad , \qquad (3.6)$$

where $P_r(\varepsilon_\perp \rightarrow \varepsilon_\perp')$ is the probability for the particles with the transverse energy $\varepsilon_\perp$ to be scattered to $\varepsilon_\perp'$, and $\varepsilon_\perp^U$ is the upper limit of the integral, which is going to be discussed below. The scattering probability $P_r(\varepsilon_\perp \rightarrow \varepsilon_\perp')$ was calculated in the following method. Suppose that an atom in the string is displaced by a distance S. Referring to Fig. 3.2, the particles with the transverse energy $\varepsilon_\perp$ are generated at the position (R, θ) on the half-way plane between the displaced atom and the preceding atom in the string, to a direction determined by the azimuthal angle φ. The crossing angle ψ between the direction of the particle and the string was determined by

$$\psi = [(\varepsilon_\perp - U(\rho))/\varepsilon]^{1/2}, \text{ where } \rho = [R^2 + S^2 + 2RS\cos\theta]^{1/2} . \tag{3.7}$$

Next, the scattering angle of each particle was calculated using the impact approximation. The Molière potential[16] was also employed for the interaction potential between the particle and the displaced atom. The crossing angle ψ', the azimuthal angle φ' and the transverse energy $\varepsilon_\perp'$ on the next half-way plane was obtained. The distribution in $\varepsilon_\perp'$ at the next half-way plane was then calculated for particles with a given transverse energy $\varepsilon_\perp$ at the preceding half-way plane and the transition probability was obtained. In calculating the diffusion coefficient by using Eq.(3.6), the upper limit $\varepsilon_\perp^U$ of the integral was taken from 2.4 $\varepsilon_\perp^c$ to 6.5 $\varepsilon_\perp^c$. Discussion on the range of the integral is made in the next section.

The diffusion coefficient $D_p(\varepsilon_\perp)$ for the scattering by electrons and thermally vibrating lattice atoms (lattice vibrations) has been calculated by the equation:

$$D_p(\varepsilon_\perp) = \frac{1}{A(\varepsilon_\perp)} \int_0^{\varepsilon_\perp} A(\varepsilon_\perp') \frac{d\langle\varepsilon_\perp'\rangle}{dz} d\varepsilon_\perp' , \tag{3.8}$$

and the analytical expression $\frac{d\langle\varepsilon_\perp'\rangle}{dz}$ derived by Lindhard[14] and Bonderup et al.[15] (Eq.(19) of ref. (15)). Since $A(\varepsilon_\perp')$ is nearly constant for large value of $\varepsilon_\perp'$, where $\frac{d\langle\varepsilon_\perp'\rangle}{dz}$ has appreciable magnitudes, Eq.(3.8) is approximated by

$$D_p(\varepsilon_\perp) = \int_0^{\varepsilon_\perp} \frac{d\langle\varepsilon_\perp'\rangle}{dz}\, d\varepsilon_\perp' \quad . \qquad (3.9)$$

$D_p(\varepsilon_\perp)$ calculated with Eq.(3.9) is about 10 % larger than that calculated with Eq.(3.8) for not too low transverse energy. The nuclear contribution (i.e., the contribution of lattice vibrations) to $D_p(\varepsilon_\perp)$ depends on the square of the thermal vibration amplitude $\rho_\perp$ perpendicular to the atomic row, while the electronic contribution is independent of $\rho_\perp$.

The total diffusion coefficient is given by

$$D(\varepsilon_\perp) = D_p(\varepsilon_\perp) + c\, D_d(\varepsilon_\perp) \ , \qquad (3.10)$$

where c is the fractional concentration of the displaced atoms. $D(\varepsilon_\perp)$ for $\varepsilon_\perp \geqq \varepsilon_\perp^c$ was assumed to have the constant value $D(\varepsilon_\perp^c)$.

3.2.3 Accessible Area and Initial Distribution

In the one string approximation, the accessible area $A(\varepsilon_\perp)$ is calculated by

$$A(\varepsilon_\perp) = (\pi r_o^2 - \pi\rho^2)/(\pi r_o^2) \quad , \qquad (3.11)$$

where $\pi r_o^2 = (Nd)^{-1}$ is the area of the unit cell and ρ is the distance from the string given by the relation: $\varepsilon_\perp = U(\rho)$ (see Fig. 3.1). The accessible area was

normalized by the area of the unit cell. In order to prevent the divergence of the particle distribution, the lowest value of $A(\varepsilon_\perp)$ was taken as $A(\Delta\varepsilon_\perp^{th})$, where $\Delta\varepsilon_\perp^{th}$ is the average fluctuation of the transverse energy due to the thermal vibration with the average amplitude $\rho_\perp$ and is given by $U(\rho_\perp) \simeq U_{row}(\rho_\perp)$.

The initial distribution $g(\varepsilon_\perp, 0)$ was obtained with Eq.(2.14). In calculating $g(\varepsilon_\perp, 0)$ with Eq.(2.14), the transverse energy $\delta\varepsilon_\perp = \varepsilon(\Delta\psi)^2$ due to the angular spread $\Delta\psi$ of the initial beam was added. Although the one string approximation induces an error of 10 % in $g(\varepsilon_\perp, 0)$ and an error of a factor of 2 in $A(\varepsilon_\perp)$ for the low transverse energies, the obtained results are not affected appreciably.

The numerical calculation was made for 1.5 MeV protons incident along <100> direction of KCl crystal, which has nearly a simple cubic structure, at room temperature. The depth dependence of the random fraction was also calculated with the single, multiple and plural scattering models in the same crystal and the results were compared with that of the diffusion model.

3.3 Results and Discussion

3.3.1 Diffusion Coefficient

In order to calculate the transition probability $P_r(\varepsilon_\perp \rightarrow \varepsilon_\perp')$, the three parameters R, θ and φ were varied independently in steps; R:(1-20 ~ 30)a/20, θ: (1-15) $\pi/15$, φ: (1-30) $\pi/15$ (see Fig. 3.2). Here a is

the Thomas-Fermi radius. The weighting factor R was multiplied in the integral to obtain P_r. Figure 3.3 shows the diffusion coefficient $D_d(\varepsilon_\perp)$ per unit fractional concentration of displaced atoms in the case that 1.5 MeV protons are incident along a <100> string of KCl, as a function of the reduced transverse energy $\varepsilon_\perp$, for various values of displacement S.

The error in $D_d(\varepsilon_\perp)$ was estimated by varying the range R and the step of the transverse energy $\varepsilon_\perp'$. According to these estimates, it is shown that the error of $D_d(\varepsilon_\perp)$ is within 10 % for $\varepsilon_\perp > U(S)$ and about 50 % for $\varepsilon_\perp \leqq U(S)$, where U(S) is the value of the transverse potential at the position S. Since the value of $D(\varepsilon_\perp)$ for $\varepsilon_\perp \leqq U(S)$ is small as shown in the figure, the error 50 % makes only a small contribution to the results of preceeding calculation. The origin of R was also slightly diviated from the position S to see whether the choice of the origin had introduced a systematic error. The error of $D_d(\varepsilon_\perp)$ thus obtained is a few % at $\varepsilon_\perp < U(S)$ and substantially zero for $\varepsilon_\perp > U(S)$.

One of the crucial problem in the estimation of the diffusion coefficient is the choice of the upper limit $\varepsilon_\perp^U$ of the integral as described previously. Since the diffusion equation mainly treat the particle distribution for $\varepsilon_\perp < \varepsilon_\perp^c$, the direct scattering to the transverse energy much larger than $\varepsilon_\perp^c$ should not be taken into the diffusion coefficient. On the other hand, to take the upper limit as $\varepsilon_\perp^c$ may lead to an un-

derestimate of the dechanneling rate, since the diffusion equation includes the contribution of the rechanneling from the region outside $\varepsilon_\perp^c$. In the present study the upper limit $\varepsilon_\perp^U$ was taken from (2.4 ~ 6.5) $\varepsilon_\perp^c$, where $\varepsilon_\perp^c = \varepsilon \Psi_{1/2}^2 = 0.62$ at room temperature. The diffusion coefficient calculated with the range of the upper limit described above agrees each other within a factor of 3. Figure 3.3 shows the result obtained with the upper limit of 6.5 $\varepsilon_\perp^c$.

It is to be noted that $D_d(\varepsilon_\perp)$ increases suddenly as $\varepsilon_\perp$ increases and is strongly peaked at a certain critical value of $\varepsilon_\perp$, which nearly equals to U(S). The sudden increase takes place since particles with smaller $\varepsilon_\perp$ than U(S) cannot come close to the string within the distance S. The large scattering probability at $\varepsilon_\perp \simeq U(S)$ is responsible for the peak. Above the critical value, $D_d(\varepsilon_\perp)$ increases gradually with increasing $\varepsilon_\perp$. In this region, as $\varepsilon_\perp$ increases the scattering by the displaced atom occurs with larger crossing angle, resulting in a larger change in the transverse energy; therefore the scattering probability at large energy differences becomes large.

Figure 3.4 shows the components of the diffusion coefficient $D(\varepsilon_\perp)$ caused by electrons(D_e), lattice vibrations(D_n) and displaced atoms (S = 7a) for c = 1 % (D_d), at room temperature. At lower transverse energies the defect contribution dominates, while at higher trans-

verse energies the nuclear and electronic contribution dominates. If c increases further, defect contrinution dominates over with range of the transcerse energy.

3.3.2 Distribution Function

Figure 3.5 shows the accessible area $A(\varepsilon_\perp)$, which was normalized by the area of the unit cell. As described in Sec. 3.2.3, the lowest value of the accessible area was taken as $A(U_{row}(\rho_\perp))$, where $\rho_\perp$ is the thermal vibration amplitude normal to the atomic row($\rho_\perp$ = 0.213 A at room temperature). It is seen from the figure that $A(\varepsilon_\perp)$ increases rapidly with increasing $\varepsilon_\perp$.

The diffusion equation was solved numerically. In the present calculation, the step of the reduced transverse energy $\Delta\varepsilon_\perp$ was taken as 0.01. The step of the depth Δz was taken from 100 A to 10 A, so that the relative change in $g(\varepsilon_\perp, z)$ is smaller than a few %. The distribution of particles with $\varepsilon_\perp \leqq 4.8\,\varepsilon_\perp^{c}$ was calculated at each depth successively. The number of particles flowing out through the boundary was estimated as less than 5 % after the particle travels for the largest penetration depth used in the present study and it was assumed that the number of particles inside the boundary was constant.

Figure 3.6 shows the distribution function at z = 1 μm in the <100> channel of KCl without defects (solid line) and with the displaced atoms of c = 1 %

for S = 7a (broken line). The initial distribution ($\Delta\psi = 0.09^{\circ}$) is also shown in the figure(dot-dash line). An arrow in the figure shows the value U(S) of the transverse potential at the position S. Similar result at z = 1μm with the displaced atoms of c = 1 % for S = 3a is shown in Fig. 3.7 (broken line). It is seen that a remarkable modification of the distribution function takes place around $\varepsilon_{\perp} = U(S)$. The value of the distribution at $\varepsilon_{\perp} = U(S)$ is depressed strongly: the effect being more remarkable when the displaced atoms are situated more close to the center of the channel. Clearly, the modification of the particle distribution at the low transverse energies is due to the contribution of defects to the diffusion coefficient $D(\varepsilon_{\perp})$ at low $\varepsilon_{\perp}$, where the accessible area $A(\varepsilon_{\perp})$ is rapidly increasing. Corresponding to the depression of the particle distribution at low transverse energies, the particle distribution increases at high transverse energies. This results in the increase of the random fraction or the dechanneling, which is just the interference effect between the scattering with defects and the scattering with electrons and the lattice vibrations. The interference effect may be more remarkable at larger penetration depth.

Figure 3.8 shows the particle distribution at z = 5μm in the <100> channel of KCl with the displaced atoms of 1 % for S = 7a (broken line) and without

defects (solid line). At large penetration, the strong modification is spread over wide range of the transverse energy; at the low transverse energies, the particle distribution is suppressed considerably and at high transverse energies the particle distribution increases remarkably. This modification makes a considerable contribution to the dechanneling.

These strong modification of the particle distribution in the transverse energy may affect appreciably the flux distribution or the spatial distribution of particles in a channel. It is interesting to note that the flux F_o at the center of the channel is modified by interstitials located near the center of the channel. The flux $F_o(z)$ was calculated by integrating $g(\varepsilon_\perp, z)/A(\varepsilon_\perp)$ from $\varepsilon_\perp = 0$ to ∞ (Eq. (2.6)). Figure 3.9 shows the dependence of $F_o - 1$, normalized by the value at $z = 0$, on the defect concentration q per area for the case of $S = 7a$. Here q is obtained by integrating the defect concentration $c(z)N$ from the surface to a depth z and given by cNz for c = constant. It is seen that the value of $F_o - 1$ reduces to about a half at $q \sim 10^{17}$ cm^{-2}. This effect would explain the results that the experimental heights of the flux peak in several crystals[19 - 22] are smaller than that theoretically predicted.[23]

The distribution function in the transverse energy may be measured through the angular distribution of transmitted beams from thin crystals. The experimental determination of the

transverse energy where the modification of the distribution by the displaced atoms occurs would provide a new technique of the interstitial atom location.

3.3.3 Random Fraction

The random fraction $\chi_R(z)$ was calculated as a function of z by integrating $g(\varepsilon_\perp, z)$ above $\varepsilon_\perp^c = 0.62$ (or $\psi_{1/2} = 0.335^\circ$). Figure 3.10 shows the dependence of the random fraction $\chi_R(z)$ on depth z for protons in the <100> string of KCl, in which 1 % atoms are displaced by various amounts of S. Below about 0.5 μm, there is little difference between $\chi_R(z)$ in a pure crystal and $\chi_R(z)$ in a crystal including displaced atoms: for shallow depth the change in the distribution function $g(\varepsilon_\perp, z)$ takes place only around $\varepsilon_\perp \sim U(S)$. Above 1 μm, however, $\chi_R(z)$ and its slope are affected considerably by the displaced atoms, and it should be noted that the slope of χ_R for S = 7a is twice the value near the surface. For z > 1 μm, the distribution function $g(\varepsilon_\perp, z)$ around $\varepsilon_\perp^c$ is perturbed appreciably due to the modification of $g(\varepsilon_\perp, z)$ by the displaced atoms as shown in Fig. 3.8, which enhances the dechanneling through the diffusion due to the scattering with electrons and the lattice vibrations. It is also to be noticed that the slope of $\chi_R(z)$ increases as the displacement of the atom increases. This result is easily understood since $D(\varepsilon_\perp)$ is non-zero over wider range of $\varepsilon_\perp$ as the displacement becomes larger.

Figure 3.11 shows the difference χ_d between the random fraction for crystals with defects (S = 7a) and that for crystals without defects obtained with the diffusion model and also with the single scattering, plural scattering and multiple scattering models, as a function of defect concentration q per unit area. The results of diffusion calculation with c = 0.01 and c = 0.05 are included. To calculate χ_d with the plural scattering model, the particle distribution proposed by Meyer[24] was used. From the figure it is seen that χ_d calculated with two different concentrations fall in nearly the same line if plotted as a function of q. The random fraction χ_d of the diffusion calculation increases slowly for small q and the slope becomes large abruptly at $q = 10^{16} \sim 10^{17}$ cm^{-2}, and finally converges to χ_d of the multiple scattering calculation. Although χ_d of the diffusion calculation is slightly larger than that of the single scattering calculation for $q < 10^{16}$ cm^{-2}, the value of χ_d in this region is too low and comparable with an error of the present calculation.

At high surface concentration of defects, the particle distribution modified by defects reaches a quasi-equilibrium as shown in Fig. 3.8. In such a case the dechanneling may be described as a gradual increases in the width of the distribution curve and the miltiple scattering model may be a resonable assumption. On the

other hand at low surface concentration of defects channeled particles are confined within the region of small transverse energy, and only collisions which impart transverse energies larger than $\varepsilon_\perp^c$ may cause dechanneling. Thus the single scattering model may be a good assumption at low concentration. As shown in Fig. 3.11, χ_d of the diffusion calculation agrees with the χ_d of the multiple scattering calculation at high surface concentration, and agrees with the χ_d of the single scattering calculation at low concentration. This result indicates that an appropriate choice has been made of the upper limit $\varepsilon_\perp^U$ of the integral (Eq.(3.6)), to obtain the diffusion coefficients described before.

The difference between χ_d calculated with the diffusion model and single and multiple scattering models for $q = 10^{16} \sim 10^{17}$ cm^{-2} may be ascribed to the defect-induced modification of particle distribution. Since this effect is not taken into account in the single and multiple scattering models, it is concluded that the effect of the modification of the particle distribution on dechanneling is intrinsic and that the single scattering model and the multiple scattering model underestimate χ_d for $q = 10^{16}$ cm^{-2} $\sim$ 10^{17} cm^{-2}, although they are good approximations for $q < 10^{16}$ cm^{-2} and $q > 10^{17}$ cm^{-2}, respectively. It is also clear that χ_d obtained with the plural scattering model is much smaller than those obtained with other models.

3.4 Conclusion

The particle distribution $g(\varepsilon_\perp, z)$ in the transverse energy $\varepsilon_\perp$ has been calculated as a function of the depth z for 1.5 MeV H^+ in the <100> channel of KCl crystals including lattice defects, using a diffusion equation. The diffusion equation involves the diffusion coefficient $D_d(\varepsilon_\perp)$ due to the scattering with defects (displaced atoms) as well as the diffusion coefficient $D_p(\varepsilon_\perp)$ due to the scattering with electrons and thermally vibrating lattice atoms. The diffusion coefficient $D_d(\varepsilon_\perp)$ caused by displaced atoms has been obtained with the present method for various distance S of the displacement from the atomic row. It has been shown that $D_d(\varepsilon_\perp)$ increases suddenly as $\varepsilon_\perp$ increases and is strongly peaked at a certain transverse energy, which is close to the value U(S) of the transverse potential at the position where the displaced atoms are located. As $\varepsilon_\perp$ increases further, $D_d(\varepsilon_\perp)$ increases gradually. At low transverse energies, the contribution $D_d(\varepsilon_\perp)$ of defects to the total diffusion coefficient $D(\varepsilon_\perp)$ is dominant while $D_p(\varepsilon_\perp)$ is dominant at higher transverse energies. The diffusion equation has been sloved numerically and the particle distribution $g(\varepsilon_\perp, z)$ has been obtained. It is found that displaced atoms (defects) depress $g(\varepsilon_\perp, z)$ around $\varepsilon_\perp \sim U(S)$ considerably and enhance the dechanneling through the interference effect between the scattering with defects and the scatter-

ing with electrons and thermally vibrating lattice atoms. This modification and the interference effect are more remarkable for a large displacement S, i.e., for the displaced atoms located close to the center of the channel.

The random fraction, i.e., the close encounter yield from lattice atoms χ_R has been also obtained as a function of the depth z. It has been shown that χ_R vs z curves depend on the displacement S and large displacement gives large χ_R. The increment of the random fraction χ_d induced by displaced atoms located close to the center of the channel is compared with χ_d of the single, multiple or plural scattering calculations. It has been found that χ_d obtained with the diffusion model is larger than χ_d of the single scattering calculation for the defect concentration per area $q \gtrsim 10^{16}$ cm^{-2} and finally converges to χ_d of the multiple scattering calculation. Since the single and multiple scattering models do not include the modification of the particle distribution or the interference effect, it is concluded that the single scattering model underestimates the dechanneling at high surface concentration of defects q and the multiple scattering model underestimates it at low q. The plural scattering model gives the much smaller value of χ_d than the other models give.

References

1. S. T. Picraux, "New Uses of Ion Accelerator," ed. by J. F. Ziegler (Plenum Press, New York, 1975) p. 229
2. J. A. Davies, J. Denhartog, L. Eriksson and J. W. Mayer, Can. J. Phys. 45, 4053 (1967).
3. E. Bøgh, Can. J. Phys, 46, 653 (1968).
4. J. W. Mayer, L. Eriksson, S. T. Picraux and J. A. Davies, Can. J. Phys. 46, 663 (1968).
5. L. C. Feldman and J. W. Rodgers, J. Appl. Phys. 41, 3776 (1970).
6. F. H. Eisen, B. Welch, J. E. Westmoreland and J. W. Mayer, "Atomic Collision Phenomena in Solids," ed. by D. W. Palmer, M. W. Thompson and P. D. Townsend (North-Holland, Amsterdam, 1970) p. 111.
7. J. E. Westmoreland, J. W. Mayer, F. H. Eisen and B. Welch, Rad. Effects 6, 161 (1970).
8. J. F. Ziegler, J. Appl. Phys. 43, 2973 (1972).
9. K. Schmid, Rad. Effects 17, 201 (1973).
10. K. L. Merkle, P. P. Pronko, D. S. Gemmell, R. C. Mikkelson and J. R. Wrobel, Phys. Rev. B8, 1002 (1973).
11. P. P. Pronko, J. Bøttiger, J. A. Davies and J. B. Mitchell, Rad. Effects 21, 25 (1974).
12. K. Morita, K. Tachibana and N. Itoh, Phys. Letters A33, 257 (1970).
13. K. Ozawa, F. Fujimoto, K. Komaki, M. Mannami and T. Sakurai, Phys. Stat. Sol. 9, 323 (1972).

14. J. Lindhard,
Mat. Phys. Medd. Dan. Vid. Selsk, 34, No. 14 (1965).

15. E. Bonderup, H. Esbensen, J. U. Andersen and
H. E. Schiøtt, Rad. Effects 12, 261 (1972).

16. V. V. Beloshitsky, M. A. Kumakhov and V. A. Muralev,
Rad. Effects 13, 9 (1972).

17. G. Molière, Z. Naturforsch, A2, 133 (1947).

18. J. H. Barrett, Phys. Rev. B3, 1527 (1971).

19. B. Domeij, G. Fladda and N. G. E. Johansson,
Rad. Effects 6, 155 (1970).

20. J. U. Andersen, O. Andreasen, J. A. Davies and E. Uggerhøj,
Rad. Effects 7, 25 (1971).

21. N. Iue, N. Matsunami, K. Morita, N. Itoh, M. Yoshida
and S. Hirota, Rad. Effects 14, 191 (1972).

22. J. U. Andersen, E. Laegsgaard and L. C. Feldman,
Rad. Effects 12, 219 (1972).

23. D. Van Vliet, Rad. Effects 10, 137 (1971).

24. L. Meyer, Phys. Stat. Sol. B44, 253 (1971).

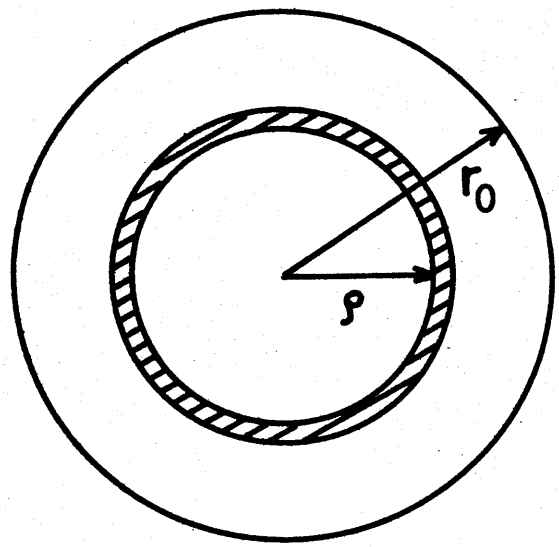

Fig. 3.1 A unit cell of a channel.

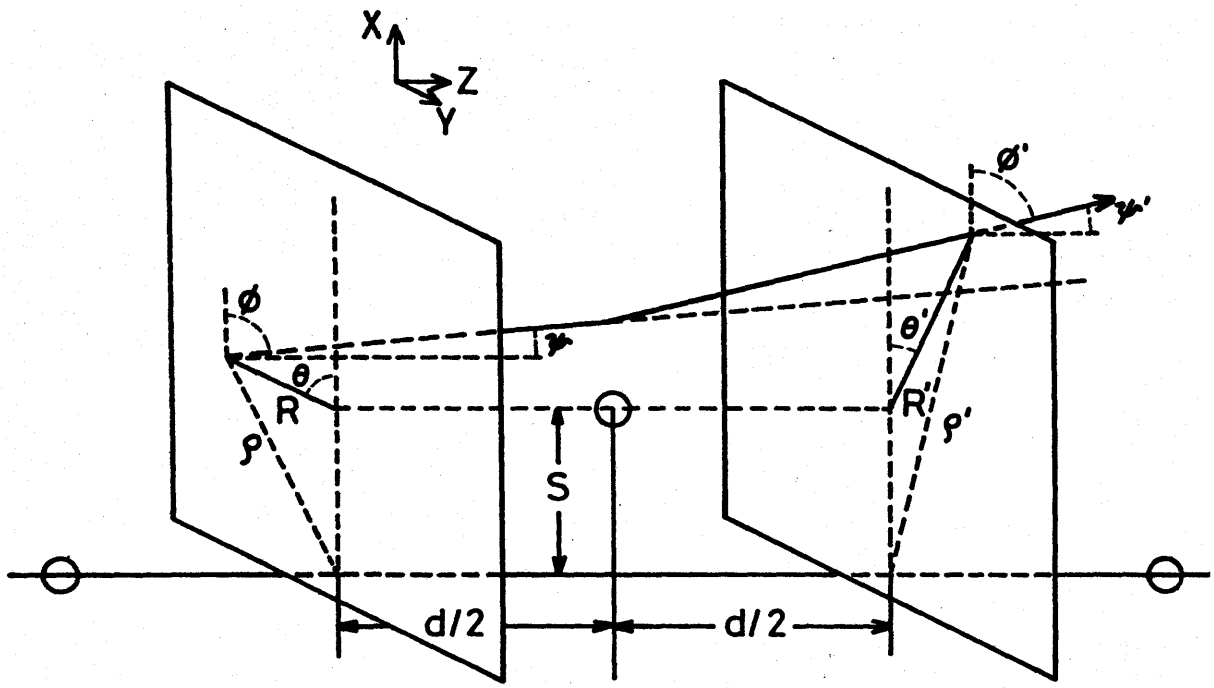

Fig. 3.2 Geometry for the calculation of the diffusion coefficient by defects.

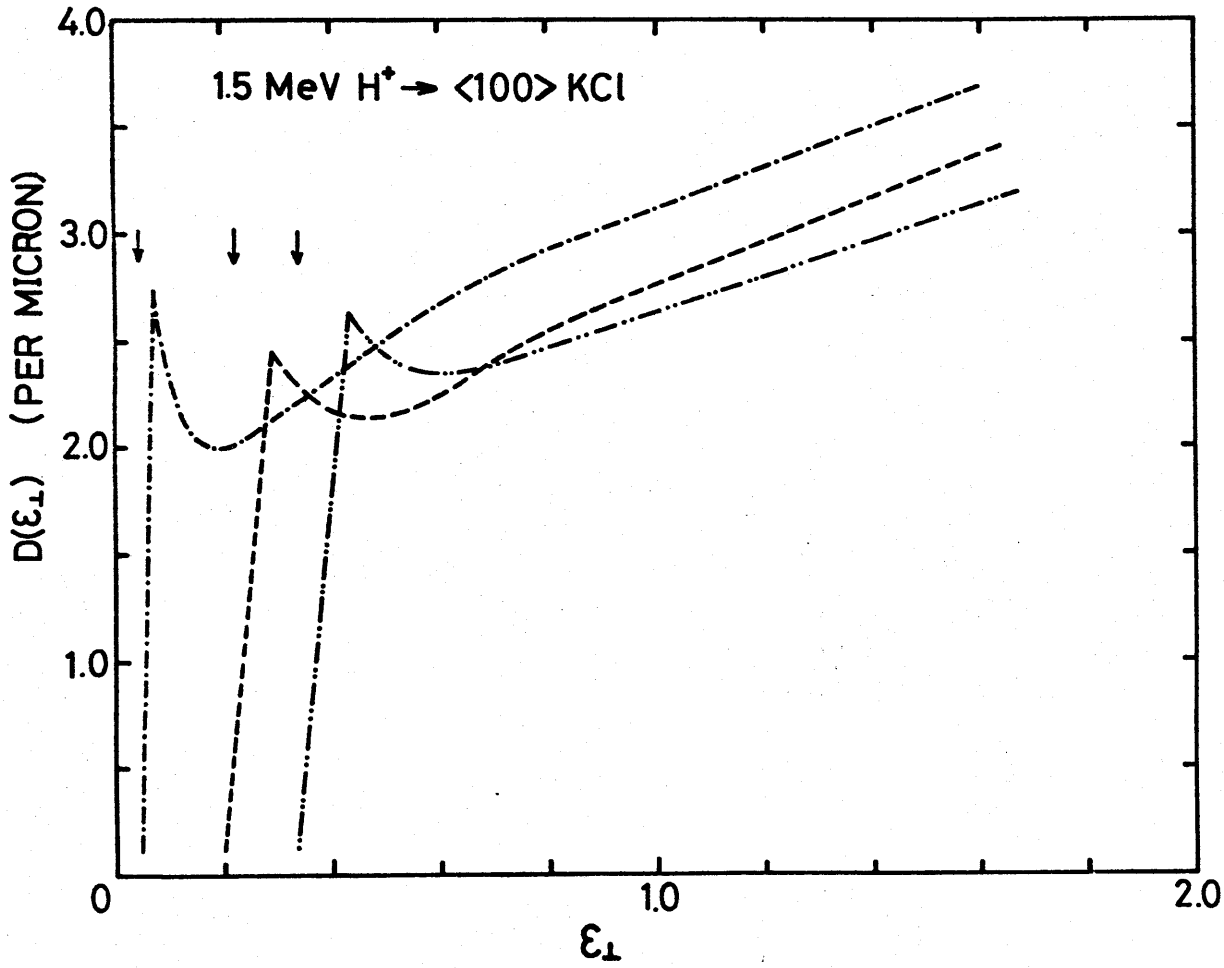

Fig. 3.3 Diffusion coeffcients of 1.5 MeV protons in the <100> channel of KCl at room temperature, caused by displaced atoms of unit fractional concentration, as a function of the reduced transverse energy $\varepsilon_\perp$, for S=3a (double dot-dash line), 4a (broken line) and 7a (dot-dash line). The arrows in the figure are the values U(S) of the transverse potential at positions S.

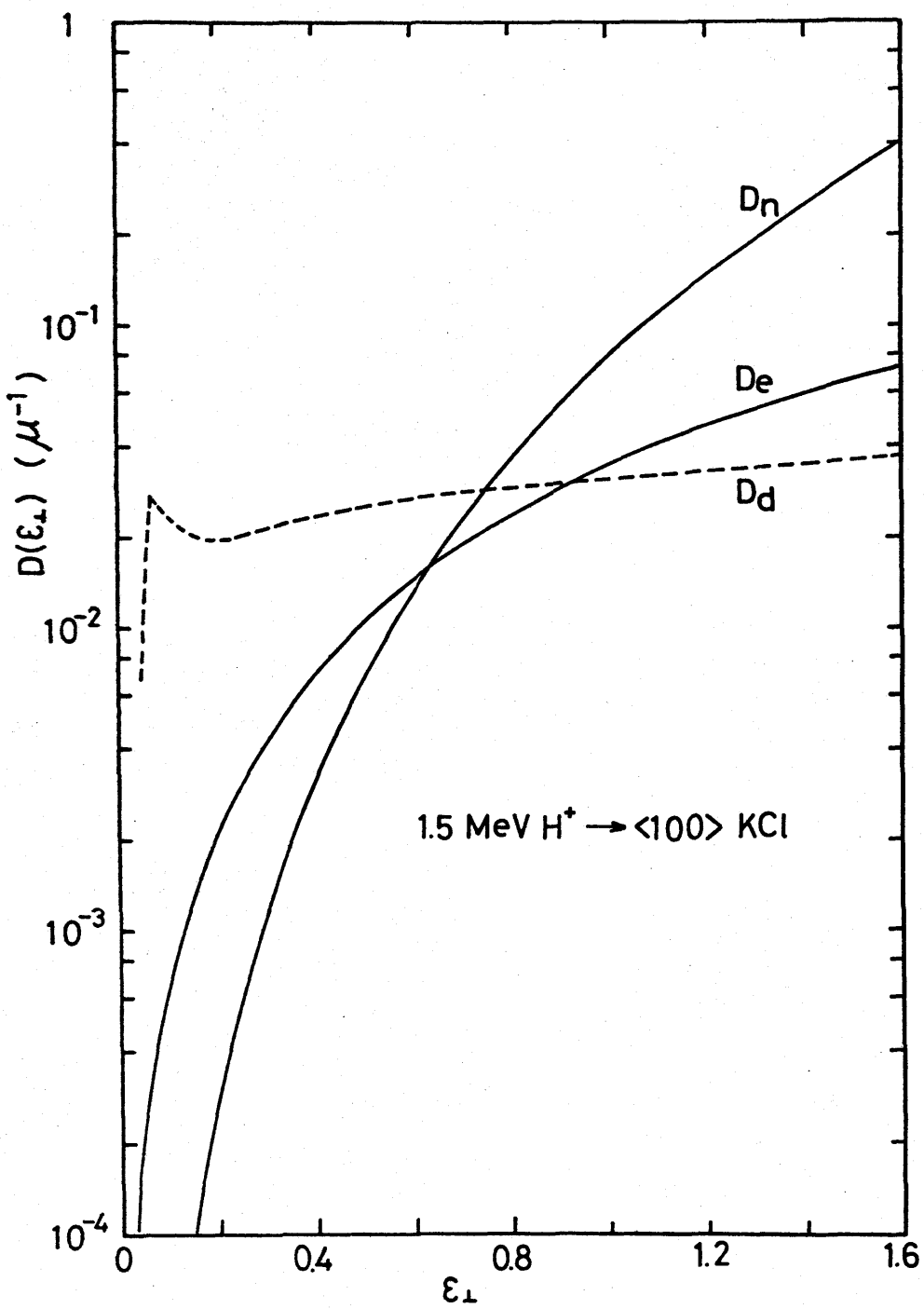

Fig. 3.4 Components of diffusion coefficient due to the scattering by thermally vibrating lattice atoms (D_n), by electrons (D_e) and by displaced atoms (D_d) with c=1%, S=7a, for 1.5 MeV protons incident along a <100> channel of KCl at room temperature.

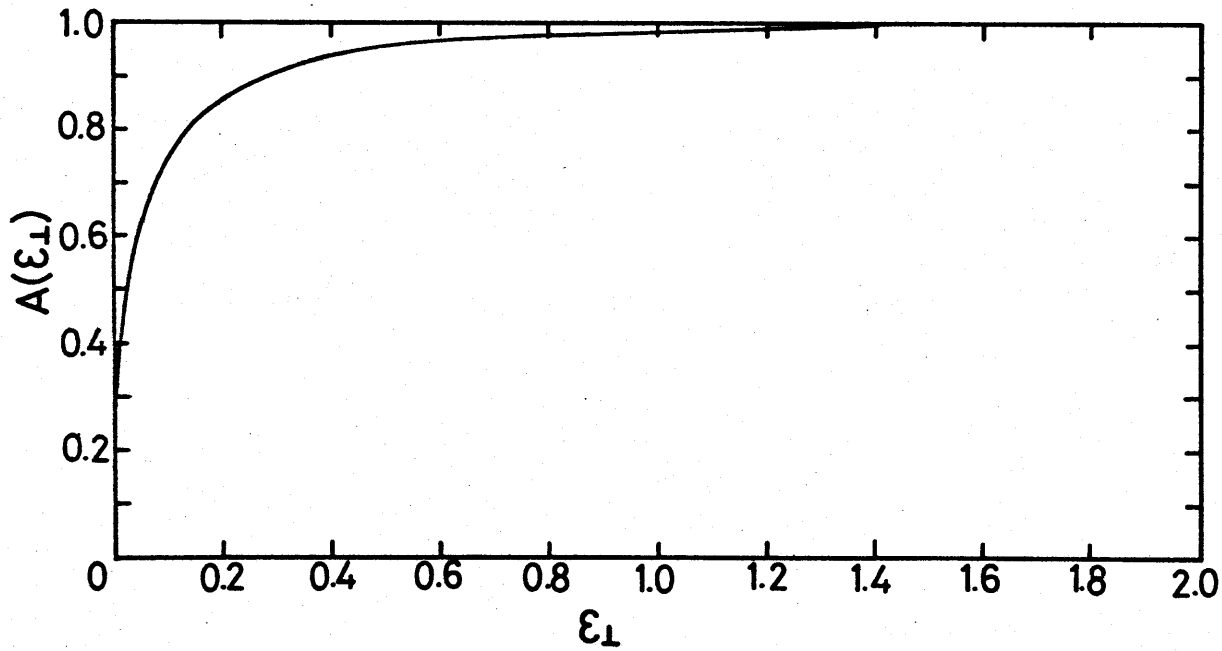

Fig. 3.5 Accessible area $A(\varepsilon_\perp)$ as a function of the reduced transverse energy $\varepsilon_\perp$, for 1.5 MeV H^+ in the <100> channel of KCl. The accessible area is normalized by the area of the unit cell.

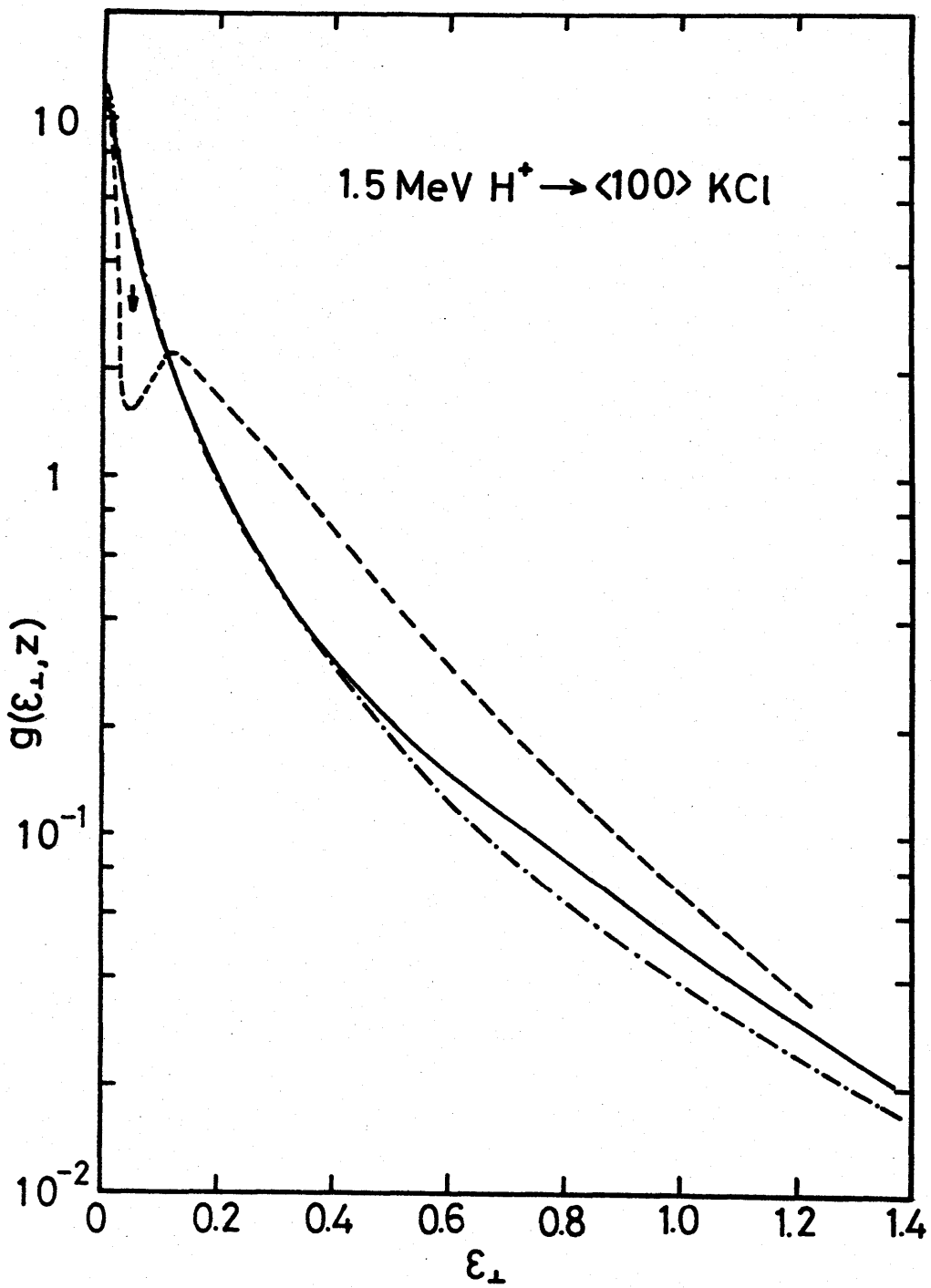

Fig. 3.6 Distribution of particles in the reduced transverse energy $\varepsilon_\perp$ at the depth z=1μm in a <100> channel of KCl without defect (solid line) and with defects of c=1% for S=7a (broken line). The initial distribution is shown by the dot-dash line.

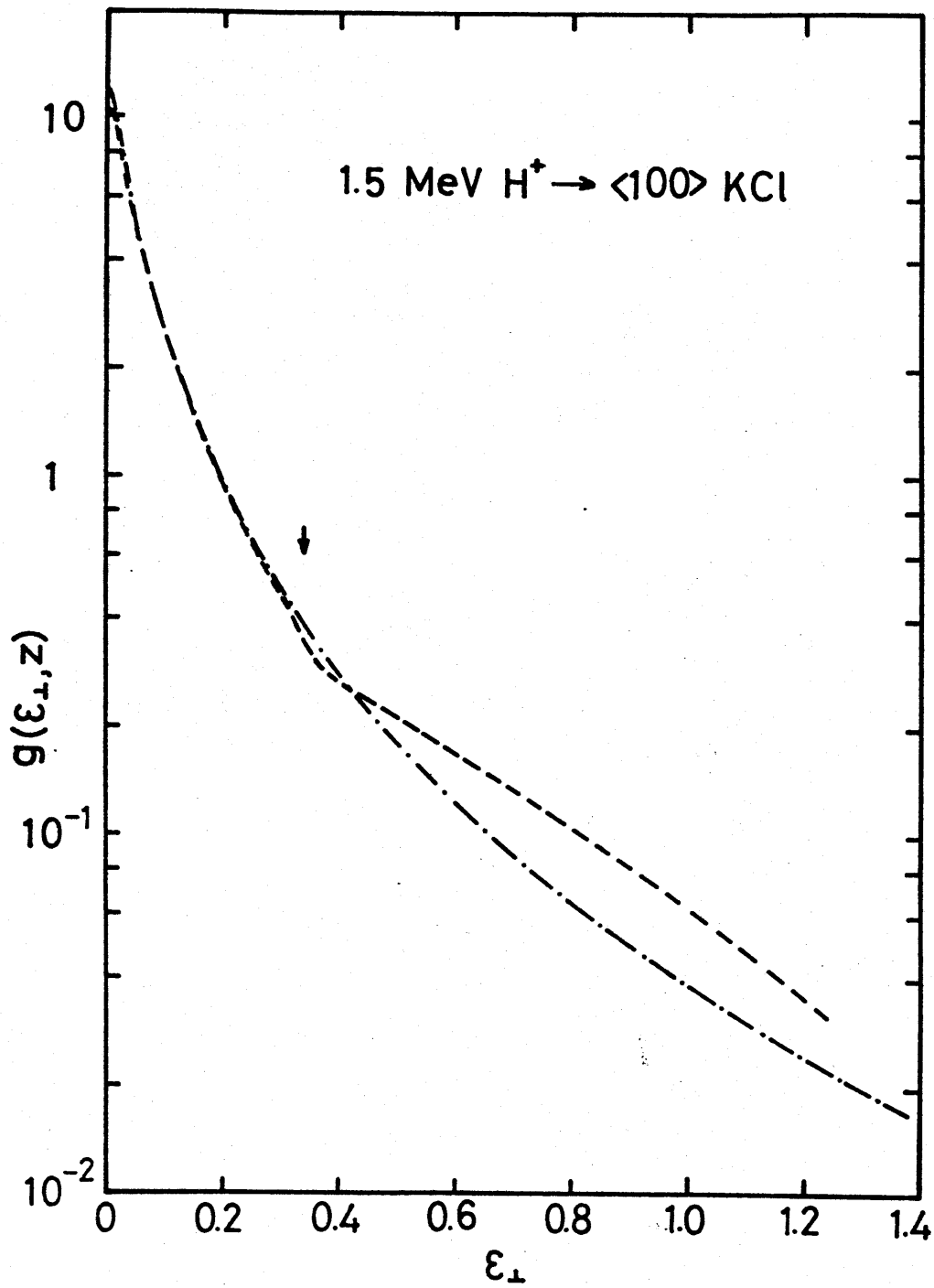

Fig. 3.7 Distribution of particles in the reduced transverse energy $\varepsilon_\perp$ at the depth z=1μm in a <100> channel of KCl with defects of c=1% whose displcement S=3a (broken line). The initial distribution is shown by the dot-dash line.

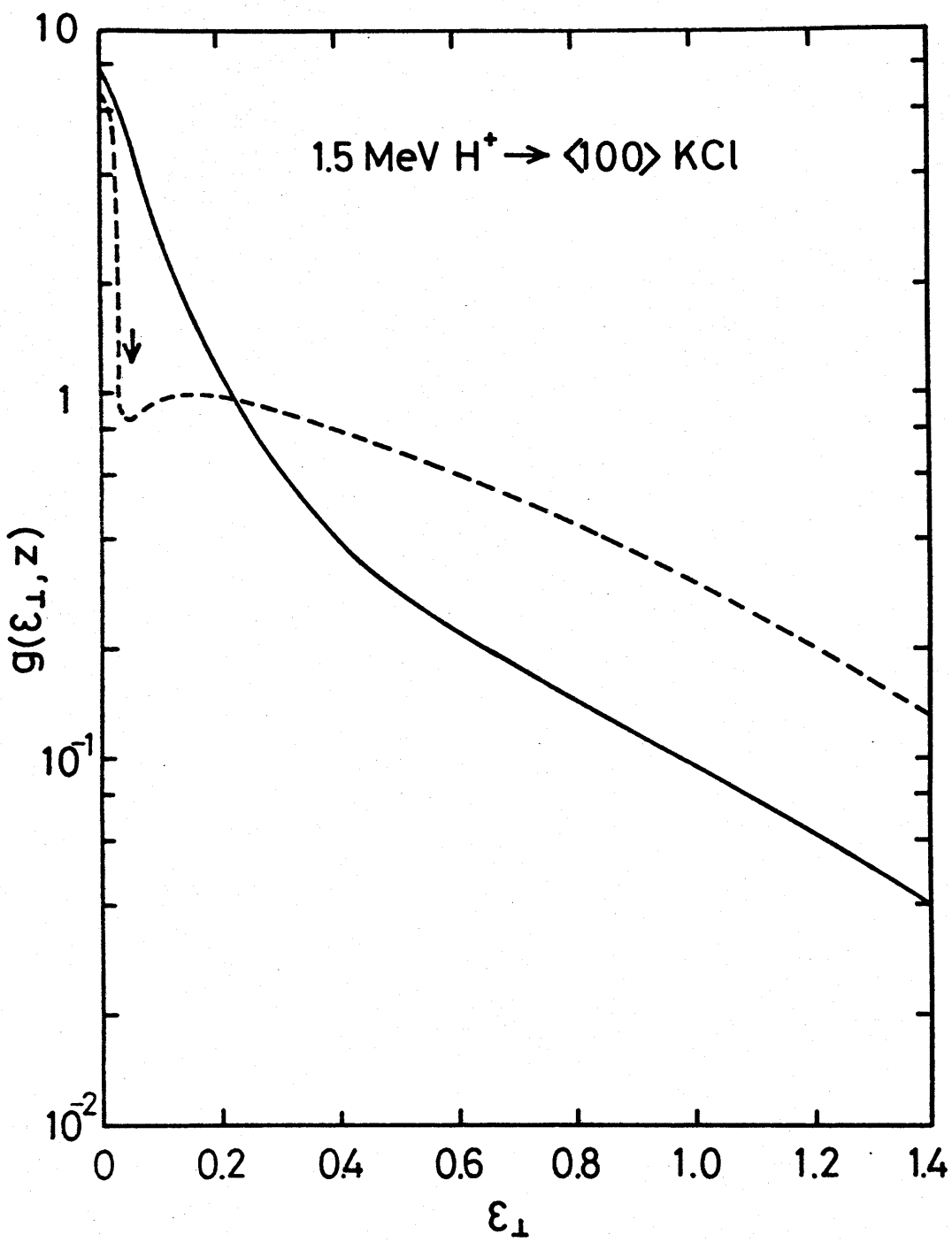

Fig. 3.8 Distribution of particles in the reduced transverse energy $\varepsilon_\perp$ at the depth z=5μm in a <100> channel of KCl with defects of c=1% whose displacement S=7a (broken line) and without defects (solid line).

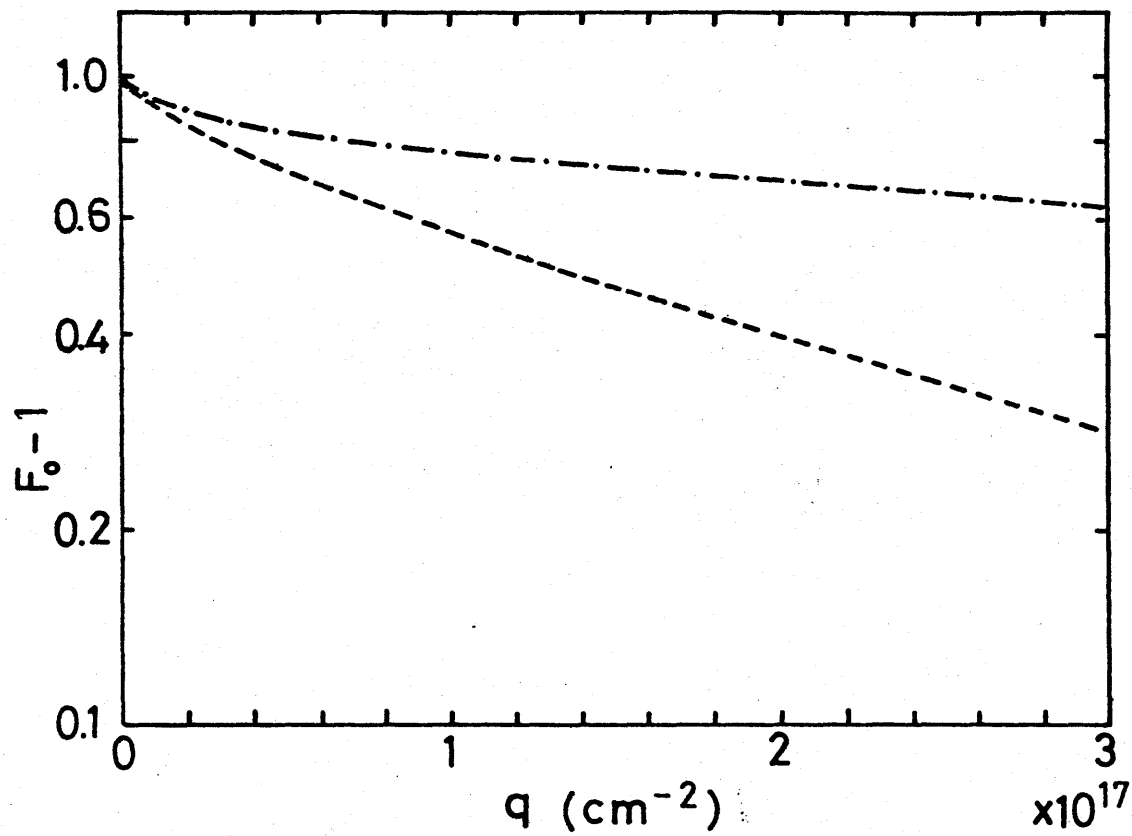

Fig. 3.9 Dependence of the normalized height of the flux peak F_o above the random value on the defect concentration per unit area, for the volume defect concentration c=1% (broken line) and for c=5% (dot-dash line).

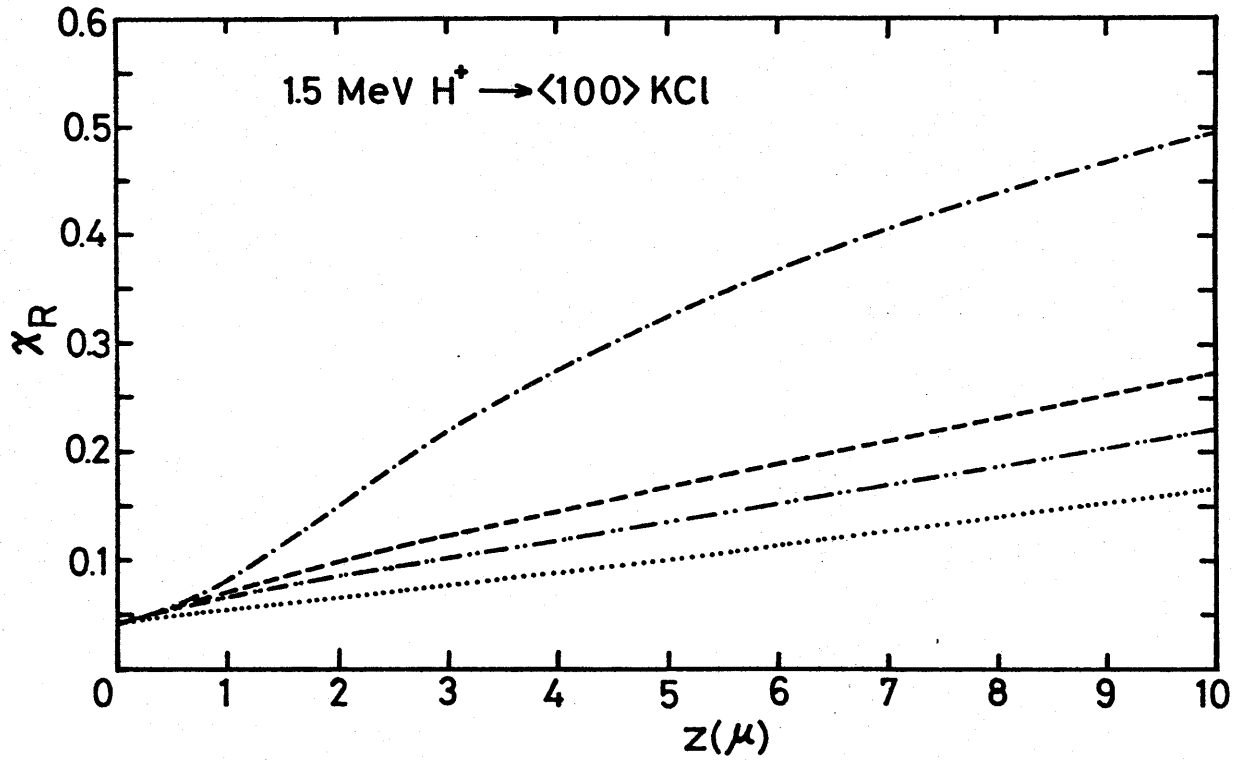

Fig. 3.10 Dependence of the random fraction χ_R for 1.5 MeV protons on the depth z in a <100> channel of KCl including displaced atoms of c=1%, for S=3a (double dot-dash line), 4a (broken line) and 7a (dot-dash line). The dotted line is the random fraction in the channel without displaced atoms.

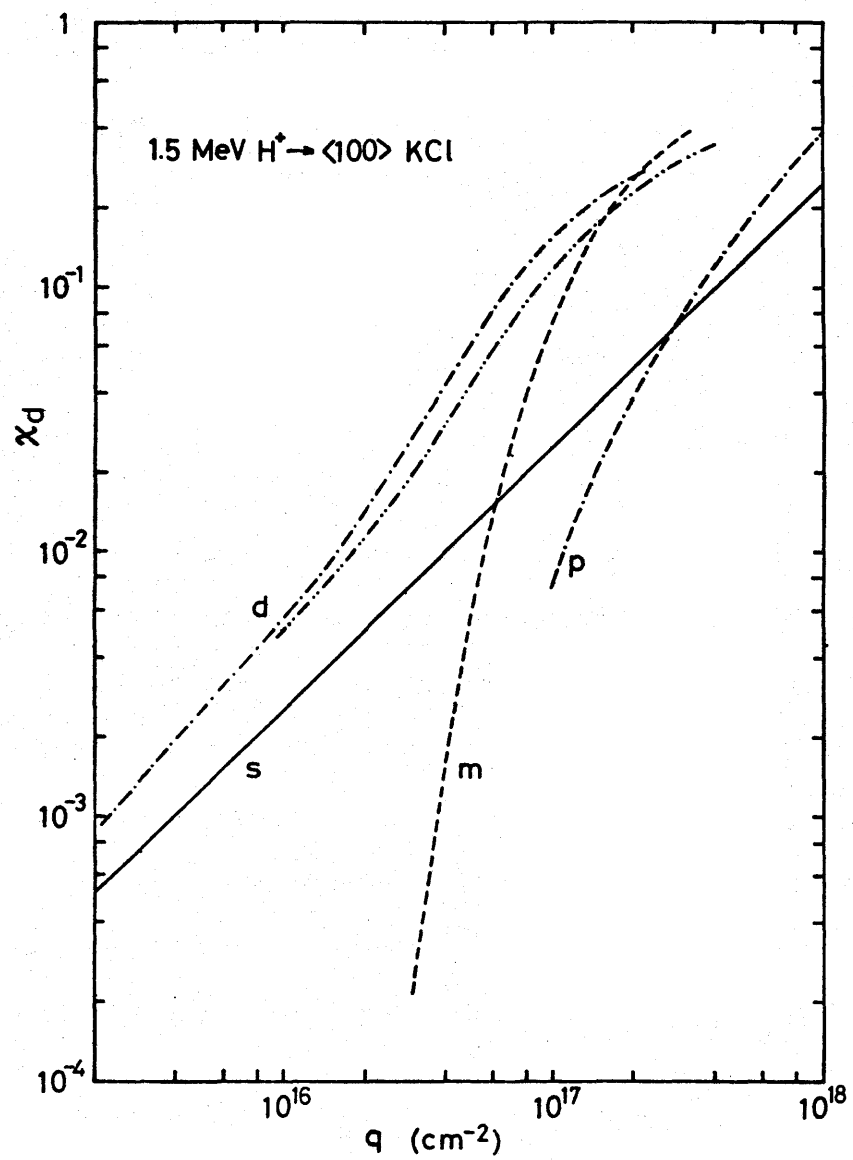

Fig. 3.11 Defect-induced increment in the random fraction, for 1.5 MeV protons incident along a <100> channel of KCl, calculated with the single scattering model (solid line), with the plural scattering model (double dash-dot line), with the multiple scattering model (broken line) and with the diffusion model with c=1% (dot-dash line), with c=5% (double dot-dash line) for S=7a.

CHAPTER IV

LOCATION OF Pb IMPURITY IN KCl AND Au IMPURITY IN Si

4.1 Introduction

In this chapter, channeling technique has been applied for the determination of the location of Pb impurity in KCl and diffusion-doped Au impurity in Si. KCl crystal is a typical ionic crystal and Si crystal is a semiconductor which has been extensively used for the electronic devices.

In alkali halides, optical and EPR studies have shown that the monovalent or divalent impurities stabilize the interstitial halogens created by irradiation and that the complexes of impurities and radiation-induced interstitials are formed.[1] Configuration of the complexes and their location in the lattice are closely related to their electronic state and its determination is important for general understanding of the interstitial stabilization by impurities. Although the environment of impurities or its electronic state is known to some extent through optical and EPR studies, the location of the impurities and the interstitial halogens in the lattice has not yet determined.

In Si crystals, some attentions have been paid to the Au impurities and it is suggested that they occupy either the substitutional or interstitial sites.[2,3]

Since the locations of implanted impurities in semiconductors are not very clear in most cases presumably due to the radiation damage introduced during implantation, it is of interest to study the location of diffusion-doped impurities in semiconductors, which would take well-determined locations. In Si doped with Au by diffusion, it has been found that a large amount of Au atoms is accumulated above the solubility limit near both front (Au-deposited) and back(non-deposited) surfaces. By means of channeling, Chou[4] has shown that Au atoms doped by diffusion into heavily p-doped Si crystal occupy the substitutional site near the surface. Yoshida et al.[5] found electron diffraction patterns of an unidentified poly-crystal at the Au-deposited surface in n-type 0.3 Ω Si. At the back surface, on the other hand, no other diffraction patterns than those of Si lattice are observed. This result suggests that Au atoms are located on either substitutional or interstitial sites near the back surface.

Firstly, this chapter describes the results of channeling and optical studies of Pb^{++}-doped KCl crystals. KCl crystal has an advantage of its nearly simple cubic structure which is suitable for the theoretical calculation. Furthermore divalent Pb impurity was selected partly because of larger mass than that of the host ions, which makes the usual Rutherford backscattering technique available in channeling experiments and partly

because of an interest of optical studies.[6] A model of the complex of the impurities and the radiation-induced interstitials is also suggested. Secondly, this chapter describes the results of channeling experiments of the accumulated Au atoms doped by diffusion at the back surface of Si crystals.

4.2 Experimental Procedure

4.2.1 Sample

Pure KCl crystals were obtained from the Harshaw Chemical Company. Pb^{++}-doped KCl crystals were made in our laboratory with the similar method described elsewhere.[7] The mixture of ultra pure KCl from the Merck Company and reagent grade $PbCl_2$ were heated slowly and fused in an evacuated two stage quartz tube. After they were melted in chlorine atmosphere, the quartz tube filled with Cl_2 gas was sealed off. Then Pb^{++}-doped KCl crystals were grown by the Bridgeman method in chlorine atmosphere from the molten mixture of KCl and $PbCl_2$. Pb^{++}-doped KCl crystals were annealed at 550° C for 30 minutes and then quenched to room temperature in order to avoid the aggregation of Pb^{++}. Before annealing, Pb^{++}-doped KCl crystals are not transparent probably due to the appearance of the colloid band.[8] After annealing above 500° C for 30 minutes, Pb^{++}-doped KCl crystals become transparent and the A band[6] appears in place of the colloid band. Pb^{++}-doped KCl crystals

were cleaved just before the channeling or optical measurements.

Au-doped Si were prepared with the method described elsewhere.[5] Gold was deposited by evaporation on one side of (111) surface of an n-type silicon grown by the floating-zone method. The specimen was preheated at 600° C for 20 minutes in a nitrogen atmosphere and gold was diffused into silicon at 1100° C for 90 minutes in an argon atmosphere. After gold was diffused into silicon, the gold left on the surface was removed by immersing the specimen in hydrofluoric acid for 5 minutes and then in hot acqua for 20 minutes.

4.2.2 Channeling

The experimental technique for channeling measurements is shown schematically in Fig. 4.1. The He^{+} beams of 1.5 MeV, which were obtained from the Van de Graaff accelator at Nagoya university and analyzed by a magnet, were collimated to an angular spread less than 0.09° by two copper apertures of 2 mm and 1mm in diameter, spaced at about 90 cm. The target crystals were mounted on a holder of copper disc or of polyvinyl chloride which was firmly held on a goniometer in a target chamber. The pressure of the target chamber was less than 10^{-5} torr. The goniometer assembly can be rotated about the vertical axis (tilt angle ψ) and about the horizontal axis (azimuthal angle φ). The accuracies of the tilt angle and the azimuthal angle

were 0.05° and 0.08°, respectively.

The helium ions backscattered through an angle of 150° or 165° were detected with a Si surface-barrier detector placed in the target chamber apart from the target crystal by 5 ~ 10 cm. The output of the detector was fed into a conventional electronic equipments, i.e., a charge-sensitive pre-amplifier, a main amplifier and a 100 (or 400)-channel pulse-height analyser (see Fig. 4.2), and the energy spectra of the scattered ions were obtained. The energy resolution (FWHM) of the present detection system was 30 KeV for 1.5 MeV He^{+}.

Crystal orientation relative to the beam direction was performed with the following method. To obtain an approximate alignment with a major crystal axis, the equipment as shown in Fig. 4.3 has been developed. In this case a proton beam was employed to reduce the radiation damage during the determination of the crystal orientation. The scattered protons from the target crystal with relatively high energies, that is, those which were backscattered near the crystal surface were selected by filtration through a mylerfilm and detected by converting to the photons by means of a fluorescent screen (ZnS). The photon beam was fed into a photomultiplier, the output of which was read with a d.c. ammeter. By this way, the intensity of the scattered ion beam can be read immediately as a function of the tilt and azimuthal angles. Crystal alignment can be

obtained, by minimizing the output of the d.c. ammeter. Further, the final alignment was made by comparing the backscattered spectra obtained with the multi-channel pulse-height analyser system at several tilt and azimuthal angles.

Backscattering spectra were obtained at various tilt angles in the proximity of a given axial direction. The azimuthal angle was chosen so that tilting did not lead to any planar channel. To compare the intensity of each spectrum it is necessary to know the integrated target current. In the case of Pb-doped KCl, the beam current was monitored with a removable Farady Cup every 100 ~ 200 sec during measurements. The fluctuation of the beam current was less than 5 %. The integrated target current for each spectrum was obtained by the time of the measurement multiplied by the average beam current. In the case of Au-doped Si, which was electrically isolated from the target chamber by the insulator target holder, the target current was integrated with an electrometer. Then the integrated beam current was obtained with the ratio of the target current and the current of the Faraday Cup. The typical beam current was 1 nA so as to minimize the pile-up effects and to get moderate counts of the particles backscattered by the impurities within ~ 10^3 sec.

4.2.3 Optical Absorption

Samples with thickness of about 1 mm were placed in a cryostat where optical absorption and irradiation with electrons or X-rays were made alternatively at liquid nitrogen or room temperature. Electrons at an energy of 1.5 MeV were generated with the Van de Graaff accelator described above. X-rays were generated with an X-ray tube operated at 50 KV, 30 mA. The optical absorption of crystals irradiated with electrons or X-ray was measured with a Shimazu MPS-50 photospectrometer.

4.3 Experimental Results

4.3.1 Channeling of KCl (Pb)

The backscattered spectra of He^{+} beams incident on Pb^{++}-doped KCl crystals were studied at room temperature. The energy spectra of 1.5 MeV He^{+} backscattered from Pb^{++}-doped KCl crystals are shown in Fig. 4.4. The aligned spectrum was obtained for the particles incident along the <100> axis of Pb^{++}-doped KCl and the random spectrum was obtained for the particles which were not incident parallel to any low index axis or plane. The particles scattered by potassium or chlorine has energies lower than 1.02 MeV and those with energies higher than 1.02 MeV can be distinguished as scattered by lead.

To compare the scattering yields from Pb and from

KCl, the energy window, over which the yields were summed, were set as shown in the figure. The energy window of Pb was set so as to make the statistical error nearly the same as the error from other sources. The energy window for KCl was taken so that helium ions scattered by KCl and Pb at the same depth were counted. The depth corresponding to this energy window was estimated to be 1500 A, using the stopping power for the random particle (~20 eV/A). It is to be noted that the Pb yields are independent of the position of the energy window owing to the flatness of the spectrum within a statistical error while the position of the energy window of KCl affect appreciably the KCl yield owing to the presence of the dechanneling effect. Therefore the window was set as close as to the surface, so as to minimize the dechanneling effect and eliminate the effect of the surface. In addition, the tail of the random spectrum for pure KCl at the position of the Pb window was measured in order to see how the pile-up effects influence the backscattering yield for impurities. The ratio of the counts in the Pb window to those in the KCl window for pure KCl was found to be less than 0.1 %, which was one-tenth of the ratio for the case of Pb^{++}-doped KCl. Thus in the following analysis the pile-up effects were disregarded. With the dependence of the scattering cross section on the square of the atomic number of the target atom, it is found that the concentration of lead

in this specimen is 0.05 atom % (1.5×10^{19} cm^{-3}).

Figure 4.5 shows the angular dependence of the yield of helium ions scattered by Pb (closed circle) and KCl (open circle) around the <100> and <110> axes. The backscattering yield was normalized by the yield for the random spectrum. Estimated errors of the Pb yields were also indicated in the figure. The counting time per point was about 40 minutes. The effect of radiation damage saturated within 10 minutes and the obtained yield was not affected by further irradiation. From the figure, the half-angle $\Psi_{1/2}$ for host ions of KCl was obtained as 0.48° and 0.35° when the particles were incident along the <100> and <110> axes, respectively. The minimum yield χ_{min} of KCl was also obtained as 0.29 and 0.31 for the <100> and <110> axes, respectively. The half-angles of host ions are rather close to the theoretical value of 0.52° and 0.44° for the <100> and <110>axes, respectively, calculated from Barrett's equation.(9) On the other hand, the minimum yields are much larger than the theoretical values, which are only a few per cent. As described later, this discrepancy is ascribed to the dechanneling due to the radiation damage. It should be noted that the angular variation of the Pb yields is much different from that of the KCl yields: for both the <100> and <110> axes, the angular dependence of the Pb yields shows a shallow dip with a small peak near the center. The peak for

the <110> axis is more narrow than that for the <100> axis. These patterns indicate that a substantial fraction of the Pb impurities is displaced to a position near the center of the <110> channel. Detailed comparison between the theoretical (broken line) and experimental angular variation is made in Sec. 4.4.1.

4.3.2 Optical Absorption of KCl(Pb)

It is known that the divalent lead impurity in KCl shows an optical absorption band at 273 nm, which called the A band.[10, 11] The concentration of Pb^{++} of the specimen used in the present study is much larger than that employed in the usual optical studies.[10, 11] In order to see whether Pb ions are in an aggregate form or not the oscillator strength of the A band was determined from the peak height and the concentration of Pb^{++} derived from the backscattering experiment, and compared with the result obtained previously.[10] Since the maximum optical density of the A band was larger than the detection limit of the photospectrometer, it was calculated by fitting the experimental optical-density vs photon-energy curve to a gaussian shape with the value of the peak position of 4.54 eV (273 nm) and the half width of 0.17 eV, determined from the absorption measurement of a specimen with low Pb^{++} concentration at room temperature. Then the oscillator strength of the A band was obtained as 0.16 ± 0.08 using the Smakula's

equation with the refractive index of 1.57 at 273 nm. Although the shape of the A band is not exactly gaussian, the error induced by this assumption is included in the error limit. The result agrees with the value of 0.11 obtained by Fukuda,[10] indicating that the lead ions are not in a form of aggregates but distributed randomly in crystals.

Effects of irradiation on the A band of Pb^{++} and the growth of the optical absorption bands due to the interstitial centers in Pb^{++}-doped KCl were studied through optical absorption measurements. For these studies, KCl crystals doped with Pb^{++} of relatively low concentration were used for observing the whole shape of the A band. Moreover, the change of the A band induced by He^{+} bombardment cannot be seen due to small penetration depth of MeV helium ions, which is at most 10 μm and much smaller than the thickness of the sample (~ 1 mm). Thus irradiation was made with 1.5 MeV electrons or 50 KeV X-rays, whose penetration depth is much larger than the thickness of the sample. While channeling studies were carried out at room temperature, optical absorption studies were performed at liquid nitrogen temperature as well as at room temperature, because the products of irradiation at liquid nitrogen temperature are well-defined as compared with those at room temperature.

Figure 4.6 shows the absorption spectra of Pb^{++}-doped KCl crystals measured at room temperature after

irradiation of 1.5 MeV electrons at the same temperature. The doses of electrons are 7×10^{14} cm^{-2} for curve (b) and curve (c), respectively. The absorption spectra of Pb^{++}-doped KCl before irradiation (curve (a)) and of pure KCl irradiated with X-rays (curve (d)) are also shown in the figure. X-ray dose for pure KCl was taken so as to produce nearly the same number of F centers as that for Pb^{++}-doped KCl (curve (c)). With the oscillator strength of the A band obtained by Fukuda,[10] Pb^{++} concentration of the specimen was calculated as 2×10^{17} cm^{-3}. For Pb^{++}-doped KCl, the broad band around 235 nm as well as the F band at 556 nm, i.e., an absorption due to electrons trapped at an anion vacancy (F center), appeared by electron irradiation. The broad band around 235 nm, which may originate from the interstitial halogens, is not exactly the same as the band produced in pure KCl. It can be seen that the intensity of the F band and the broad band around 235 nm increases with the increase of the electron dose. On the other hand the A band becomes broad as the electron dose increases. The concentration of the F center was estimated to be 3×10^{17} cm^{-3} for higher electron dose (curve (c)). Since the interstitials are the complementary defects of the F center, the concentration of the interstitials created by irradiation is nearly the same as that of Pb^{++}.

Similar results were obtained for the irradiation at liquid nitrogen temperature. The absorption spectra

of Pb^{++}-doped KCl measured at liquid nitrogen temperature after irradiation with 1.5 MeV electrons of 9×10^{14} cm^{-2} (curve (b)) and 2×10^{16} cm^{-2} (curve (c)) at the same temperature are shown in Fig. 4.7. Figure 4.7 also includes the absorption spectra of Pb^{++}-doped KCl before irradiation (curve (a)) and of pure KCl irradiated with X-rays (curve (d)). The broad band around 235 nm and the F band appeared by irradiation and the intensity of these two bands increases, while the A band decreases and becomes broad with the increase of the electron dose. The increase of the Pb^{+} band[12] at 254 nm and the V_k band, which has been ascribed to the self-trapped hole,[6] are also observed. In pure KCl, the absorption band at 240 nm is produced by heavy irradiation[13] and has been suggested to arise from the transition in the di-interstitial center[1] (V_4 center). In the present experiment, where the radiation dose is low, the peak position of the uv-band for pure KCl is not exactly the same as that of the V_4 band. Nevertheless the band around 235 nm produced in Pb^{++}-doped KCl is clearly different from that produced in pure KCl.

4.3.3 Channeling of Si(Au)

In the same way, the energy spectra of helium ions backscattered from Au-doped Si were measured at room temperature. Figure 4.8 shows the energy spectra from the back surface of Au-doped Si, when the beam of

1.5 MeV He^+ are incident along random (+), <100> (•), <110> (o) and <111> (x) directions. The energy spectra of helium ions backscattered by the impurity Au have peaks around 1.39 MeV (~ 71 channel) in contrast with Pb-doped KCl. Those peaks are due to that the concentration of Au decreases rapidly as the depth from the crystal surface increases. The maximum concentration of Au was estimated to be 5×10^{18} cm^{-3}.

The angular dependence of the Au impurity yield (•) and of the Si yield (o) around the <100> , <110> and <111> axes of the back surface is shown in Fig. 4.9. The Au impurity yield was obtained by integrating the scattering yield over the energy window as shown in Fig. 4.8 and the yields were normalized by the random yield. The width of the Au peak was mainly arised from the energy resolution and Au atoms are expected to be concentrated near the surface. Therefore the energy window for Si was set near the surface and its width was taken smaller than that for Au as shown in Fig. 4.8.

The minimum yield χ_{min} of Si was obtained as 0.073, 0.049 and 0.12 when the He^+ beam were incident along the <100> , <110> and <111> axes of the back surface, respectively. The half-angle $\Psi_{1/2}$ of Si was also obtained as 0.32^o, 0.55^o and 0.55^o for the <100> , <110> and <111> axes, respectively. The half-angles of host Si atoms agree well with the theoretical value of 0.50^o, 0.60^o and 0.54^o for the <100> , <110> and

<111> axes, respectively, calculated from the Barrett's equation.[9] The minimum yield χ_{min} are close to the theoretical value of 0.021, 0.015 and 0.018 for the <100> , <110> and <111> axes, respectively.

The Au yield shows quite different angular dependence from the Si yield, at the back surface as shown in Fig. 4.9. The Au yield has a shallow dip along the <100> direction. The minimum yield of this dip (0.75) is much larger than that of the Si dip (0.073), and the ratio of the half-width of the Au dip to that of Si dip is 0.56. The yield along the <110> direction is the superposition of a dip with a smaller half-width than that of the Si dip and a narrow peak. The half-width of this narrow peak is about 0.08^{o}. The Au yield along the <111> direction has a small peak and a dip with the same half-width as the Si dip. These results indicate that some fraction of the Au impurities occupy the mid-channel position in the <110> and <111> channels. The location of Au impurity is made in Sec. 4.4.2.

4.4 Discussion

4.4.1 KCl (pb)

For Pb^{++}-doped KCl, the A band ($^{1}\Gamma_{1}$ - $^{3}\Gamma_{4}$ transition) becomes broad with the increase of the electron dose at liquid nitrogen and room temperatures, suggesting that the Pb^{++} ions are placed in a symmetry worse than D_{4h} by irradiation. The broad band around 235 nm,

which is the characteristic band created in Pb^{++}-doped kCl, grows in accordance with the increase of the width of the A band. The width of the F band formed in Pb^{++}-doped KCl is the same as that in pure KCl. It is known also[14] that the migration of vacancies does not take place at liquid nitrogen temperature even during irradiation. Thus it follows that only the interstitial centers created in Pb^{++}-doped KCl is influenced by the presence of the Pb^{++} impurity. Since the broadening of the A band becomes significant as the interstitial concentration, which is equal to the F-center concentration, becomes nearly the same as that of Pb^{++}, it is concluded that the radiation-induced interstitials are stabilized by Pb^{++} ions forming the complexes of Pb^{++} ions and interstitial chlorines. The same conclusion has been drawn by Sonder et al.[15] from the observation of the enhancement of the F-center production yield by impurities. Furthermore, the broad band at around 235 nm of Pb^{++}-doped KCl irradiated at room temperature resembles that for the irradiation at liquid nitrogen temperature. Thus the complexes of Pb^{++} ions and interstitial chlorines created at room temperature may be identical to those produced at liquid nitrogen temperature. At liquid nitrogen temperature the Pb^{+} band and the V_k band are created by irradiation and a decrease in the area under the A band is observed. At room temperature, however, the electronic rearrangement does not take place and the

area under the A band is almost unchanged by irradiation.

By the above argument, it is clear that the radiation-induced interstitials are associated with Pb^{++} ions in Pb^{++}-doped KCl. Therefore the observation from the channeling experiments that the Pb^{++} are located off the lattice point is ascribed to their association with the interstitial halogens. In the following, the location of Pb^{++} in the KCl lattice is determined by a comparison of the experimental angular dependence of the impurity yields with a theoretical angular dependence of the impurity yields. The method of theoretical calculation based on the continuum approximation was described in Chapter II. In order to avoid the divergence of the flux distribution of the particles, the minimum accessible area was taken so that the channeled particles have an angular spread corresponding to a value at a depth of 1000 A, which was calculated from Lindhard's equation[16] of the multiple scattering of the particles by electrons. Moreover, the boundary transverse energy $\varepsilon_{\perp}^{B}$, explained in Chapter II, was taken as 2.0 in the reduced unit. This choice does not affect the angular dependence of the scattering yield for the atoms located inside the channel. For the impurities displaced along the <110> or <111> directions, there are different projected positions in the view along the <100> or <110> channel. This situation is shown schematically in Figs. 4.10 and 4.11, respectively. Under the consideration of the pro-

jected positions for <100> or <110> channel, the angular dependence of the close encounter yield was calculated, and the results for the <110> and <111> displacements are shown in Figs. 4.12 and 4.13, respectively.

For the Pb^{++} ions, the experimental angular dependence shows a peak with a shallow dip around both the <110> and <100> channels. The peak around the <110> channel is more narrow than the peak around the <100> channel. According to the calculated results, this is the case for the <110> displacement. Although the calculated angular dependence around the <100> channel has no dip, the experimental angular dependence of the Pb yields has a shallow dip. This is probably because some fraction of Pb^{++} ions remains in the normal lattice point. Furthermore the collision of the channeled particles with the lattice defects would modify the particle distribution and affect the angular dependence of the yield considerably as described in Chapter III: reducing the height of the flux peak and increasing the minimum yield.

In order to take the modification of the particle distribution into account for comparing the experimental yield with the theoretical, the following procedure was used. First it is assumed that the increase in the yield for the host ions is entirely due to the modification of the flux distribution. This assumption is valid because

the fractional concentration of defects in only 10^{-2}. Thus for the impurities on the normal lattice site, the angular dependence of the yield should be identical to that of the host ions. Since for impurities at the other positions, the effect of the flux modification on the angular dependence of the yield cannot be estimated accurately, the theoretical yield was used without any modification. Now considering that some fraction of Pb remains uninfluenced by interstitials and is situated at the lattice point, the theoretical curve in Fig. 4.5 was drawn so that it agrees with the experimental results for the dip portion. A best fit was obtained by assuming that 70 % of Pb ions are situated on the face center and 30 % on the lattice sites. The experimental angular dependence of the Pb yields agrees with the theoretical angular dependence within 10 % for the dip portion. On the other hand, the theoretical value of the peak around the center in the angular variation curve is larger by a factor of 2 ~ 3 than the experimental value. This discrepancy may be due to the dechanneling effect. According to the previous calculation for 1.5 MeV H^+ in <100> axis of KCl including lattice defects in Chapter III, the height of the flux peak is reduced to about o.4 of the initial value when the minimum yield reaches 30 %. Thus the difference in the experimental and theoretical peak height in Fig. 4.5 may be ascribed to the modification of the flux distribution. The discrepancy

may be also ascribed to that Pb^{++} is not located exactly at the face-center position. The calculation indicates that no-sharp peaks are observed if Pb^{++} is deviated from the face-center by o.4 A. Therefore, it is concluded that the Pb^{++} ions associated with the radiation induced-interstitials are situated near the face-center position within a deviation of 0.4 A.

Finally a probable model of the complex is discussed based on the results of the optical and channeling experiments. Pb^{++} ions are in the face-center position in a heavily irradiated specimens. Most extensive optical studies of the complex of a divalent impurity and interstitials have been made for Ca^{++}-doped KBr[17]. It has been shown that the D_3 center, which has a <100> symmetry axis and has a optical absorption band near the V_4 band, constitutes the complementary pair to the F center, and it has been suggested that the D_3 center is a divalent impurity associated with a di-interstitial[18, 19]. Since the heavy irradiation of Pb^{++}-doped KCl at room temperature produces an optical absorption band near the V_4 band without any reduction of Pb^{++} concentration, it appears that a center analogous to the D_3 center is produced in Pb^{++}-doped KCl. Thus it is reasonably assumed that the Pb^{++} ions are associated with the di-interstitial. White and Greene[20] has suggested that a di-interstitial has a form of a halogen molecule, of which each atom occupies approximately two neighboring body-

center sites. Furthermore Catlow et al.[21] have pointed out that the halogen molecule may be trapped by a pair of a positive and negative ion vacancies particulatly at higher temperatures. It is also known that before irradiation most of lead impurities are associated with a positive ion vacancy. In view of these arguments, a model of the complex of Pb^{++} and the di-interstitial is suggested as shown in Fig. 4.14. The two interstitial chlorines are situated at two positive alkali vacancies, one alkali vacancy having been occupied by the Pb^{++} and the other having been associated with the Pb^{++}. The Pb^{++} is located at a face center and the halogen atoms at positive ion sites combine with neighboring halogens to form the molecular ions.

For Mn^{++}-doped KCl and NaCl, it is known[22] that the substantial fraction of the intensity of the EPR signals for Mn^{++} disappear by irradiation. If the majority of Mn^{++} is associated with two Cl_2^- as shown in Fig. 4.14, no EPR signal would be observed, since the association with the paramagnetic centers may broaden the Mn^{++} EPR lines due to the dipole-dipole interaction. Although several radiation-induced centers involving Mn^{++} have been identified, all of them are produced only in small fractions. Therefore the present model is not contradictory to the observations on the radiation effect on Mn^{++}-doped NaCl. The positions of halogen interstitials were not determined directly in the pre-

sent work. The double alignment technique developed by Morita and Castanjen[23] would be useful to locate the halogen atoms in the complex.

4.2.2 Si (Au)

The results of Au-doped Si shown in Fig. 4.9 are analyzed assuming that the Au atoms occupy the interstitial sites. There are two possible interstitial sites in the Si lattice; the tetrahedral and hexagonal interstitial sites. If the Au atoms are located on the tetrahedral interstitial sites, which situate in the <100> and <110> strings of the host Si atom as seen from the vertical sections of the channels shown in Fig. 4.15, the Au yield should show dips with the same angular dependence as the Si yield along the <100> and <111> directions. The experimental results indicate that the Au atoms are not on the tetrahedral interstitial sites. On the other hand, if the Au atoms are located on the hexagonal interstitial sites, the Au yield would show the different angular dependence from the Si yield along the <100>, <110> and <111> directions. As seen from Fig. 4.9 the present experimental results are in favor of the hexagonal interstitial sites. Further quantitative discussions are made below.

According to the results of Chapter II, it is clear that Au atoms at the center A of the <110> channel induce the flux peaking. The peak observed in the

Au yield for the <110> channel is ascribed to the atom at the position A. At the position B of the <110> channel, the transverse potential was obtained as 11.5 eV by summing the six row potentials surrounding the <110> channel. Since this value is larger than the transverse energy $\delta \varepsilon_{\perp} \sim 4$ eV corresponding to the angular spread of the incident beam, the scattering yield of the atom at position B for the incident angle $\psi_{in} = 0$ is smaller than the random value, 1.0. Thus it is expected that the yield curve for the Au atoms at the position B show a dip with a smaller half width than that of the Si yield curve. Therefore the Au yield along the <110> direction is expected to be a summation of a dip and a flux-peaking, which is indeed observed as shown in Fig. 4.9 (b). In the case of the <100> direction the potential at the position C shown in Fig. 4.15 is 8.3 eV. Thus it is expected again that the Au yield along the <100> axis shows a dip with a smaller half-width than that of the Si yield, which is consistent with the experimental result shown in Fig. 4.9 (a).

For the <111> channel, a quarter of Au atoms lies on the string and three quarters occupy the position E shown in Fig. 4.15. The transverse potential at the position E is calculated as 1.5 eV and found to be smaller than $\delta \varepsilon_{\perp} \sim 4$ eV. Therefore the flux-peaking is expected to be observed in this case. The Au atoms at the position D produces a dip with the same half-width as the Si

Si yield. The experimental result shown in Fig. 4.9 (c) is also consistent with this consideration.

4.5 Conclusion

Channeling experiments and optical absorption studies have been made for Pb^{++}-doped KCl crystals. The comparison between the experimental yield of Pb and the theoretical yield of Pb calculated with the continuum approximation has shown that the substantial fraction of Pb^{++} ions is located at the face-center position for irradiated Pb^{++}-doped KCl crystals. The optical absorption srudies have shown that the A band due to Pb^{++} becomes broad and the V-type center, which is different from the V_4 center produced in pure KCl crystals, grows as the irradiation dose increases. It is concluded that the displacement of Pb^{++} ions from the lattice point to the face-center position is due to the association with the radiation-induced interstitials. A model of the complex of the Pb^{++} impurities and the radiation-induced interstitials is suggested.

Channeling experimants have been also made to locate diffusion-doped Au in Si crystals, in which Au is evapolated on a surface and diffused into the crystals. At the back surface of the specimen, where Au is accumulated at a concentration of 5×10^{18} cm^{-3}, it is found that Au in Si is situated at the hexagonal interstitial position.

References

1. N. Itoh, Crst. Lattice Defects 3, 115 (1972).
2. W. C. Dash, J. Appl. Phys. 31, 2275 (1960).
3. M. Yoshida and K. Saito, Japan. J. Appl. Phys. 9, 1217 (1970).
4. S. Chou, "Investigation of Diffused Impurities in Silicon Using the Ion Backscattering Technique," Standford Univ., (1971).
5. M. Yoshida and S. Hirota, Japan. J. Appl. Phys. 11, 917 (197
6. W. B. Fowler, "The Physics of Color Center," ed. by W. B. Fowler (Academic Press, New York, 1968) p. 53
7. M. Ikeya, N. Itoh and T. Suita, Japan. J. Appl. Phys. 7, 837 (1968).
8. S. C. Jain, S. Radhakrishna and K. S. K. Sai, J. Phys. Soc. Japan 27, 1179 (1969).
9. J. H. Barrett, Phys. Rev. B3, 1527 (1971).
10. A. Fukuda, Sci. Light (Tokyo) 13, 64 (1964).
11. S. G. Zazubovich, N. E. Lushchik and Ch. B. Lushchik, Opt. Spectry (USSR) 15, 203 (1964).
12. S. B. S. Sastry, V. Viswanathan and C. Ramassastry, J. Phys. Soc. Japan 35, 508 (1973).
13. B. J. Faraday and W. D. Compton, Phys. Rev. 138, A893 (1965).
14. E. Sonder and W. A. Sibley, "Point Defects in Solids vol. 1," ed. by J. H. Crawford, Jr. and L. M. Slifkin (Plenum Press, New York, 1972) p. 201

15. E. Sonder, G. Bassignani and P. Camagni,
Phys. Rev. 180, 882 (1969).

16. J. Lindhard,
Mat. Fys. Medd. Dan. Vid. Selsk. 34, No. 14 (1965).

17. T. Ishii and J. Rolfe, Phys. Rev. 141, 758 (1966).

18. J. Hoshi, M. Saidoh and N. Itoh,
Cryst. Lattice Defects (in print).

19. N. Itoh and M. Ikeya, J. Phys. Soc. Japan 22, 1170 (1967).

20. W. W. White and A. C. Greene,
Cryst. Lattice Defects 1, 83 (1969).

21. C. R. A. Catlow, K. M. Diller and M. J. Norgett,
J. Phys. C8, L34 (1975).

22. N. Itoh and M. Ikeya, Rad. Effects 4, 161 (1970).

23. K. Morita and H. D. Carstanjen, "Atomic Collisions in Solids," ed. by S. Datz, B. R. Appleton and C. D. Moak, (Plenum Press, New York, 1975) p. 825.

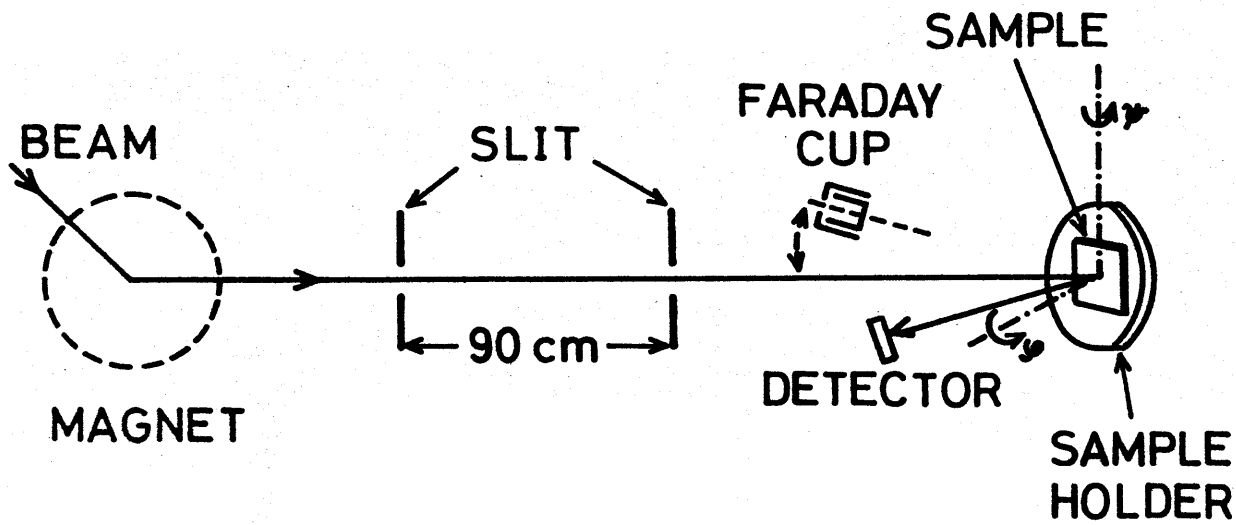

Fig. 4.1 Schematic arrangement of channeling experiments.

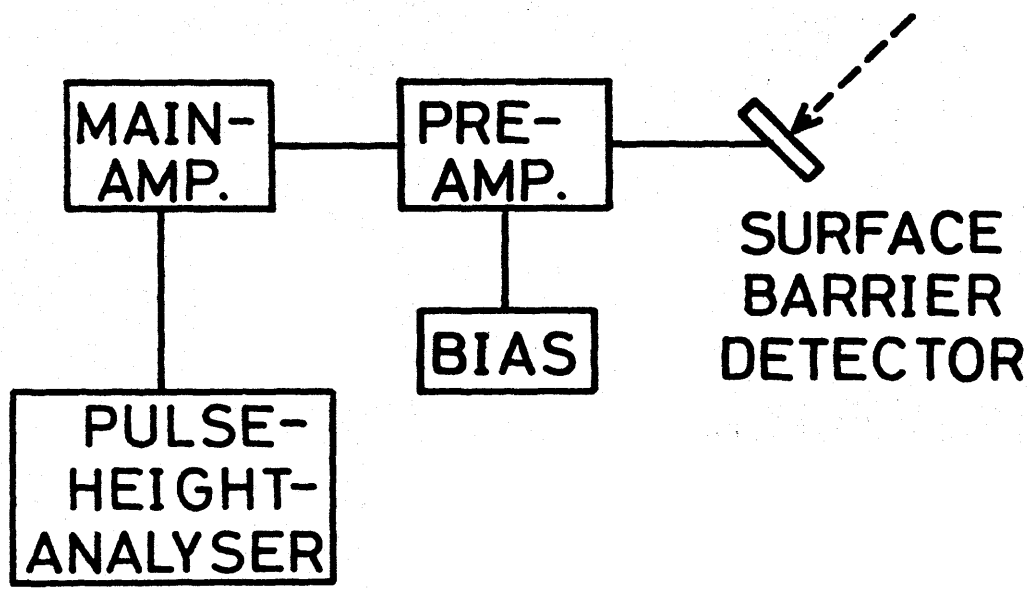

Fig. 4.2 Block diagram of detector and associated electronics.

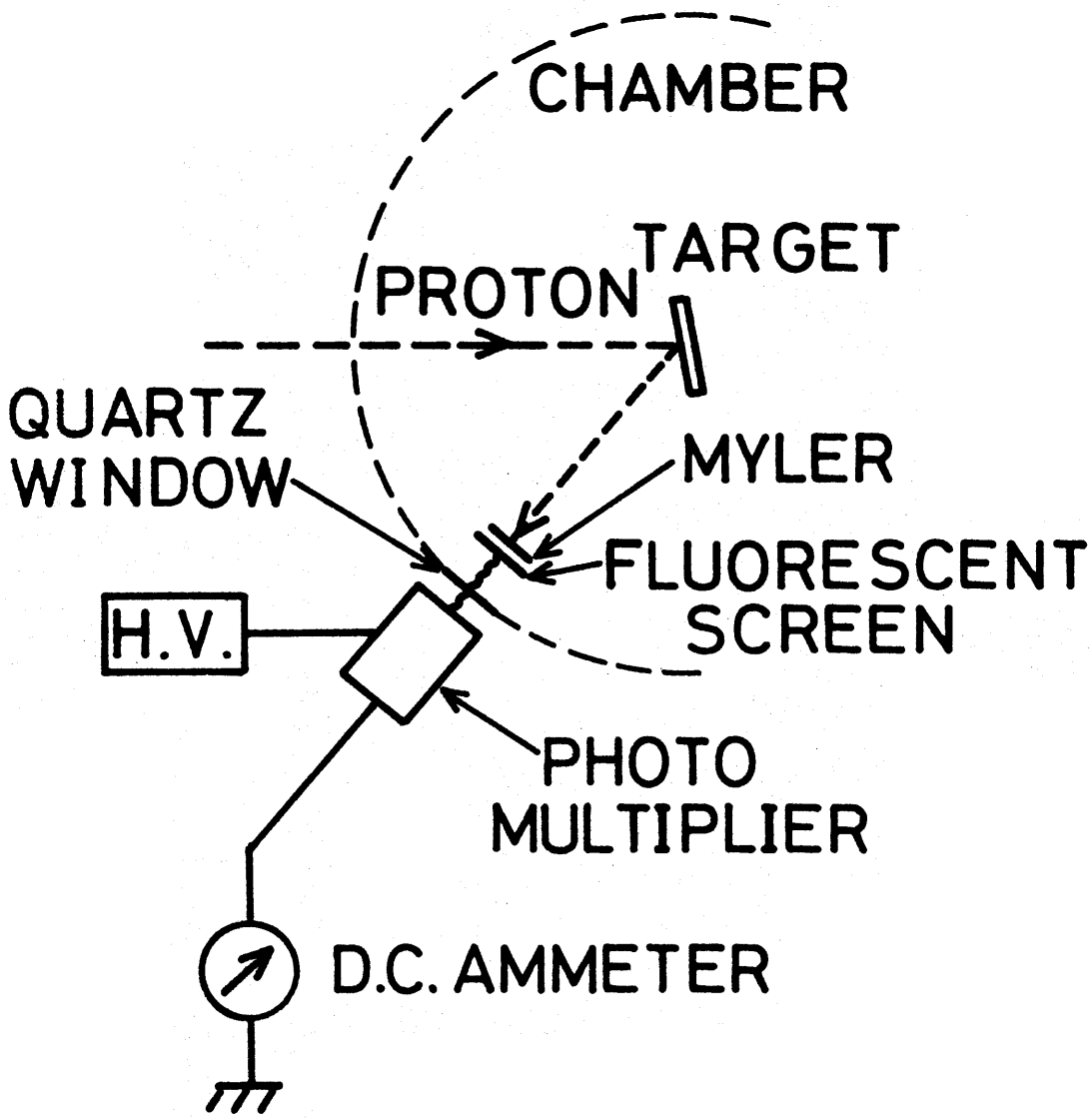

Fig. 4.3 Schematics of a equipment for crystal alignment.

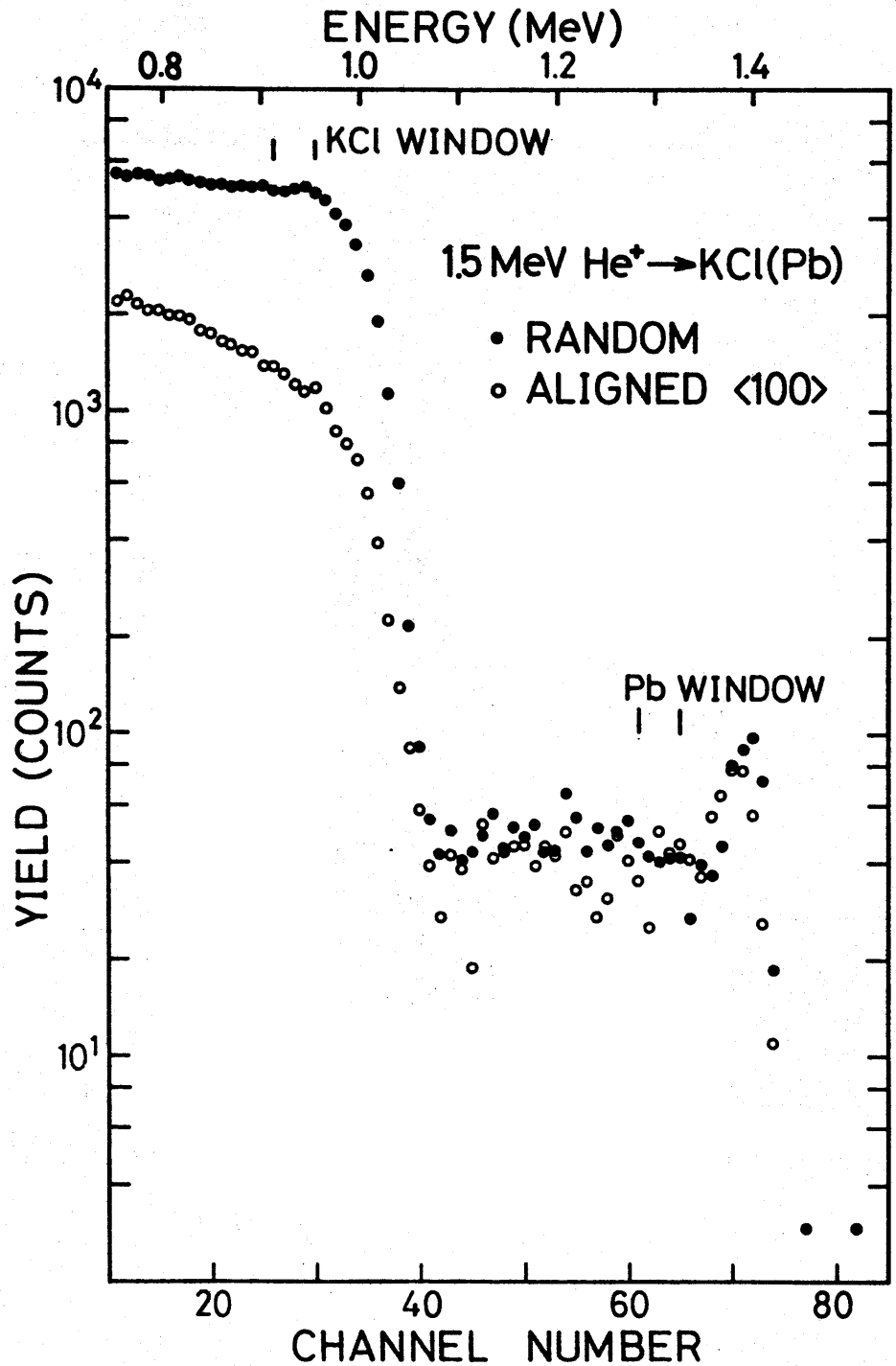

Fig. 4.4 Backscattered energy spectra for 1.5 MeV He^{+} incident along the <100> and random directions in a Pb^{++}-doped KCl crystal at room temperature.

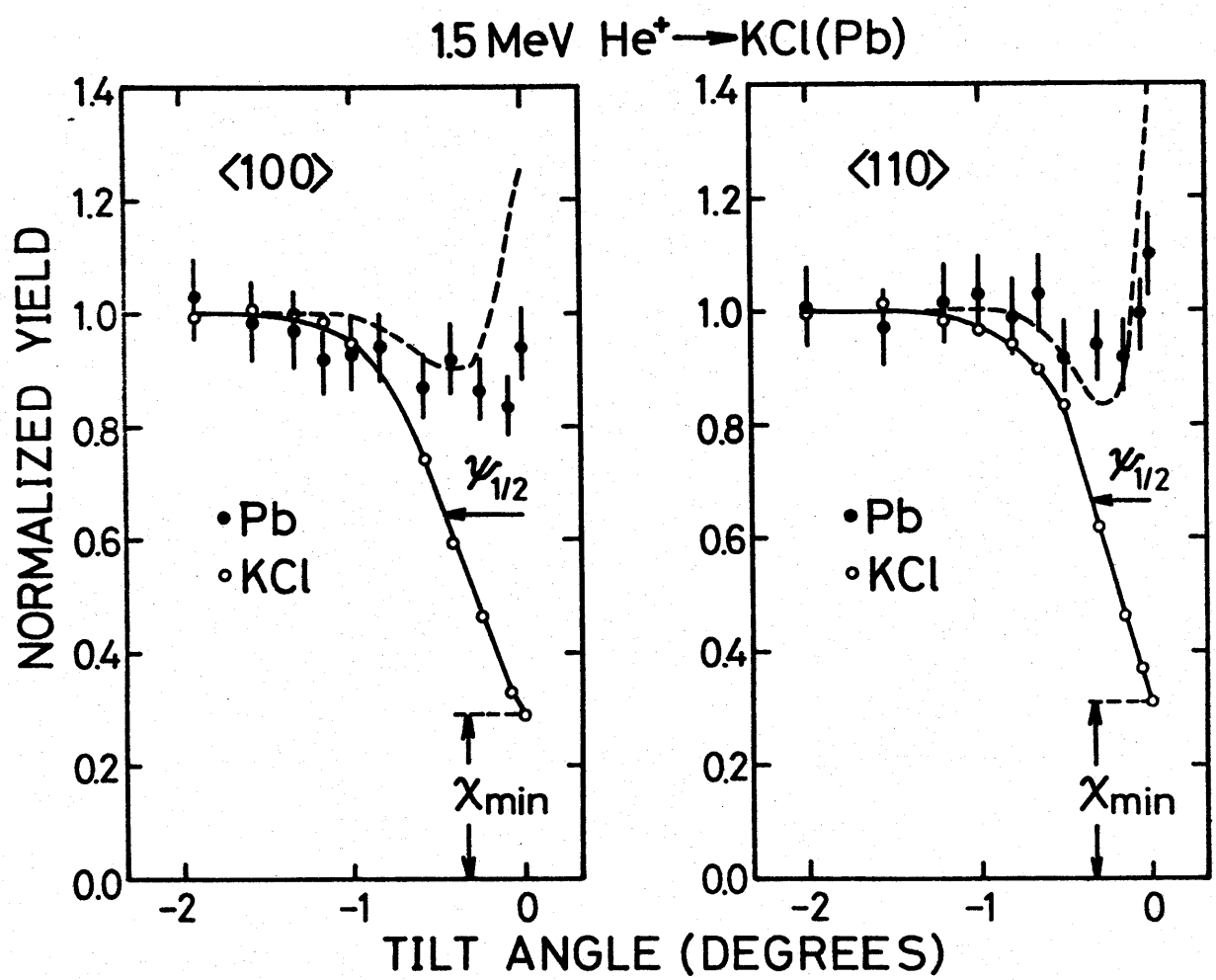

Fig. 4.5 Normalized backscattering yield from Pb(closed circle) and KCl(open circle) as a function of the angle between the direction of the incident beam and the <100> , <110> axes. The solid line is drawn by inspection. The broken line is the theoretical backscattering yield from Pb.

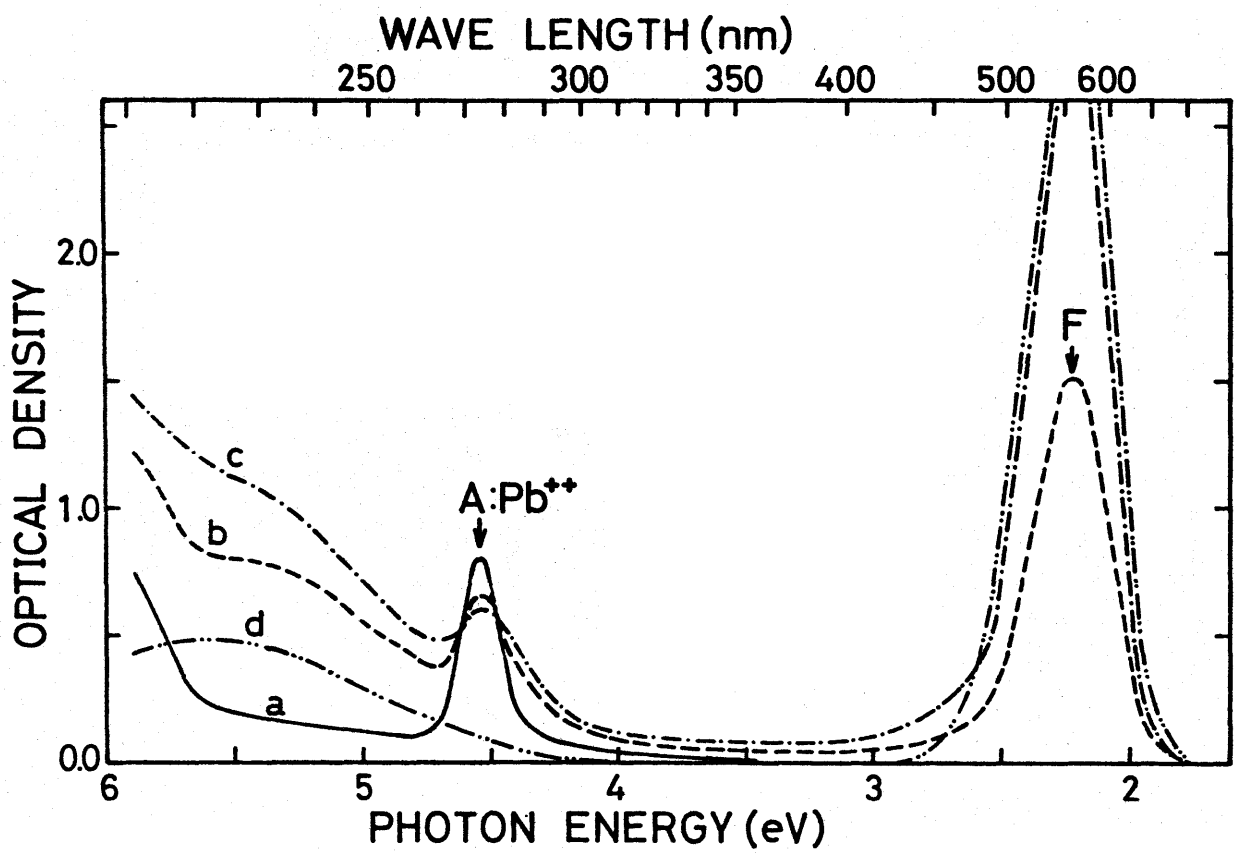

Fig. 4.6 Optical absorption spectra of a Pb^{++}-doped KCl measured at room temperature after irradiation with 1.5 MeV electrons of 7×10^{14} cm^{-2} (b) and 1.5×10^{16} cm^{-2} (c) at the same temperature. Optical absorption spectra of a Pb^{++}-doped KCl before irradiation (a) and of a pure KCl irradiated with X-rays (d) are included.

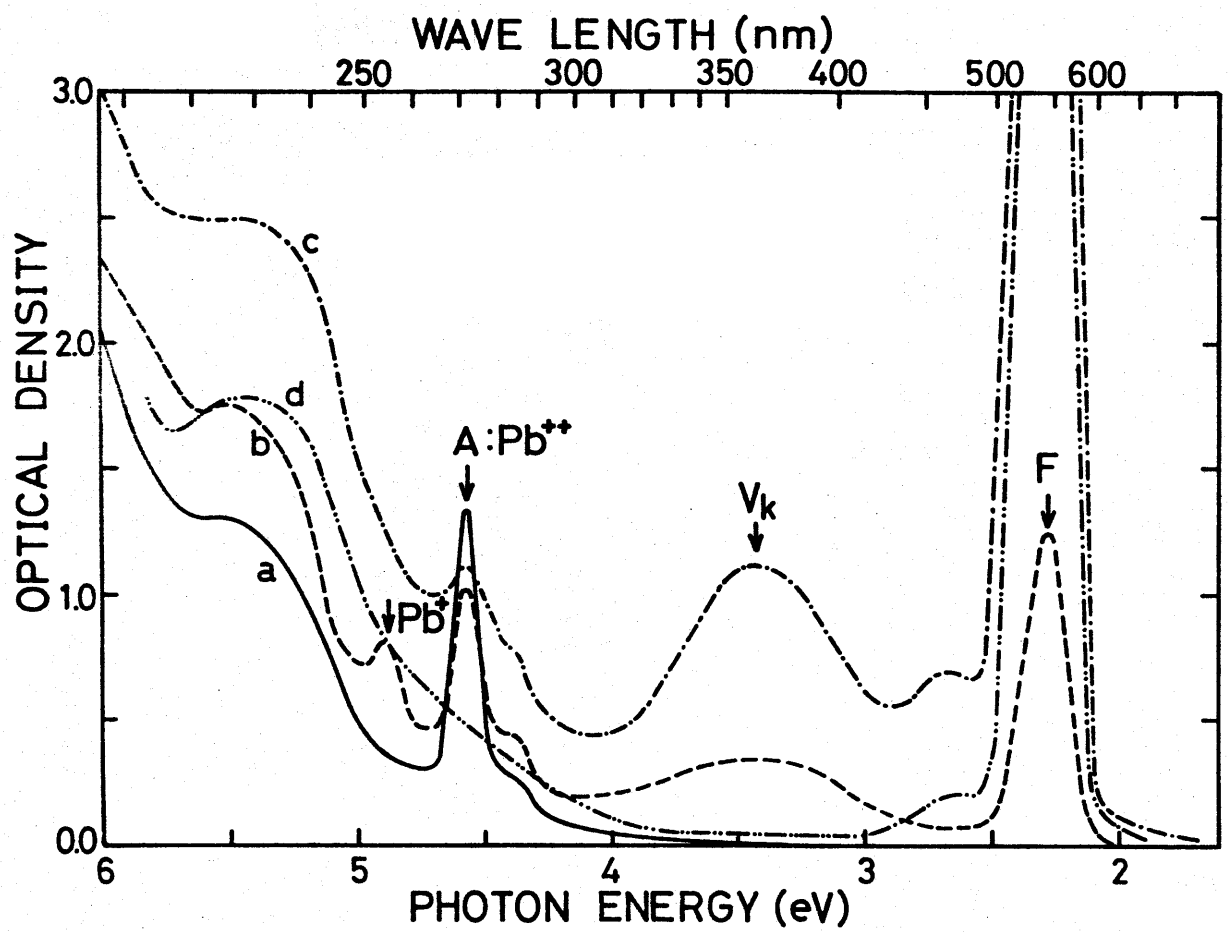

Fig. 4.7 Optical absorption spectra of a Pb^{++}-doped KCl measured at liquid nitrogen temperature after irradiation with 1.5 MeV electrons of 9×10^{14} cm^{-2} (b) and 2×10^{16} cm^{-2} (c) at the same temperature. Optical absorption spectra of a Pb^{++}-doped KCl before irradiation (a) and of a pure KCl irradiated with X-rays (d) are included.

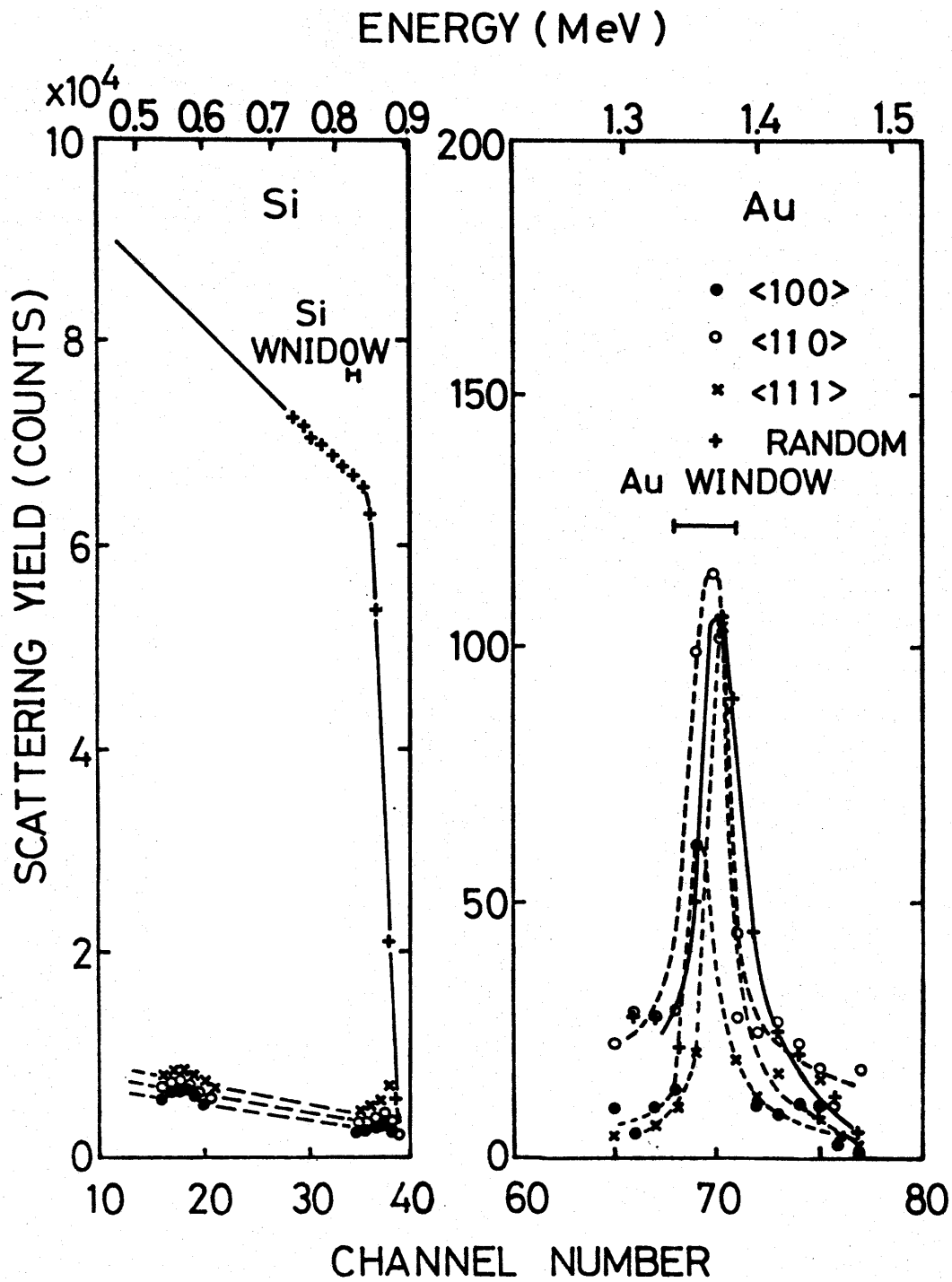

Fig. 4.8 Energy spectra of helium ions backscattered from the back surface of Au-doped Si when the beam of 1.5 MeV He^+ is incident along the <100> (•), <110> (o), <111> (x) and random (+) directions at room temperature. The solid and broken lines are drawn by inspection.

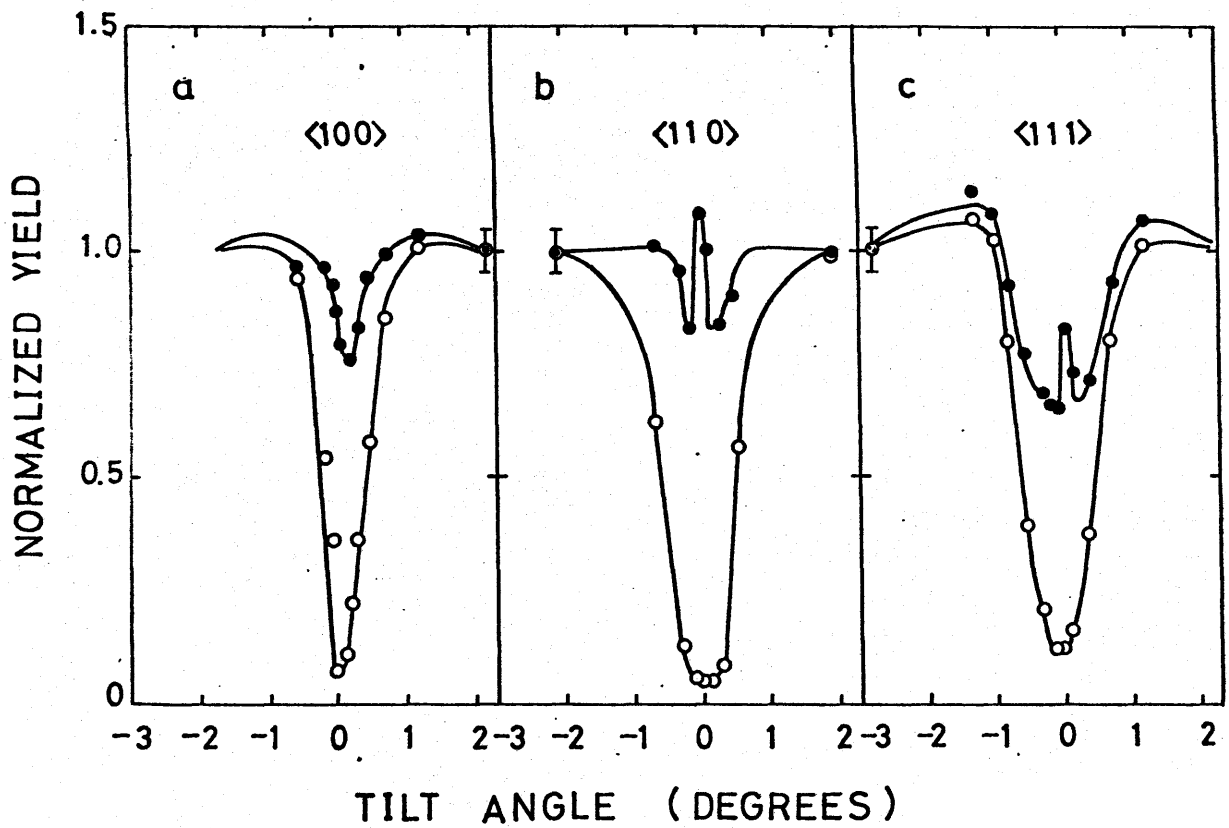

Fig. 4.9 Normalized yield of 1.5 MeV helium ions backscattered from the Au atoms (•) and Si atoms (o) at the back surface of Au-diffused Si crystals as a function of angle of incidence relative to the <100> (a), <110> (b) and <111> (c), respectively.

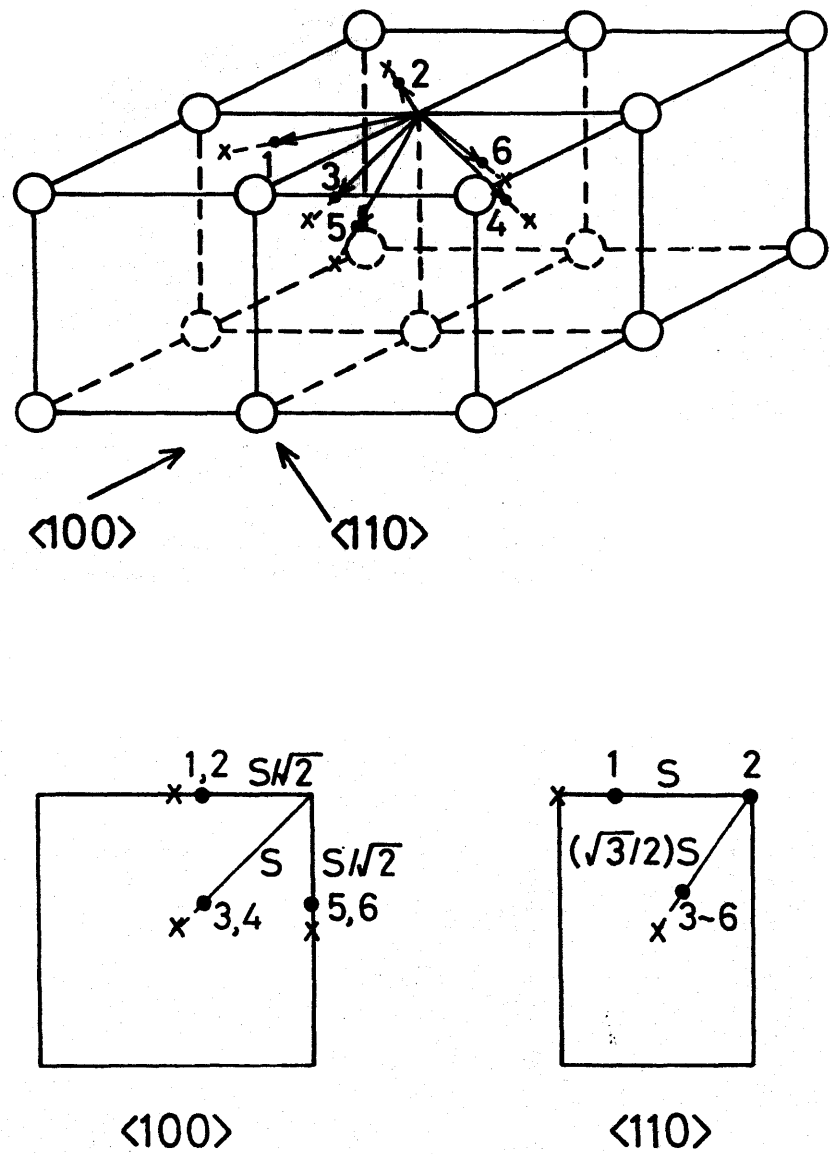

Fig. 4.10 A half of the unit cell of the KCl lattice with projections showing the positions (•) of the impurities which are displaced to the <110> direction by an amount of S, viewed along the <100> and <110> channels. The crosses indicate the face-center position and large open circles indicate host K^+ or Cl^- ions.

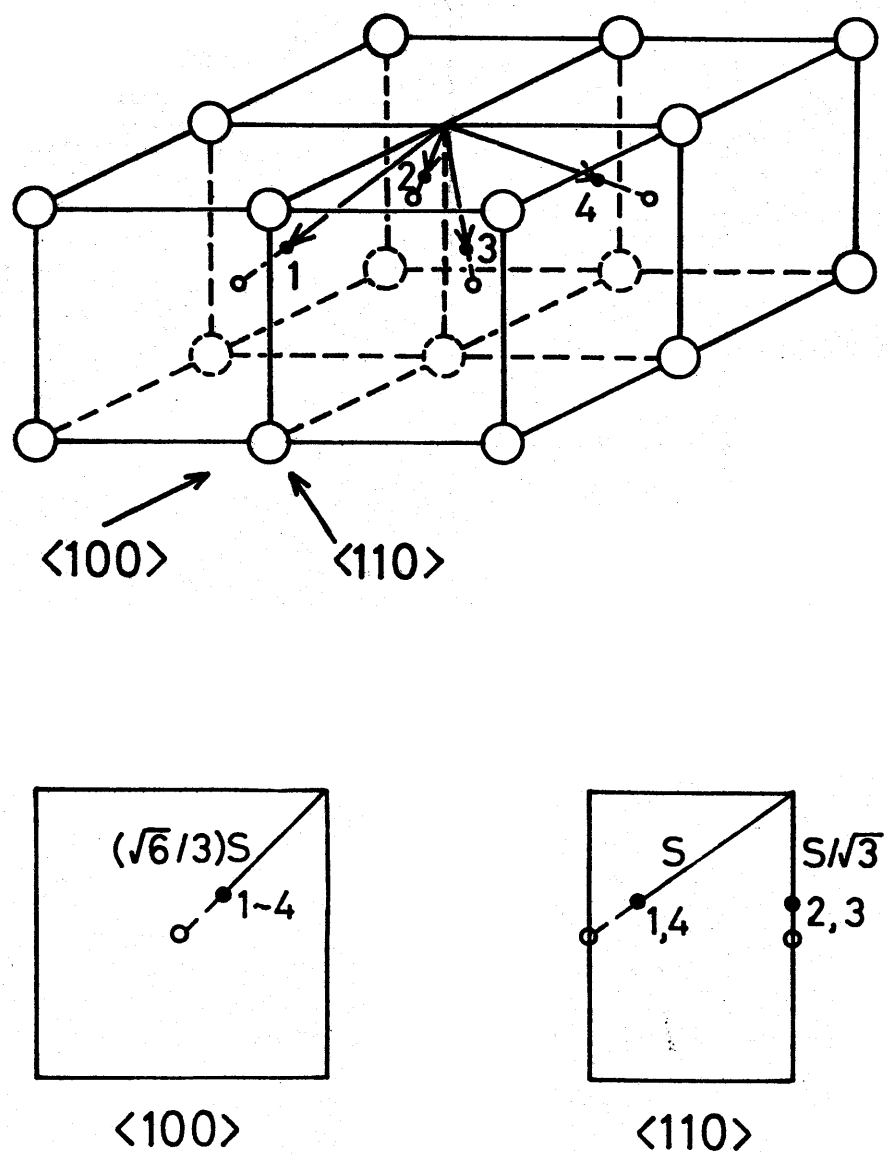

Fig. 4.11 A half of the unit cell of the KCl lattice with projections showing the positions (•) of the impurities which are displaced to the <111> direction by an amount of S, viewed along the <100> and <110> channels. The small open circles indicate the body center and large open circles indicate host K^+ or Cl^- ions.

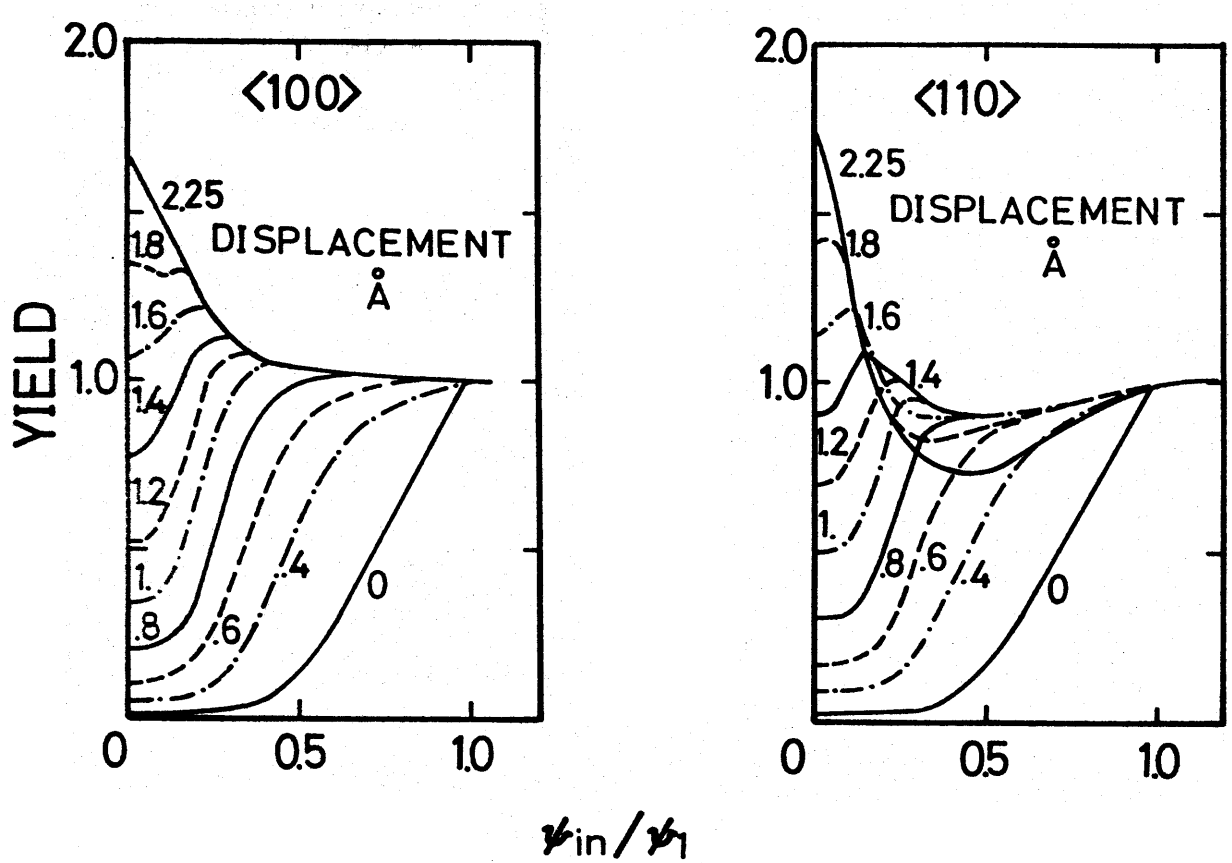

Fig. 4.12 Calculated normalized yield of 1.5 MeV He^+ ions backscattered by the atoms displaced to the <110> direction from the lattice point, for various displacement as indicated by the numbers in the figure, as a function of angle of incidence relative to the <100> and <110> directions of KCl at room temperature. Incident angle is normalized by ψ_1, where ψ_1 is the Lindhard's characteristic angle; $\psi_1 = 0.85^o$ and 0.71^o for <100> and <110> axes, respectively.

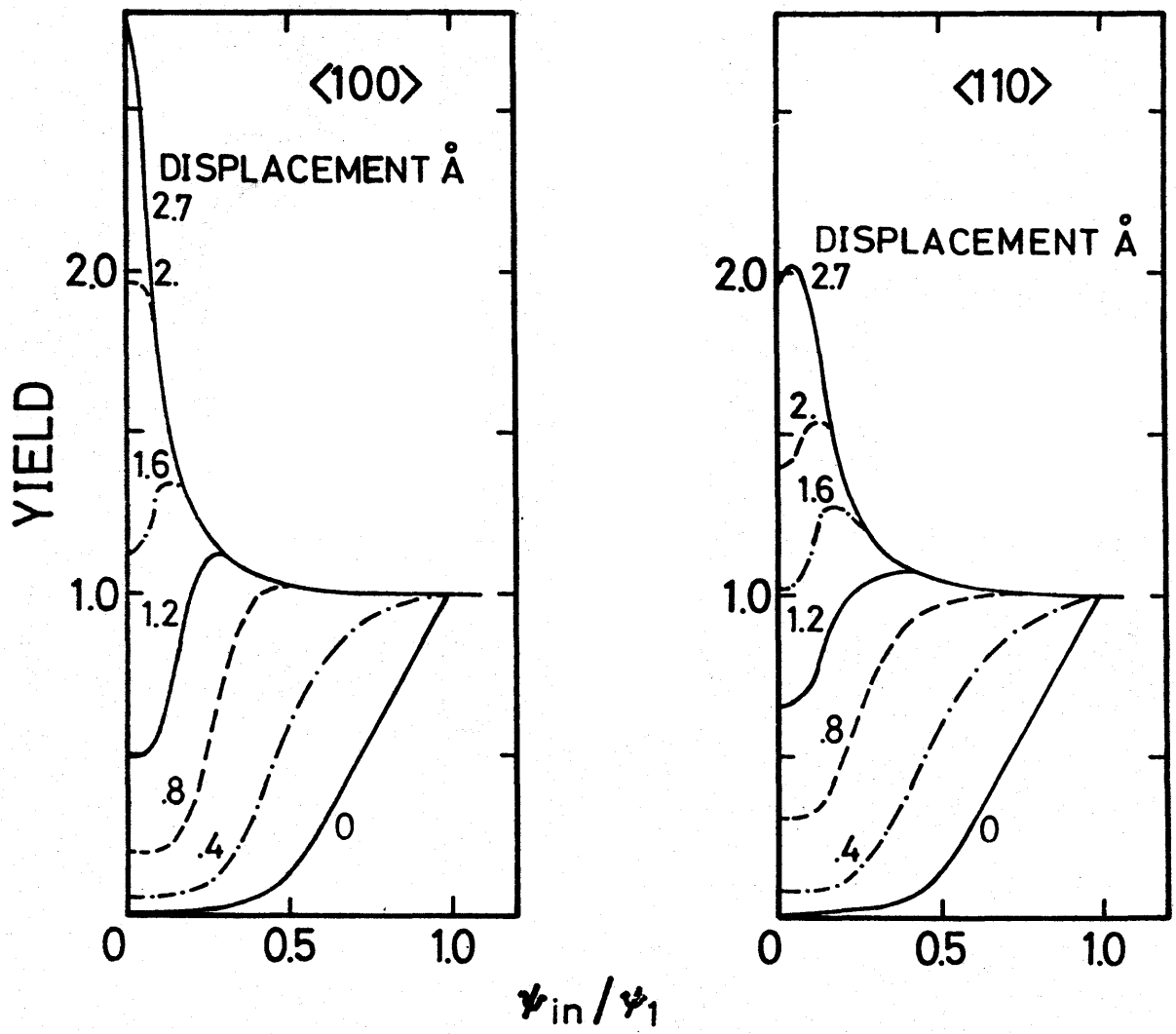

Fig. 4.13 Calculated normalized yield of 1.5 MeV He^+ ions backscattered by the atoms displaced to the <111> direction from the lattice position, for various displacements as indicated by the numbers in the figure, as a function of angle of incidence relative to the <100> and <110> directions in KCl at room temperature. Incident angle is normalized by ψ_1, where ψ_1 is the Lindhard's characteristic angle; $\psi_1 = 0.85^\circ$ and 0.71° for <100> and <110> axes, respectively.

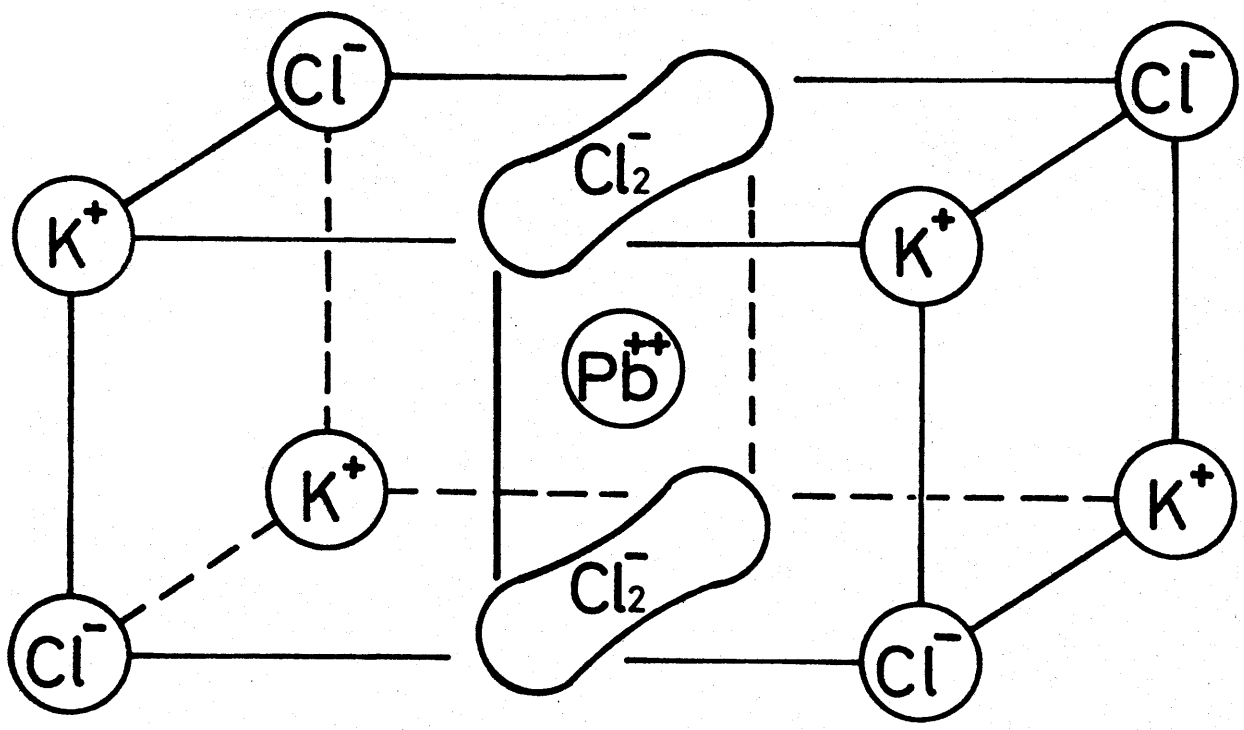

Fig. 4.14 A possible model of the complex of the Pb^{++} and the interstitial chlorine in the irradiated Pb^{++}-doped KCl.

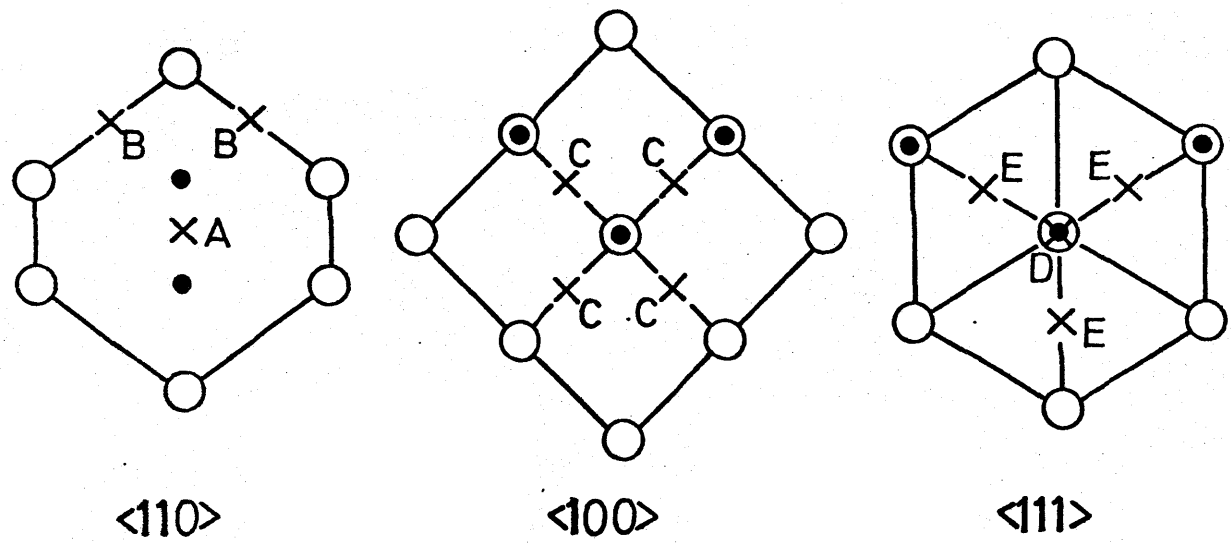

Fig. 4.15 Vertical sections of the <100> , <110> and <111> channels of Si crystals. The hexagol interstitial sites are designated by the crosses and tetrahedral interstitial sites by the closed circles. Open circles indicate Si atoms.

CHAPTER V

DIRECT METHOD OF DETERMINING DEFECT DISTRIBUTION IN ION-IMPLANTED LAYERS

5.1 Introduction

One of the useful applications of channeling technique is the determination of depth dependence of the defect concentration in ion-implanted layers, which is of primary importance for understanding the nature of the implanted layers.[1] Although several methods such as EPR[2], optical reflectance[3] and optical absorption[4] measurements have been employed for the determination of defect concentration and its distribution, the dechanneling measurements[5 - 13] (backscattering technique combined with channeling) are most convenient and have been used extensively, because a good depth resolution is obtained easily without slicing the sample.

The normalized backscattering yield $\chi(z)$ of particles incident along a major axis of crystals at a depth z from the crystal surface may be expressed as [6]

$$\chi(z) = \chi_R(z) + \{1 - \chi_R(z)\} c(z) , \quad (5.1)$$

where $\chi_R(z)$ and $c(z)$ are the random fraction and the fractional defect concentration at z, respectively. The first and second terms are due to the scattering

of dechanneled particles with lattice and displaced atoms and of channeled particles with displaced atoms, respectively. To obtain c(z), it is necessary to know $\chi_R(z)$ at the depth z. The random fraction $\chi_p(z)$ in an undamaged crystal may be obtained experimentally, since the contribution of the second term is neglected. In a damaged crystal, the random fraction may be increased due to the scattering by defects. Then

$$\chi_R(z) = \chi_p(z) + \chi_d(z) , \qquad (5.2)$$

where χ_d is the additive term by defects in $\chi_R(z)$. Several methods to obtain the additive term χ_d have been developed: the methods of the single scattering[6], multiple scattering[6], plural scattering[8] and diffusion (see Chapter III). It is generally accepted that χ_d is dependent on z through the total surface concentration q of defects up to a depth z, which is given by

$$q = N \int_0^z c(t)dt \quad . \qquad (5.3)$$

Here N is the lattice atoms per cm^3.

So far the single or multiple scattering model is usually used for obtaining χ_d and it has been pointed[14] out that the defect concentration derived from the

dechanneling experiments is an overestimate by a factor of about 4 than the value estimated by the EPR measurements. It has been also found that the depth profiles of defect[10] obtained from the dechanneling measurements with the single scattering model have larger maximum-to-surface concentration ratio by a factor of five than the ratio for the theoretical depth profile obtained by Brice[15], as shown in Fig. 5.1. Moreover, it has been pointed out[9] that the half-width of the depth profile of defect concentration derived with the single scattering model increases by a factor of two as the implantation dose increases, which is rather improbable. The arguments made above may make one consider that the previous models underestimate $\chi_d(q)$ for intermediate values of defect concentration q per unit area, as discussed in Chapter III. It is also to be noted that the defect concentration c(z) derived from Eq. (5.1) is critically dependent on the choice of $\chi_d(q)$.

In this circumstance, it is of interest to develop a method, which does not include any assumption on $\chi_d(q)$ and is based on a different standpoint. In this chapter, a new method of deriving $\chi_d(q)$ has been developed, in which an assumption is made on the growth curve of the defect concentration against the dose. In this method $\chi_d(q)$ and c(z) are derived by employing two dechanneling data obtained at two different radiation doses. This method was applied for the experi-

mental data by Eisen[9] on B-implanted Si, and $\chi_d(q)$ and $c(z)$ were obtained and the results were compared with those obtained with the previous method.

5.2 Method of Analysis

According to Eqs. (5.1) and (5.2), the normalized scattering yields $\chi(D_1, z)$ and $\chi(D_2, z)$ at two different doses D_1 and D_2 ($> D_1$), respectively, are given by

$$\chi(D_1, z) = \{ \chi_p(z) + \chi_d(q_1) \} + c(D_1, z)\left[1 - \{\chi_p(z) + \chi_d(q_1)\}\right] , \tag{5.4}$$

and

$$\chi(D_2, z) = \{ \chi_p(z) + \chi_d(q_2) \} + c(D_2, z)\left[1 - \{\chi_p(z) + \chi_d(q_2)\}\right] , \tag{5.5}$$

where q_1 and q_2 are the defect concentrations per unit area for the doses D_1 and D_2, respectively, namely

$$q_1 = N \int_0^z c(D_1, t)dt$$

and

$$q_2 = N \int_0^z c(D_2, t)dt ,$$

where N is the atom density per cm^3. If the function

$f(z)$, which is given by

$$f(z) = \frac{c(D_2, z)}{c(D_1, z)} , \qquad (5.6)$$

is known, one obtaines

$$\chi_d(q_2) = \frac{\{\chi(D_2, z) - \chi_p(z)\} - f(z)\, c(D_1, z)\{1 - \chi_p(z)\}}{1 - f(z)\, c(D_1, z)} . \qquad (5.7)$$

Equations (5.4) and (5.7) may be used to obtain $c(D_1, z)$ and $\chi_d(q)$ in a successive way. Firstly the depth is divided into n sections and the middle point for each section is taken as z_i. If $\chi_d\{q_1(z_1)\}$ at the first segment is known, $c(D_1, z_1)$ may be determined by putting the experimental values of $\chi(D_1, z_1)$ and $\chi_p(z_1)$ into Eq. (5.4). Next, an assumption is made on the dose dependence of the fractional concentration:

$$c(D, z) = 1 - \exp\{-\alpha w(D, z)\} , \qquad (5.8)$$

where $\alpha w(D, z)$ is the absorbed energy per unit volume at a depth z for a dose D and α is a constant. Recent experimental results[3] obtained with the optical reflectance have shown that the exponential dependence is held for $c < 0.8$. The value of $w(D_1, z_1)$ is evaluated

from $c(D_1, z_1)$. Since $w(D_2, z)/w(D_1, z)$ equals to D_2/D_1 independent of z, then $c(D_2, z_1)$ and $f(z_1)$ may be obtained by using the experimental value of D_2/D_1. Now the left hand side of Eq. (5.7) may be calculated, giving the value of χ_d at

$$q_2(z_1) = c(D_2, z_1)\ N\ z_1 = f(z_1)\ c(D_1, z_1)\ N\ z_1 \ . \tag{5.9}$$

The value of $\chi_d(q_1)$ at the next section, namely at $q_1(z_2)$ may be approximated by the value at $q_1\{(z_1 + z_2)/2\} = c(D_1, z_1)\ N\ (z_1 + z_2)/2$ and can be obtained by interpolating the value of $\chi_d\{q_2(z_1)\}$ and $\chi_d\{q_1(z_1)\}$. With $\chi(D_1, z_2)$, $\chi_p(z_2)$ and $\chi_d\{q_1(z_2)\}$, the value of $c(D_1, z_2)$ is obtained. The same procedures can be repeated to the final segment to evaluate two functions: $\chi_d(q)$ and $c(D_1, z)$.

The determination of $\chi_d\{q_1(z_1)\}$ is made as follows. It has been pointed out in Chapter III that the single scattering model is a good assumption at low q. Therefore the most appropriate determination of $\chi_d(q)$ is such that the value of χ_d at low q agrees with the result of the single scattering model. The choice of $\chi_d\{q_1(z_1)\}$, however, does not affect the shape of χ_d vs q curve appreciably, unless the fractional defect concentration is not too large. On the other hand, the determination of D_2/D_1 is not straight-forwards, since the local dose where the experimental analysis is made

can not be determined accurately. In the process of analysis, if D_2/D_1 is chosen too small, the obtained values of $\chi_d(q)$ are much larger than the result of the single scattering calculation, and if D_2/D_1 is chosen too large, the oscillation in the χ_d vs q is observed. Thus the calculation may be repeated until the obtained values of $\chi_d(q)$ at low q agree with the result of the single scattering model and do not show any oscillation.

5.3 Results and Discussion

The experimental results by Eisen[9] for Si implanted with 200 KeV B at -150° C were analyzed with the above procedure. The results obtained from the backscattering yield of 450 KeV H^+ incident along the <110> direction at two different implantation doses of B are shown in Figs. 5.2 and 5.3. Figure 5.2 shows $\chi_d(q)$ obtained with the present method and also with the single scattering and multiple scattering models. $\chi_d(q)$ in Fig. 5.2 was obtained with $D_2/D_1 = 2.2$. For $D_2/D_1 = 2.4$, the obtained $\chi_d(q)$ shows the oscillation and its value at high q is smaller than the result of the multiple scattering calculation. It is seen that $\chi_d(q)$ is a linear function of q at low q, in good agreement with the result of the single scattering calculation. The deviation takes place at $q = 4 \times 10^{16}$ cm^{-2}, and the obtained values of $\chi_d(q)$ are larger than the results of the single and multiple scattering calculations for

intermediate q. This result is consistent with the results of the diffusion calculation (see Chapter III) and is easily understood, since at low q the particles in a channel are concentrated near the center of a channel and the distribution begins to be modified by defects with increasing q. This modification of the particle distribution in a channel causes the interference effect between dechanneling by defects and by thermally vibrating strings and electrons, producing larger $\chi_d(q)$ at intermediate q. It has been shown that the modification is more predominant as the interstitial atoms are located nearer to the center of the channel.

The backscattering yield $\chi(D_1, z)$ and the random fraction $\chi_d(q)$ are compared in Fig. 5.3. Figure 5.3 also shows the obtained value of $c(D_1, z)$ and the depth profile of the energy deposition by elastic encounters.[15] The shape of the concentration vs depth curve is rather smooth and is much different from the result obtained with the single scattering model: for the latter the value of c near the maximum reaches 0.55. As seen from the figure, the present result is close to the Brice's depth profile of elastic energy deposition. The accuracy for depth profile of defects is worse than that for the $\chi_d(q)$ curve. As pointed out already in Chapter III, $\chi_d(q)$ curve is not only a function of q but depends on the local concentration slightly, causing errors in the estimation of c(z). It is clear, however, that the

obtained $\chi_d(q)$ is considerably different from that derived from the single and multiple scattering models. The apparent increase in the width of the damaged layer and non-linear increase in the defect concentration against the radiation dose may partly originate from the non-linear increase in $\chi_d(q)$. This situation may be seen more clearly in Fig. 5.4. The broken curves of Fig. 5.4 show the calculated backscattering yield obtained with $\chi_d(q)$ shown in Fig. 5.2 and c(z) obtained by multiplying various factors to the defect concentration shown in Fig. 5.3; the peak values of c(z) being indicated by the numbers for each curve in Fig. 5.4. The solid lines show the experimental backscattering yield used for the present analysis.

From Fig. 5.4, it is seen that the backscattering yield begins to increase at small depth and increases super linearly over wide range of the depth against the radiation dose. These depth profiles are rather common for the backscattering experiments. If those backscattering data are analyzed with the single scattering model, in which $\chi_d(q)$ is a linear function of q, the scattering yield shown in Fig. 5.4 may result in the super-linear increase of defect concentration and in the change of the width of the damaged layer as the radiation dose increases. It should be noted that these curves were obtained with the same defect profile. The increase of the width for the single scattering analysis may be

ascribed to the assumption that $\chi_d(q)$ depends linearly on q. This difficulty may be solved by taking into consideration the non-linear dependence of $\chi_d(q)$ on q obtained with the diffusion calculation.

The present method has been also applied for the backscattering data of 1 MeV He^+ in the <110> channel of Si at room temperature obtained by Eisen. $\chi_d(q)$ and c(z) obtained with the present method are shown in Fig. 5.5 (curve (e)) and Fig. 5.6 (dotted line). In Fig. 5.5 the result is compared with those of the single scattering (s), plural scattering (p), multiple scattering (m) and diffusion (d) calculations. For the diffusion calculation, the diffusion coefficient was obtained by taking the upper limit $\varepsilon_\perp^U$ of the integral as 10 $\varepsilon_\perp^c$ where $\varepsilon_\perp^c$ is the critical transverse energy (see, Sec. 3.2.3). The results of diffusion calculation are obtained for c = 1.5 % (solid line) and c = 5 % (dotted line), respectively. The experimental result (e) increases similarly to that of the single scattering calculation for $q < 4 \times 10^{16}$ cm^{-2}, and is much larger than those of the single, plural and multiple scattering calculations for $q > 4 \times 10^{16}$ cm^{-2}, being in good agreement with those of the diffusion calculation. The defect concentration c(z) (broken curve) is also in good agreement with the theoretical elastic energy deposition obtained by Brice (solid curve), as shown in Fig. 5.6.

Figure 5.3 indicates also that the value of χ_d are rather close to the values of $\chi(z)$ near the maximum

of c(z). This result raises a question why $\chi_d(z)$ should decrease with increasing z after the particles penetrate the disordered layer. The decrease in $\chi_d(z)$ with increasing z may be understood in view of the fact that the particle distribution in a channel is highly modified in the presence of defects. In order to understand this rechanneling process, Fig. 5.7 compares the particle distribution as a function of the transverse energy in a disordered channel (curve a) and a perfect channel (curve b) for 1 MeV He^+, calculated with the diffusion model described above. The curves are the particle distribution at a depth of 1 μm for the disordered channel and at a depth of 15 μm for the perfect channel and are normalized by the area under the curve between $\varepsilon_\perp = 0$ and $\varepsilon_\perp^c$. The channeled fractions for both cases are 0.75. It is seen from the figure that the distributions are much different. As the particles penetrate through the disordered region the particle distribution, which has a shape such as curve (a) may tend to have a shape such as curve (b). This effect causes the particles with $\varepsilon_\perp > \varepsilon_\perp^c$ to put back into the region $\varepsilon_\perp < \varepsilon_\perp^c$. The amount of rechanneling may depend on the value of χ_d at the disordered layer, and since for larger χ_d, the particle distribution near $\varepsilon_\perp \sim 0$ is strongly suppressed, it is expected that the amount of rechanneling divided by χ_d should be larger for larger χ_d. It is also to be noted

that the maximum of $c(z)$ takes place at a smaller value of z than that estimated with the previous methods. Accurate determination of the maximum position can not be made until the rechanneling effect is evaluated quantitatively.

Now discussion is made on the assumption in deriving Eq. (5.1). According to the results described in Chapter II, more exact representation of the scattering yield $\chi(z)$ than Eq. (5.1) may be

$$\chi(z) = \{1 - c(z)\} \langle F(\vec{r}, z)\rangle_1 + c(z) \langle F(\vec{r}, z)\rangle_d , \tag{5.10}$$

where $F(\vec{r}, z)$ is the flux distribution of the particles at a depth z for the incident angle $\psi_{in} = 0$, and $c(z)$ is the fractional concentration of defects. The first term is due to the scattering by lattice atoms. $\langle\ \rangle_1$ means the averaging the flux distribution by thermal displacements of lattice atoms around the lattice position, which is given by

$$\langle\ \rangle_1 = \int_1 F(\vec{r}, z)\ P(\vec{r}) d\vec{r} \quad . \tag{5.11}$$

Here $P(\vec{r})$ is the probability that lattice atoms located at $\vec{r}$ in the channel. $\langle\ \rangle_1$ is equal to the random fraction $\chi_R(z)$. The second term is due to the scattering by displaced atoms. In the same way, $\langle\ \rangle_d$ is given by

$$< \; >_d = \int_d F(\vec{r}, z) \; P(\vec{r}) d\vec{r}. \qquad (5.12)$$

The integral also means the average of $F(\vec{r}, z)$ around the displaced atoms. This factor depends on the defect structure.

Recently, it has been shown[16] that about a half of the Si interstitial atoms produced by irradiation occupy the hexagonal site and another half of the Si interstitial atoms occupy the bond-center site by comparing the experimental angular yield obtained with double-alignment technique and the theoretical angular yield of Monte Carlo calculations. Employing these results, the maximum of the averaged flux that the Si interstitial atoms feel was estimated to be ~1.3, which was averaged from surface to 4000 A. This value of 1.3 should be reduced by dechanneling due to Si interstitial itself and by averaging the flux due to thermal displacements of Si interstitials and may be approach to unity. Furthermore taking into account the condition $\chi(z) \leqq 1$, which was confirmed experimentally, $< \; >_d$ is approximated by unity within an error of 10 ~ 20 %. Thus the usage of Eq. (5.1) instead of Eq. (5.10) is justified.

5.4 Conclusion

A new method of determining the random fraction and the defect concentration in a implanted layer has been developed. In this method, two backscattering yields obtained at two different implantation doses are employed and the assumption of exponential growth curve of defect concentration against the implantation dose is made. The backscattering data for Si implanted with B obtained by Eisen have been analyzed with the present method. The random fraction obtained with the present method shows a linear dependence on the surface concentration q of defects at low q.and is much larger than the random fraction calculated with the single, multiple and plural scattering models above a certain value of q. These results are in good agreement with the results of diffusion calculation. The obtained depth profile of defect concentration also shows good agreement with that of the elastic energy deposition obtained by Brice. It is found that the previous method, in which the random fraction depends linearly on the surface concentration of defects, leads to the difficulties: the defect concentration is a super linear function of the radiation dose and the width of the damaged layer increases as the implantation dose increases. These difficulties may be solved by using the non-linear relation between the random fraction and surface concentration of defects, as suggested by diffusion model.

References

1. J. W. Mayer, L. Eriksson and J. A. Davies, "Ion Implantation in Semiconductors" (Academic Press, New York, 1970).
2. K. L. Brower, F. L. Vook and J. A. Borders, Appl. Phys. Letters 16, 108 (1970).
3. E. T. Yen. B. J. Masters and R. Kastel, "Ion Implantation in Semiconductors," ed. by Namba (Plenum Press, New York, 1975). p. 501.
4. H. J. Stein, F. L. Vook and J. A. Borders, Appl. Phys. Letters 16, 106 (1970).
5. J. W. Mayer, L. Eriksson, S. T. Picraux and J. A, Davies, Can. J. Phys. 46, 663 (1968).
6. E. Bøgh, Can. J. Phys. 46, 653 (1968).
7. L. C. Feldman and J. W. Rodgers, J. Appl. Phys. 41, 3776 (1970)
8. J. E. Westmoreland, J. W. Mayer, F. H. Eisen and B. Welch, Rad. Effects 6, 161 (1970).
9. F. H. Eisen, B. Welch, J. E. Westmoreland and J. W. Mayer, "Atomic Collision Phenomena in Solids," ed. by D. W. Palmer, M. W. Thompson and P. D. Townsend (North-Holland, Amsterdam, 1970) p. 111.
10. J. F. Ziegler, J. Appl. Phys. 43, 2973 (1972).
11. K. Schmid, Rad. Effects 17, 201 (1973).
12. K. L. Merkle, P. P. Promko, D. S. Gemmell, R. C. Mikkelson and J. R. Wrobel, Phys. Rev. B8, 1002 (1973).
13. P. P. Pronko, J. Bøttiger, J. A. Davies and J. B. Mitchell, Rad. Effects 21, 25 (1974).

14. T. Tsurushima and H. Tanoue,
"Ion Implantation in Semiconductors,"
ed. by S. Namba (Plenum Press, New York, 1975) p. 429

15. D. K. Brice, Rad. Effects 6, 77 (1970).

16. K. Morita and H. D. Carstanjen, Rad. Effects (in print).

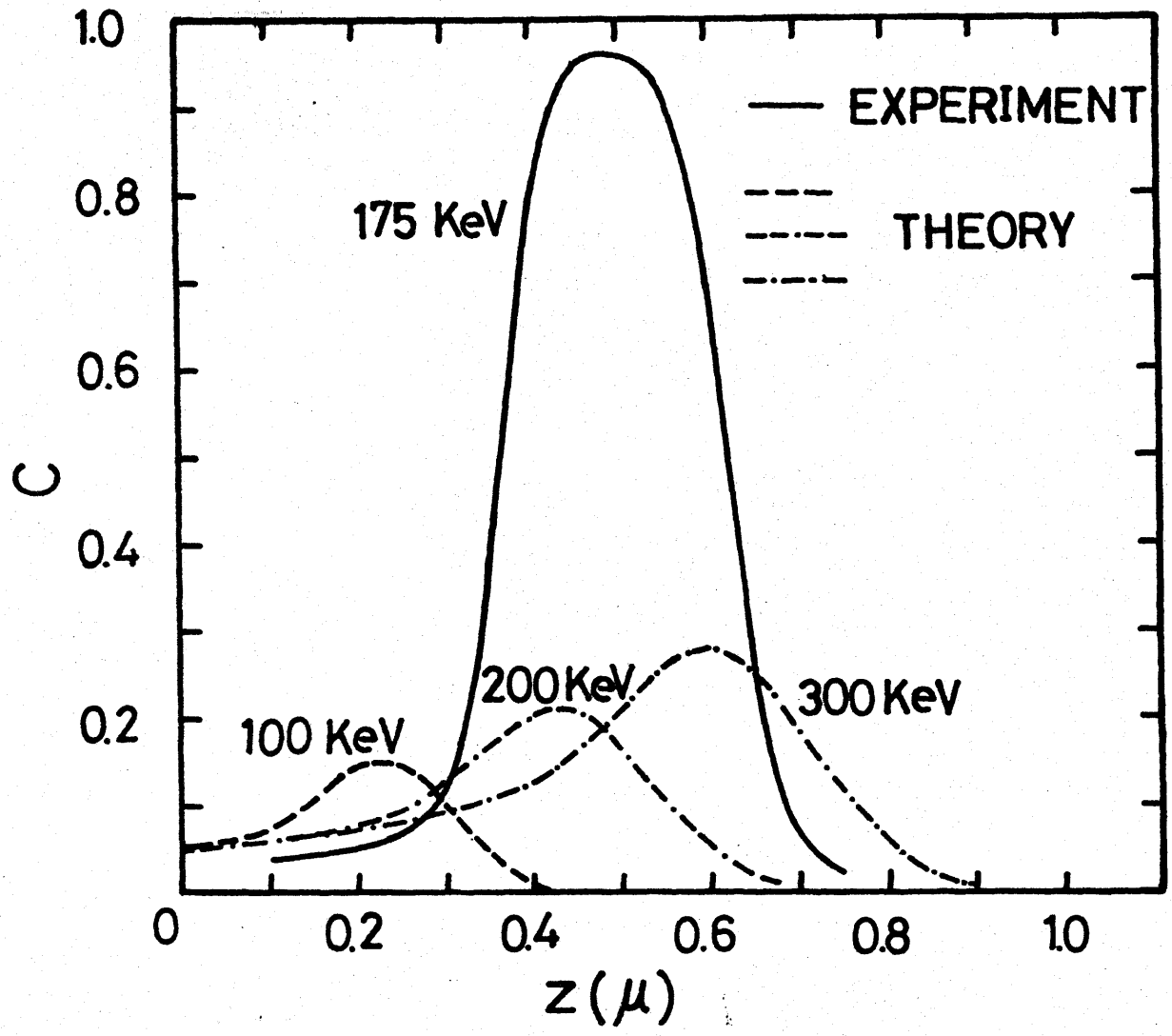

Fig. 5.1 Comparison between a typical experimental depth profile of defect concentration derived with the single scattering model and the theoretical depth profiles of elastic energy deposition in Si implanted with B^+ of energies indicated by the numbers. The solid curve is the experimental result obtained by Ziegler, with 2.5 MeV He^+. The broken, double dash-dot and dot-dash curves are the results calculated by Brice.

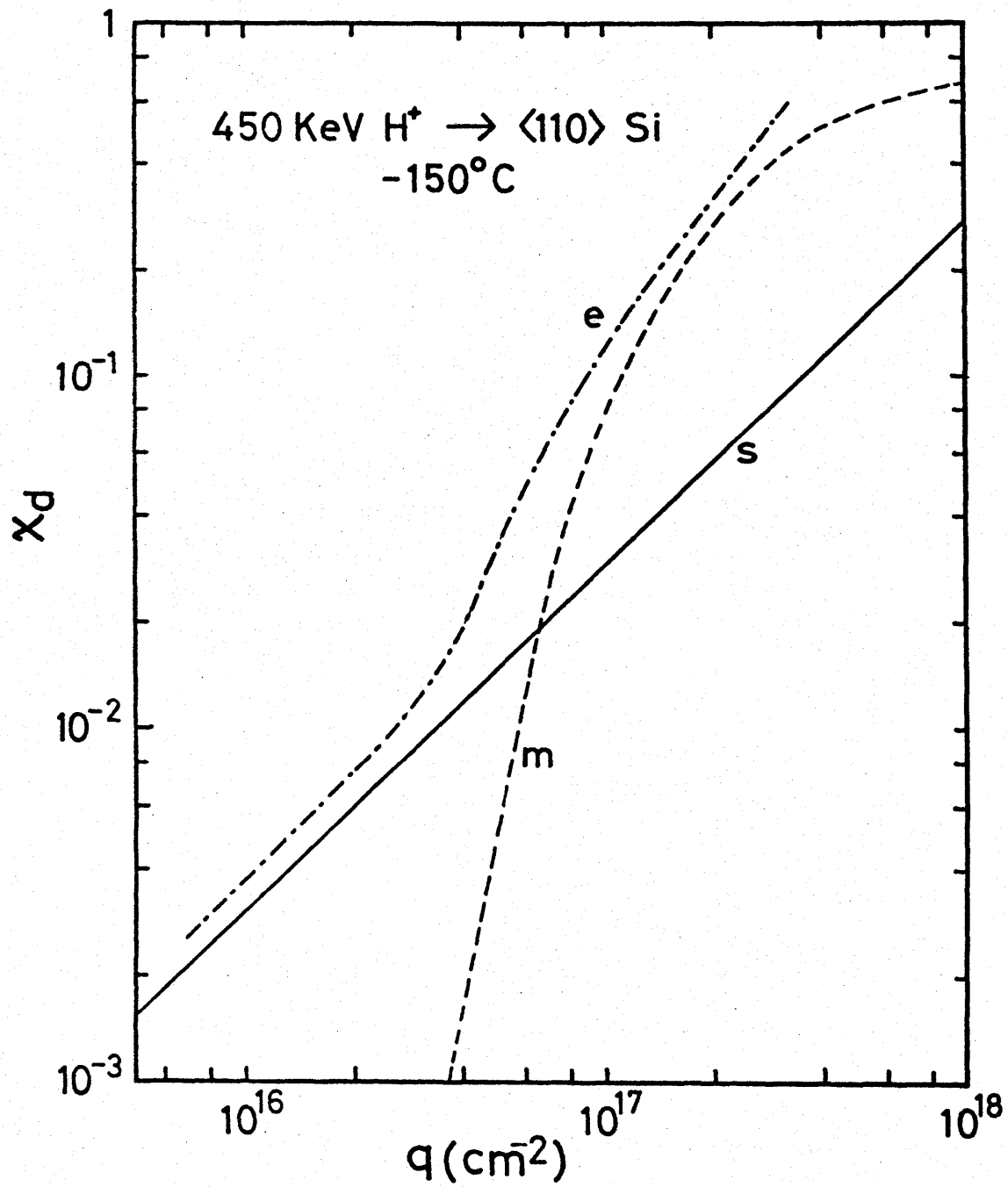

Fig. 5.2 Random fraction $\chi_d(q)$ for 450 KeV protons in Si implanted with 200 KeV B at -150° C, derived with the present method (curve e), the single scattering model (curve s) and the multiple scattering model (curve m).

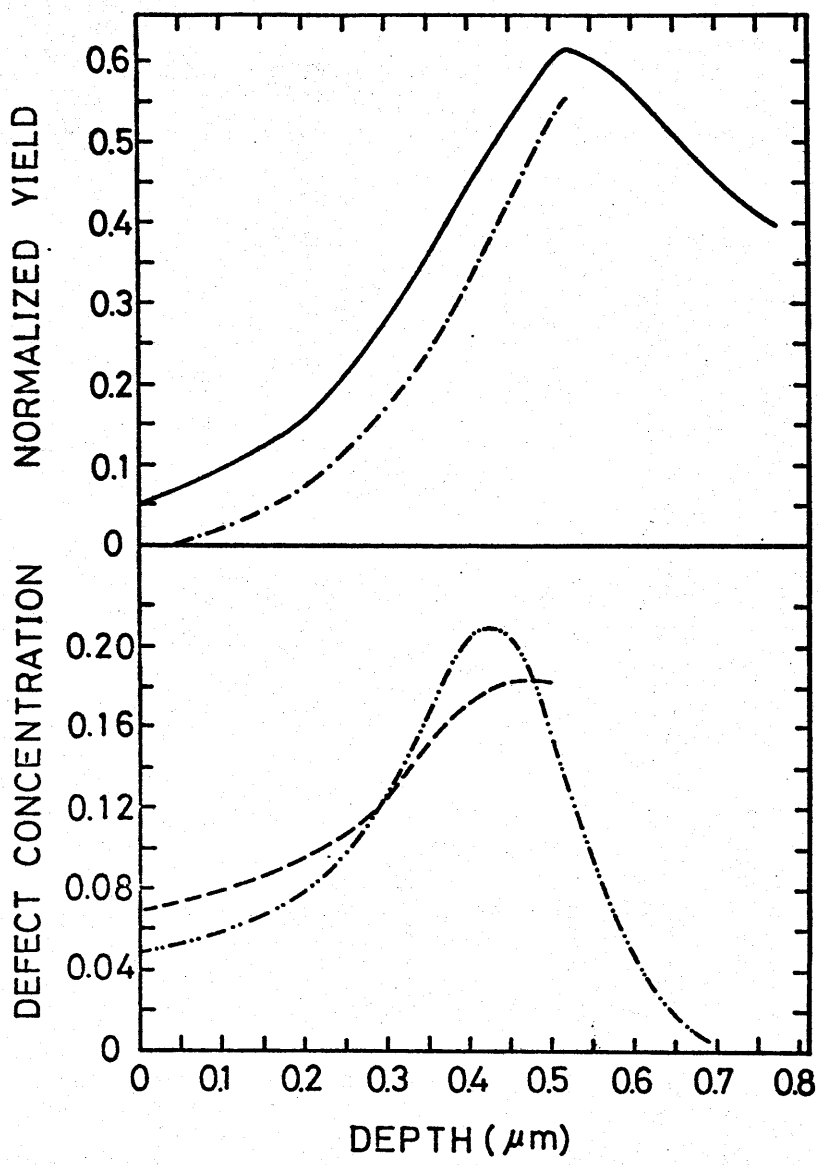

Fig. 5.3 Fractional defect concentration (broken curve) as a function of depth for Si implanted with 200 KeV B at -150° C derived from the depth dependence of the backscattering yield of 450 KeV H^+ incident along the <110> direction of Si (solid curve). Another backscattering data obtained at higher doses are used. The obtained random fraction (dot-dash curve) and depth profile of elastic energy deposition (double dot-dash curve) calculated by Brice are also shown.

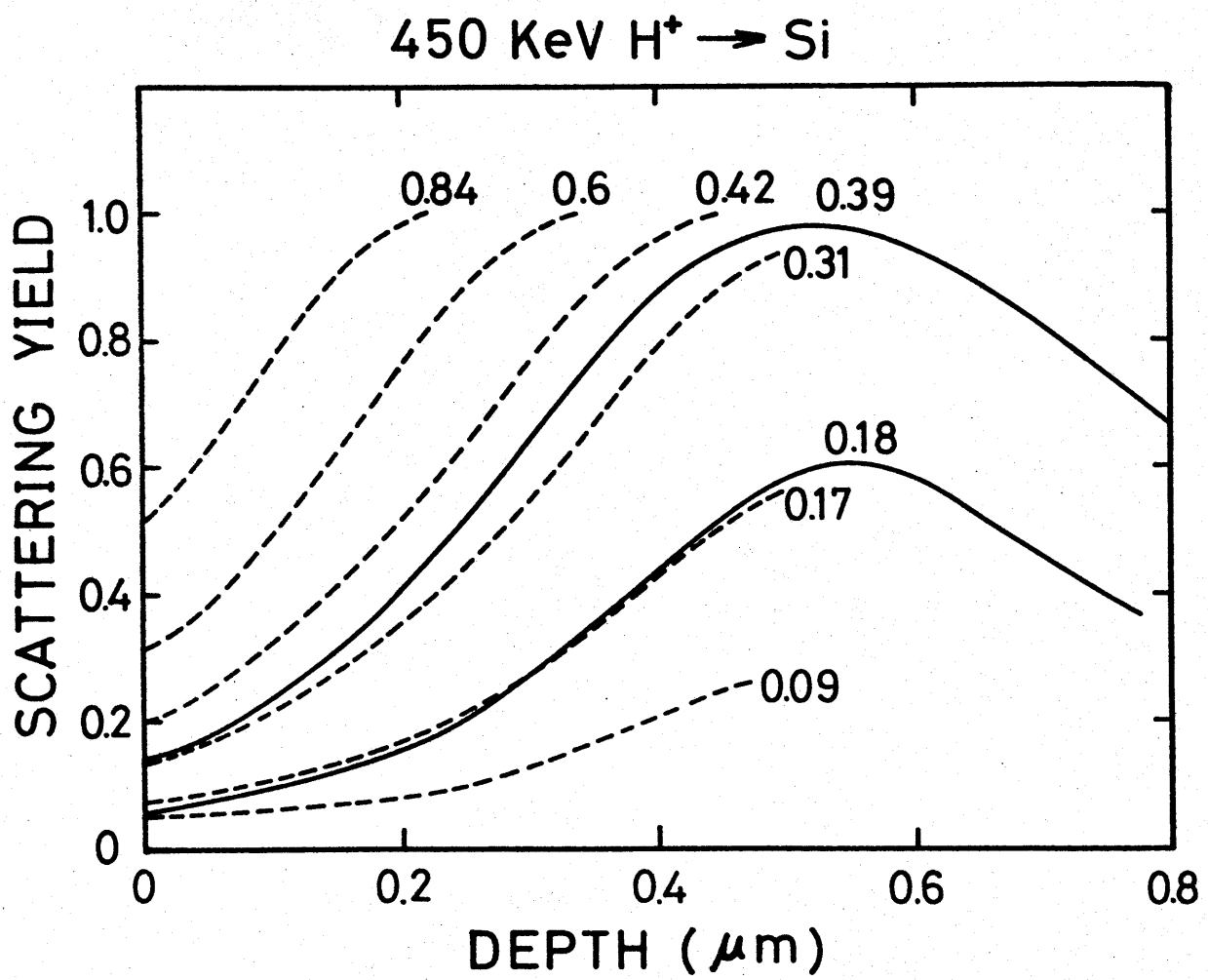

Fig. 5.4 Calculated backscattering yield obtained with the curve (e) of $\chi_d(q)$ shown in Fig. 5.2 and the same depth profile of c(z) as the broken curve shown in Fig. 5.3. The peak values of c(z) are designated by the numbers. The experimental backscattering yields used for the present analysis are also shown (solid lines).

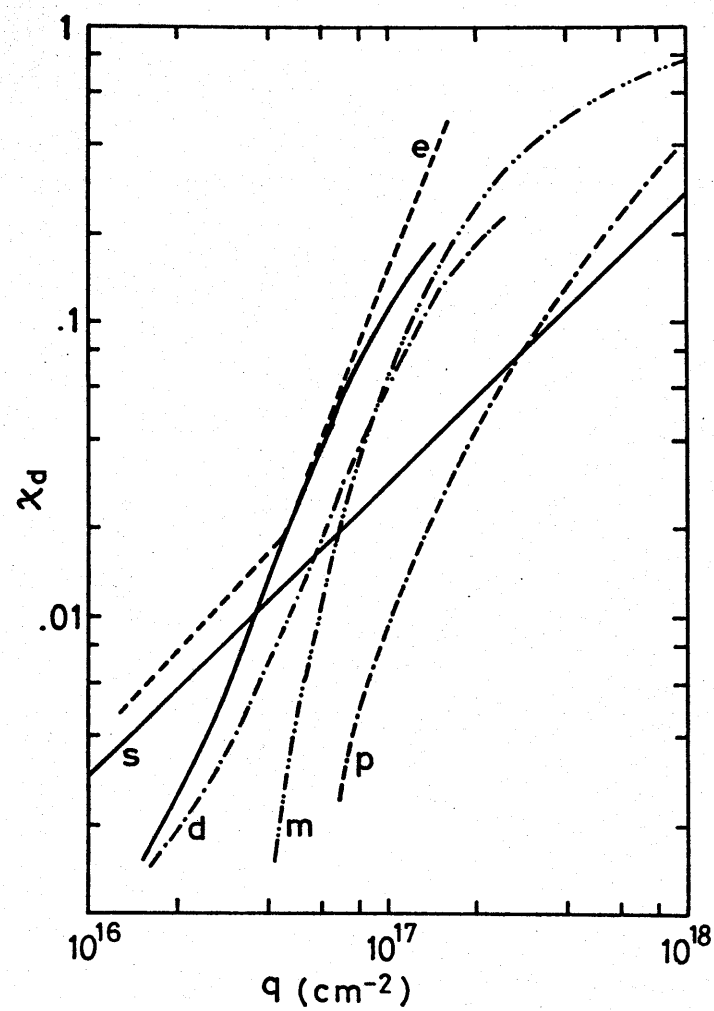

Fig. 5.5 Random fraction χ_d caused by defects, calculated with the single scattering (s), multiple scattering (m), plural scattering (p) and diffusion (d) models, as a function of defect concentration q per cm^2, for 1 MeV He^+ incident along the <110> direction of Si. The curves denoted by d were obtained for the volume defect concentration c=1.5 % (solid curve) and c=5 % (dot-dash curve). The curve e was derived from the backscattering spectra of Si implanted with B at room temperature measured by Eisen.

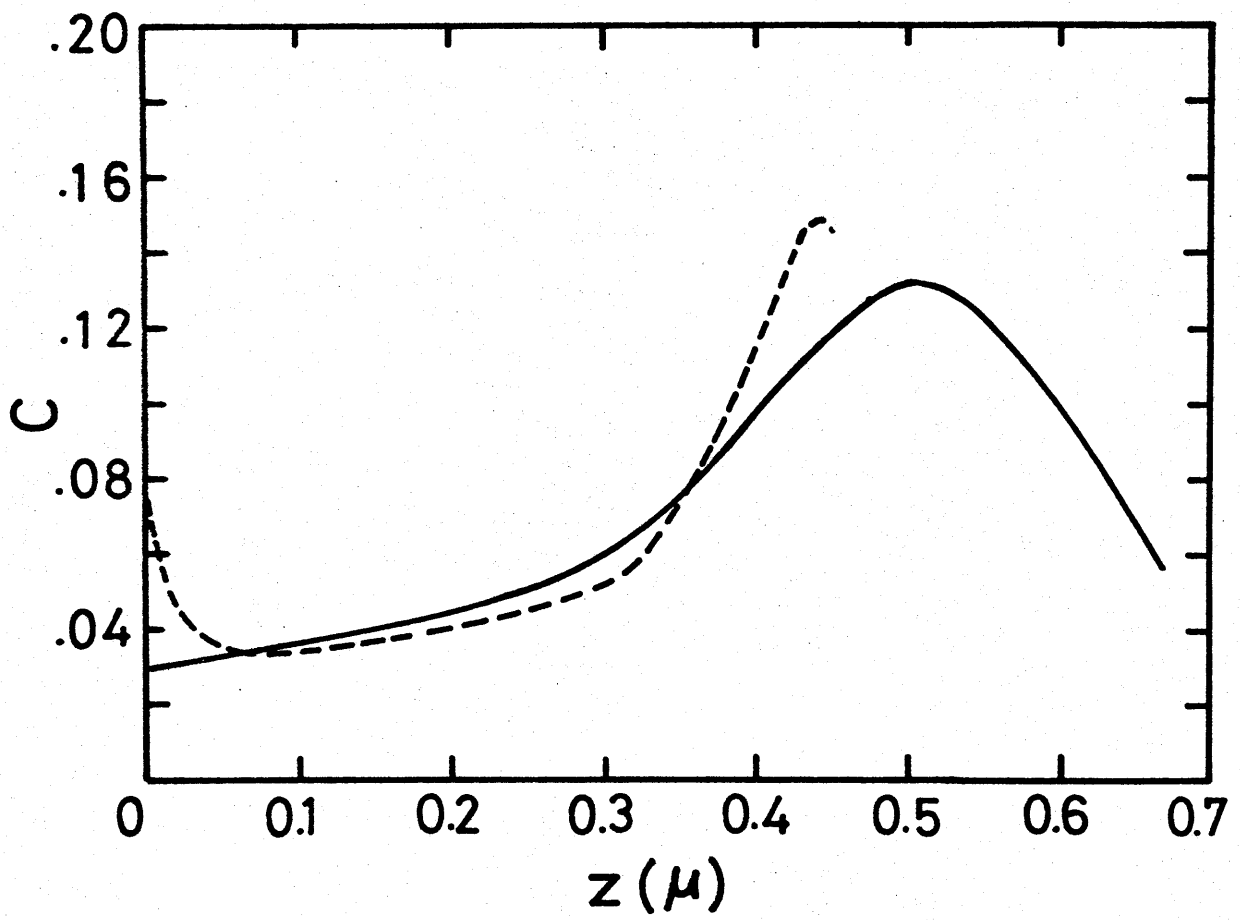

Fig. 5.6 Fractional defect concentration c(z) (broken curve) as a function of depth z for Si implanted with 200 KeV B at room temperature derived from the depth dependence of the backscattering yield of 1 MeV He^+ incident along the <110>direction. The depth profile of elastic energy deposition calculated by Brice is also shown (solid line).

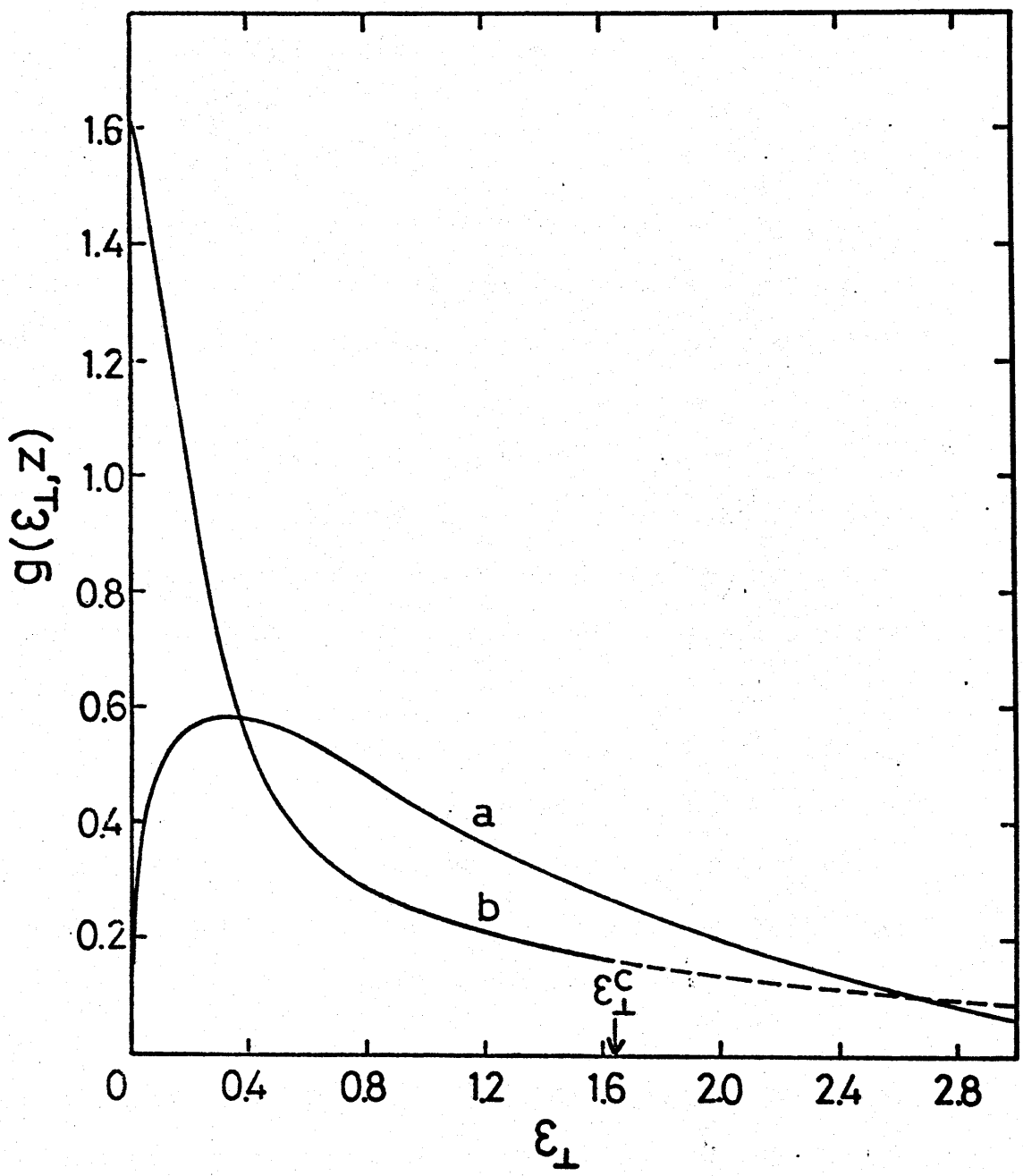

Fig. 5.7 Particle distribution $g(\varepsilon_\perp, z)$ in a channel containing 5 % interstitial atoms at z=1μm (curve a) and in a perfect channel at z=15μm (curve b), where z is the depth from the surface, as a function of the reduced transverse energy $\varepsilon_\perp$, obtained by solving the diffusion equation for 1 MeV He^+ in the <110> channel of Si.

CHAPTER VI

CONCLUSIONS

The problems underlying the usage of the channeling technique for defect studies are investigated. The validity of the simple continuum approximation in employing for the atom location is presented and a new effect which is important for the determination of defect concentration is pointed out. Experimental studies of the location of some impurities in Si and an alkali halide are also made. The important conclusions drawn in the present studies are given below.

In order to examine the validity of the continuum approximation, the flux distribution of channeled particles is calculated for MeV He^+ incident on the <100> channel of Cu as a function of the incident angle, with an analytical method based on the continuum approximation. The angular dependence of the flux is compared with that of the Monte Carlo calculation by Morgan and Van Vliet and good agreement is obtained for the positions not very close to the atomic row nor to the side of the channel. The half-angles are obtained and are in good agreement with those of the Monte Carlo calculation by Barrett. The minimum yield obtained with the present method is smaller by a factor of three than that by Barrett. The discrepancy has been ascribed to the

facts that the effectiveness factor of the Monte Carlo calculation is larger than that of the continuum calculation due to the focusing effects. The focusing effects, however, are found to make little contribution to the effectiveness factor of the atoms located inside the channel. Thus it is concluded that the continuum approximation may give good results for the location of atoms inside the channel.

The channeled particle distribution in the transverse energy for 1.5 MeV H^+ in the <100> channel including displaced atoms is calculated employing a diffusion equation and effects of displaced atoms on the channeled particle distribution and on the dechanneling are investigated. The diffusion coefficients caused by displaced atoms are found to be dependent on the distance of the displacement and dominant at low transverse energies, while the diffusion coefficients caused by electrons and thermally vibrating lattice atoms are dominant at high transverse energies. It is shown that the displaced atoms modify the channeled particle distribution; the modification of the particle distribution is remarkable when the displaced atoms are located near the center of the channel. The random fraction of the diffusion calculation is compared with that of the single, plural and multiple scattering calculations. It turns out that the modification of the channeled particle distribution combined with the

interference effect between the scattering by the displaced atoms and the scattering by electrons and thermally vibrating lattice atoms enhance the dechanneling rate and increase the random fraction.

Under the consideration of the results obtained above, channeling technique is applied for the determination of the impurity location. It is found that substantial fraction of Pb impurities in irradiated KCl crystal is located at the face-center position by comparing the experimental and theoretical angular dependence of the backscattering yields from Pb impurities. The optical absorption studies have shown that the displacement of Pb impurities from the normal lattice site to the face-center is ascribed to the association of Pb impurities with the radiation-induced interstitial chlorines. A model of the complex of the Pb impurities and the interstitial chlorines is suggested. It is also found that the diffusion-doped Au impurities in Si are located at the hexagonal-interstitial position.

A new method of the determination of the defect concentration and of the random fraction in ion-implanted layers is developed. In this method, two backscattering data obtained at two different implantation doses are employed. The random fraction obtained with the present method is in good agreement with that of the diffusion calculation, indicating that the modification of the channeled particle distribution combined with the inter-

ference effect play an important role in dechanneling caused by defects. The depth dependence of the defect concentration is also obtained and in good agreement with that of the theoretical energy deposition.

The results of the present thesis would be useful for the determination of defect concentration and structures in various crystals. Particularly the results described in Chapter V may be useful for the empirical determination of the random fraction in an ion-implanted layer if correct backscattering data at severeal implantation doses are obtained. It turns out that the continuum approximation is appropriate for determining an impurity located near the center of the channel. If an impurity is found to be located apart from the center of the channel, the detailed comparison between the experimental and theoretical angular dependence of the scattering yield from the impurity would provide more conclusive results for the validity of the continuum approximation. Although the interference effects have been demonstrated both from theoretical calculation and from an analysis of the backscattering data, measurements of the particle distribution transmitted from a thin crystal may give more direct evidence of the interference effect through the modification of the particle distribution. In addition, the determination of the location of the interstitial chlorines by means of the double alignment technique would confirm the present model of the complex

of Pb^{++} impurities and interstitial chlorines in an irradiated KCl crystal.

ACKNOWLEDGEMENTS

I would like to express my greatest thanks to Professor N. Itoh for the guidance, discussion and encouragement over the period of this work.

I am also much indebted to Professor K. Morita, with whom most of the channeling experiments were carried out, for valuable discussions, advices and encouragement.

I wish to thank Professor M. Tamagawa for helpful discussions and advices.

I also appreciate my friends and the past and present members of Professor Itoh's laboratory, especially the following people:

Professor M. Ikeya and Dr. M. Saidoh, with whom the crystals of alkali halides were made and the optical absorption studies were performed, for helpful discussions;

Mr. S. Miyagawa, Mr. K. Tachibana and Mr. N. Iue, with whom most of the channeling experiments were performed, for useful discussions;

Mr. Y. Yokoyama, with whom the channeling and optical absorption experiments were carried out, for helpful discussions and his assistance with some of the computer calculation;

Dr. T. Nakayama, Dr. T. Chong and Mr. M. Banno for their assistance with some of the experiments;

Mr. A. Noda and Mr. K. Fukihara for their opera-

tion of the Nagoya University 2 MeV Van de Grraff accelerator;

Members of the Nagoya University Computation Center for making the Facom 230 - 60 computer available;

Messrs. Katoh and Takahashi for their helf of making the goniometer and some equipments for the channeling experiments;

Messrs. Imura and Watanabe for their help of making the equipments for crystal preparation;

Dr. Y. Yoshida for supplying Au-doped Si crystals and discussions;

Dr. F. H. Eisen for supplying the backscattering data of the B-implanted Si crystals and helpful discussions;

Miss. Atomi and Miss. Matsuda for typing a part of the preliminary manuscript, of this thesis.

I also wish to thank my father and mother for their patience for a long period.

I am especially indebted to Miss. M. Hashimoto, who typed this thesis and the preliminary manuscript, for her constant encouragement and understanding.

List of Publication

1. S. Miyagawa, K. Morita, N. Matsunami, K. Tachibana and N. Itoh,
   "Proton Dechanneling in Alkali Halide Mixed Crystals,"
   Radiation Effects 13, 271 (1972).
2. N. Iue, N. Matsunami, K. Morita and N. Itoh,
   "Location of Diffusion-Doped Gold Atoms in Silicon by Means of Channeling,"
   Radiation Effects 14, 191 (1972).
3. N. Matsunami and N. Itoh,
   "Effect of Atomic Displacement on Dechanneling,"
   Phys. Letters 43A, 435 (1973).
4. N. Matsunami and N. Itoh,
   "Effect of Lattice Defects on Dechanneling and on Channeled-Particle Distribution,"
   Atomic Collisions in Solids, ed. by S. Datz, B. R. Appleton and C. D. Moak
   (Plenum Press, New York, 1975) p. 175.
5. N. Matsunami and N. Itoh,
   "On the Determination of Defects Distribution in Implanted Layers by Means of Backscattering Technique,"
   Ion Implantation in Semiconductors, ed by S. Namba
   (Plenum Press, New York, 1975) p. 485.
6. N. Matsunami,
   "Dechanneling and Modification of Particle Distribution Induced by Lattice Defects,"
   J. Phys. Soc. Japan 38, 848 (1975).

7. N. Matsunami and N. Itoh,
"Empirical Determination of the Random Fraction in Disordered Channel,"
Radiation Effects 26, 172 (1975).

8. N. Matsunami, Y. Yokoyama and N. Itoh,
"Displacement of Impurities through Interaction with Radiation-Induced Interstitials in Alkali Halides,"
(to be published).

List of Papers Submitted to Conferences

I International

1. K. Morita, K. Tachibana, S. Miyagawa, N. Matsunami and N. Itoh,
   "Studies of Colour Centers by Means of the Channeling Technique,"
   Colour Centers in Ionic Crystals at Reading, England, 1971.
2. K. Morita, N. Itoh, K. Tachibana, S. Miyagawa and N. Matsunami,
   "Contribution of Electronic and Nuclear Collisions to Dechanneling of Charged Particles,"
   Atomic Collisions in Solids at Gausdal, Norway, 1971.
3. N. Matsunami and N. Itoh,
   "Effects of Lattice Defects on Dechanneling and on Channeled-Particle Distribution,"
   Atomic Collisions in Solids at Gatlinburg, U. S. A., 1973.
4. N. Matsunami and N. Itoh,
   "On the Determination of Defects Distribution in Implanted Layers by Means of Backscattering Technique,"
   Ion Implantation in Semiconductors at Osaka, Japan, 1974.

5. N. Matsunami and N. Itoh,
"A New Method of Analyzing Dechanneling Experiments for Disordered Channel,"
Ion Beam Surface Layer Analysis at Karlsruhe, Germany, 1975.

6. N. Matsunami, Y. Yokoyama and N. Itoh,
"Validity of the Continuum Approximation in the Calculation of the Flux Distribution in a Channel,"
Atomic Collisions in Solids at Amsterdam, 1975.

II Domestic

1. N. Matsunami, K. Morita, S. Miyagawa and N. Itoh,
"Dechanneling Caused by Defects,"
The Annual Meeting of the Physical Society of Japan at Sapporo, 1971,
Session: Radiation Physics, 3a G7.

2. N. Matsunami, Y. Yokoyama and N. Itoh,
"Dechanneling Caused by Defects II,"
The Annual Meeting of the Physical Society of Japan at Hiroshima, 1972,
Session: Lattice Defects, 11p U7.

3. N. Matsunami and N. Itoh,
"Dechanneling Induced by Lattice Disorder,"
The Meeting of the Japan Society of Applied Physics at Nagoya, 1973,
Session: Semiconductor, 19a H7

4. N. Matsunami and N. Itoh,
"Effects of Lattice Defects on the Channeled-Particle Distribution,"
The Vernal Meeting of the Physical Society of Japan at Hiyoshi, 1973,
Session: X-Rays and Particle Beams, 23p N10.

5. N. Matsunami, S. Shibao, T. Ukai, N. Itoh and K. Morita,
"X-Ray production by Heavy Ion Bombardment,"
The Annual Meeting of the Physical Society of Japan at Tsudanuma, 1974,
Session: Radiation Physics, 14a D5.

6. N. Matsunami, T. Ukai, K. Morita and N. Itoh,
"X-ray Production in Insulators by Heavy Ion Bombardment,"
The Annual Meeting of the Physical Society of Japan at Kyoto, 1975,
Session: Radiation Physics, 5a K6.

7. N. Matsunami, Y. Yokoyama and N. Itoh,
"Determination of the Structure of the Complex of Impurities and Radiation-Induced Interstitial Halogens in Alkali Halides,"
The Vernal Meeting of the Physical Society of Japan at Kouriyama, 1975,
Session: Lattice Defects, 10a N8.